CONTROL OF DISTRIBUTED POWER IN MICROGRIDS: PV FIELD TO THE GRID, ISLANDING OPERATION, AND ULTRA-FAST CHARGING STATION.

Seyedamin Valedsaravi

UNIVERSITAT ROVIRA i VIRGILI

Control of Distributed Power in Microgrids: PV Field to the Grid, Islanding Operation, and Ultra-fast Charging Station

Author:

Seyedamin Valedsaravi

DOCTORAL THESIS

2023

UNIVERSITAT ROVIRA I VIRGILI
CONTROL OF DISTRIBUTED POWER IN MICROGRIDS: PV FIELD TO THE GRID, ISLANDING OPERATION, AND ULTRA-FAST CHARGING STATION.
Seyedamin Valedsaravi

Seyedamin Valedsaravi

CONTROL OF DISTRIBUTED POWER IN MICROGRIDS: PV FIELD TO THE GRID, ISLANDING OPERATION, AND ULTRA-FAST CHARGING STATION

DOCTORAL THESIS

Supervised by Prof. Abdelali El Aroudi and Prof. Luis Martínez-Salamero

Departament

d'Enginyeria Electrònica Elèctrica i Automàtica

UNIVERSITAT ROVIRA i VIRGILI

Tarragona

2023

UNIVERSITAT ROVIRA I VIRGILI
CONTROL OF DISTRIBUTED POWER IN MICROGRIDS: PV FIELD TO THE GRID, ISLANDING OPERATION, AND ULTRA-FAST CHARGING STATION.
Seyedamin Valedsaravi

UNIVERSITAT ROVIRA i VIRGILI
Departament d'EngInyerIa Electrònlca i Automitlca
Avinguda dels Paisos Catalans, 26. 43007 Tarngona
Tel. +34 977 55 96 10
Fax. +34 977 55 96 05

WE STATE that the present study, entitled "**Control of distributed power in microgrids: PV field to the grid, islanding operation, and ultra-fast charging station**", presented by Seyedamin Valedsaravi for the award of the degree of Doctor, has been carried out under our supervision at the Department of Electrical Electronics and Automatic Control Engineering of this university.

Tarragona, 30th August 2023

Doctoral Thesis Supervisor

Prof. Abdelali El Aroudi

Doctoral Thesis Supervisor

Prof. Luis Martinez-Salamero

UNIVERSITAT ROVIRA I VIRGILI
CONTROL OF DISTRIBUTED POWER IN MICROGRIDS: PV FIELD TO THE GRID, ISLANDING OPERATION, AND ULTRA-FAST CHARGING STATION.
Seyedamin Valedsaravi

This work has been sponsored by la Diputación de Tarragona under grant Martí i Franquès 2019PMF-PIPF-93 and by the Spanish *Ministerio de Ciencia e Innovación* under grants PID2020-120151RB-I00 and PID2019-111443RB-100.

UNIVERSITAT ROVIRA i VIRGILI

UNIVERSITAT ROVIRA I VIRGILI

Abstract

Departament D'enginyeria electrònica Elèctrica i Automàtica

Doctor of Philosophy

Control of Distributed Power in Microgrids: PV Field to the Grid, Islanding Operation, and Ultra-fast Charging Station

by Seyedamin Valedsaravi

This thesis explores the control of distributed power in microgrids (MGs) and addresses various challenges related to control, stability, power sharing, power converter design, grid connection, ultra-fast charging, and renewable energy supply. The performance of MGs is analysed in both grid-connected and islanded modes of operation, considering different configurations and power flow scenarios. The thesis focuses on several key challenges, including maximising power extraction from photovoltaic (PV) arrays in MGs utilizing DC-DC converters, injecting surplus MG power into the main grid via DC-AC voltage source inverters (VSIs) under nonlinear and unbalanced loads, optimising MG performance and power sharing in islanded mode through VSIs, connecting to the main grid at the point of common coupling (PCC) using low-frequency transformers (LFTs) and solid-state transformers (SSTs), and exploring power converter topologies for ultra-fast

DC charging of electric vehicles (EVs). The use of SSTs instead of LFTs can enhance MG capability while reducing the volume and weight of the MG electrical architecture. This thesis provides insights and solutions to address the aforementioned challenges, contributing to the advancement of MG control, stability, power quality, and efficient integration of renewable energy sources and EV charging.

Acknowledgements

First of all, I would like to thank my thesis supervisors, Prof. Abdelali El Aroudi and Prof. Luis Martínez-Salamero, for their supports on development of this thesis within the Industrial Automation and Electronics Research Group (GAEI) of the Universitat Rovira i Virgili (URV). I deeply thank them for the hours they have dedicated to me and all the supports they have given to me during this period.

I would like to express my sincere appreciation to the Martí i Franquès Fellowship at URV for their generous financial support, which has been instrumental in the completion of this research.

Finally, my heartfelt appreciation goes to my family for their unwavering love, affection, and moral support throughout this journey.

Contents

List of Figures

List of Tables

Nomenclature

AFE	Active Front End
APF	Active Power Filter
BMS	Battery Management System
CC	Constant-Current
CCCV	Constant-Current Constant-Voltage
CHB	Cascaded H-Bridge
CUF	Current Unbalance Factor
DAB	Dual Active Bridge
DAB-ANPC	Dual Active Bridge-based Active Neutral Point Clamped
DG	Distributed Generation
DHB	Dual Half Bridge
DPC	Direct Power Control
DPS	Dual-Phase-Shift
EMI	Electromagnetic Interference
EPS	Extended-Phase-Shift
EV	Electrical Vehicle
FB	Full Bridge
FC	Flying Capacitor
FFT	Fast Fourier Transform

FFV	Fossil Fuel Vehicles
FLC	Fuzzy Logic Controller
FREEDM	Future Renewable Electric Energy and Management
GA	Genetic Algorithm
GaN	Gallium Nitride
GOA	Grasshopper Optimization Algorithm
HB	Half Bridge
HFT	High Frequency Transformer
HT	Hybrid Transformer
HVDC	High-Voltage DC
IEMS	Intelligent Energy Management System
ISOP	Input Series Output Parallel
IPOS	Input Parallel Output Series
IPOP	Input Parallel Output Parallel
IPT	Inductive Power Transfer
ISOS	Input Series Output Series
LFT	Low Frequency Transformer
Li-ion	Lithium-ion
LLC-SRC	LLC Series Resonant Converter
LVDC	Low-Voltage DC
MCB	Multi-Cell Boost
MG	Microgrid
MMC	Modular Multilevel Converter
MPC	Model Predictive Controller
MPP	Maximum Power Point

MPPT	Maximum Power Point Tracking
MV	Medium Voltage
NaNiCl	Sodium Nickel Chloride
NiCd	Nickel-Cadmium
NiMH	Nickel-Metal-Hybrid
NPC	Neutral Point Clamped
OBC	On-board Charger
P2D	Pseudo-two-Dimensional
PCC	Point of Common Coupling
PFC	Power Factor Correction
PI	Proportional Integral
PID	Proportional Integral Derivative
PLL	Phase Lock Loop
PR	Proportional Resonant
PSFB	Phase-Shifted Full-Bridge
PSO	Particle Swarm Optimization
PV	Photovoltaic
PWM	Pulse Width Modulated
QAB	Quad Active Bridge
SiC	Silicon Carbide
SMC	Sliding Mode Controller
SOC	State of Charge
SOH	State of Health
SPM	Single Particle Model
SPSP	Single-Phase Single-Port

SPMP	Single-Phase Multi-Port
SPS	Single-Phase-Shift
SPWM	Sinusoidal Pulse Width Modulated
SST	Solid-State Transformer
SVPWM	Space Vector Pulse Width Modulated
THD	Total Harmonic Distortion
TLB	Three-Level Boost
TLT	Three-Level T-type
TPSP-SPC	Three-Phase Single-Port with Single-Phase Converters
TPMP-SPC	Three-Phase Multi-Port with Single-Phase Converters
TPSP-TPC	Three-Phase Single-Port with Three-Phase Converter
TPMP-TPC	Three-Phase Multi-Port with Three-Phase Converter
TPS	Triple-Phase-Shift
V2G	Vehicle-to-Grid
V2H	Vehicle-to-Home
V2V	Vehicle-to-Vehicle
VBC	Voltage Balancing Control
VF	Virtual Flux
VOC	Voltage Oriented Control
VR	Vienna Rectifier
VSI	Voltage Source Inverter
ZVS	Zero Voltage Switching
ZCS	Zero Current Switching

Chapter 1

Introduction

1.1 Background

The conventional power systems face significant challenges such as fossil fuel depletion, low energy efficiency, and environmental pollution. To address these issues, the global energy landscape is undergoing a significant transformation, driven by the increasing penetration of renewable energy sources and the need for sustainable and resilient power systems. Microgrids (MGs) have emerged as a promising solution to address the challenges posed by this evolving energy scenario [1]. A MG is a localized and self-contained power system that can operate independently or be interconnected with the main grid. It consists of distributed generations (DGs), such as solar photovoltaic (PV) arrays, wind turbines, energy storage systems, and other renewable sources, along with controllable loads and power converters [2]. MGs operate in two modes: grid-connected and islanded. Moreover, the electrical architecture of a MG can indeed be classified as AC/DC/Hybrid based on the presence of multiple types of common buses within the system. The coexistence of AC and DC common buses allows for a more versatile and flexible energy distribution

and management in the MG [3]. An AC common bus in the MG serves as the primary distribution point for AC loads and sources. AC loads, such as residential and commercial buildings, can be connected to this common bus, and AC generation sources, like conventional power plants or wind turbines with AC outputs, can also feed power into the AC common bus. This AC distribution network is a common feature of traditional power systems. A DC common bus in the MG functions as a separate distribution point for DC loads and sources. DC loads, such as batteries, electric vehicle (EV) chargers, and some electronic devices, can be connected to this common bus. Additionally, DC power sources, like PV panels and energy storage systems, can inject power into the DC common bus. The DC distribution within the MG offers advantages like reduced conversion losses and improved power quality for specific applications. In a hybrid MG, an AC/DC common bus exists, allowing for bi-directional power flow between the AC and DC sides of the MG. Power converters and solid-state transformers enable seamless integration and interaction between AC and DC systems [4]. This setup allows surplus power generated by renewable sources on the DC side (e.g., solar panels) to be transferred to the AC side for consumption or vice versa. The bidirectional power flow enhances energy flexibility and management within the MG [5]. As a result, the AC/DC/Hybrid architecture offers several benefits, including efficient power flow management, the ability to integrate diverse energy sources (renewable energies, conventional), and the potential for advanced energy storage and demand response strategies [6]. By combining AC and DC technologies in a MG, energy conversion losses can be minimized, and the system can be better optimized for specific loads and sources.

Controlling distributed power in MGs is crucial due to the integration of many energy sources and the uncertainty in load and supply factors. Efficient control directly influences the stability, power quality, and effective utilization of renewable energy resources within

the MG. As an example, in the islanded mode, power balance between production and consumption, equivalent to load and frequency control, becomes a major challenge. Thus, the effective management of power generation, distribution, and consumption is essential to realize the full potential of MGs and promote their widespread adoption [7].

The PV systems are one of the most widely deployed renewable energy sources in MGs. PV arrays convert sunlight into electricity, but their output is highly dependent on environmental factors and can fluctuate rapidly. Therefore, developing robust control strategies for PV systems is essential to optimize power extraction from the PV arrays while maintaining grid compatibility. Challenges arise due to the presence of nonlinear and unbalanced loads, which can impact MG stability and introduce harmonics and reactive power issues [8].

The MGs must be capable of operating in islanded mode, where they can function autonomously without a connection to the main grid. During grid disturbances or emergencies, islanded operation allows MGs to maintain power supply to critical loads and continue supporting the local community. However, achieving stable and efficient islanded operation requires careful consideration of control parameters and power-sharing strategies among DGs. Ensuring MG stability and reliability across various operating conditions is a crucial objective in islanded mode of operation [9].

With the proliferation of EVs, the demand for ultra-fast charging stations in MGs has increased. Ultra-fast charging aims to significantly reduce charging times for EVs, improving user convenience and promoting wider EV adoption. The integration of such high-power charging stations poses challenges related to power conversion efficiency and power imbalance issues. Solid-state transformers (SSTs) have shown potential in addressing these challenges by providing increased control capability and reducing the size and

weight of the MG electrical architecture [10].

1.2 Literature Review

In MGs, the utilized renewable energy sources such as PV and wind are intermittent in nature, necessitating the use of power electronics converters to regulate voltage, current, and power [9]. These converters can introduce harmonic pollution into the power system, leading to various power quality problems such as voltage waveform distortion, overheating of components, and interference with communication systems [11]. Some sources of harmonic pollution are nonlinear loads like diode-rectifiers, arc furnaces, electrified railways, and frequency control devices. Active power filters (APFs) and passive power filters have been used in industrial applications to compensate for harmonic current and suppress harmonic voltage in both shunt and series modes of operation [12].

A grid-connected voltage source inverter (VSI) with a PV-fed system has inherently shunt APF capability. The control of this PV-fed system is essential for delivering maximum power to the main grid, ensuring high power quality in grid currents, complying with IEEE standards, and compensating for nonlinear local load harmonics, reactive power, and unbalanced sequences. Previous control strategies for shunt APF compensation, such as the instantaneous $p-q$ power theory and the abc power theory, have limitations under certain conditions [13]. The proposed control strategy in this thesis aims to overcome these barriers and provide effective shunt APF compensation in both three-phase three-wire and three-phase four-wire systems. It employs a proportional-resonant (PR) controller with harmonic compensators implemented in the abc reference frame. Moreover, the PR controller design is challenging due to the inherent resonance characteristic of the LCL output

filter in the grid-connected VSI. Additionally, incorporating harmonic compensators complicates the control design. Literature methods for coefficients selection of PR controllers do not fully consider the system's performance in terms of steady-state and stability criteria, leading to potential instability issues.

Imbalances between DGs and loads in islanded MGs lead to frequency fluctuations, impacting power quality and system stability. Furthermore, uncertainties arising from unpredictable environmental changes with high renewable energy penetration further complicate MG operation [14]. Therefore, a robust control technique is needed to ensure small-signal stability in MGs under varying load or source conditions. In the islanded mode of MG operation, droop control strategies have been widely used due to their advantages such as simplicity, no need for communication lines among DGs, and plug-and-play functionality. However, the stability and power quality of MGs are affected by droop control coefficients and controllers' parameters [15]. Various methods for selecting controller coefficients have been proposed in the literature, including trial and error, designing the controllers' parameters to ensure the outer loop's slower dynamics compared to the inner loop, and using optimization algorithms like genetic algorithm (GA) and particle swarm optimization (PSO). However, each approach has its limitations in providing a universal and simple design approach for tuning the controllers' parameters to guarantee small-signal stability across the entire range of MG operations [16].

The transition from fossil fuel vehicles to EVs is driven by the need to reduce carbon dioxide emissions, which have a direct impact on climate change and global warming. The increasing popularity of EVs as an eco-friendly alternative to fossil fuel vehicles has led to the need for efficient and fast-charging solutions [17]. However, the onboard chargers connected to single-phase or three-phase AC domestic supply, which are commonly used,

cannot fulfill the technical requirements of battery fast charging [18]. To achieve rapid charging, a significant amount of DC power is required, necessitating the supply of the charging station MG from a medium voltage (MV) AC source. This connection can be accomplished through a low frequency transformer (LFT), a hybrid transformer (HT), or a SST. The motivation of the thesis is to present the state of the art of ultra-fast charging stations, particularly focusing on DC SST-based stations, which allow the integration of renewable energies, energy storage, and AC/DC loads, forming an AC/DC/Hybrid MG [19]. In contrast, LFT-based charging stations lack renewable energy integration but offer high reliability. Among the options, SSTs offer advantages such as higher control freedom, energy storage integration, smaller size, fault current limitation, and bidirectional power flow capability [20]. With advancements in high-voltage high-power silicon carbide (SiC) and gallium nitride (GaN) devices, SSTs have become promising for high-power applications [21].

1.3 Objectives of the Thesis

Overall, the thesis aims to provide comprehensive strategies for enhancing the efficiency, stability, reliability, and resilience of modern power systems through the integration and control of distributed power in MGs. Different flow of power in a MG have been investigated which is shown in Fig 1.1. Through the analysis has been done, we aim to accomplish the following objectives:

- To investigate the challenges associated with the control of distributed power in MGs and its impact on system stability, power quality, and the efficient utilisation of renewable energy resources.

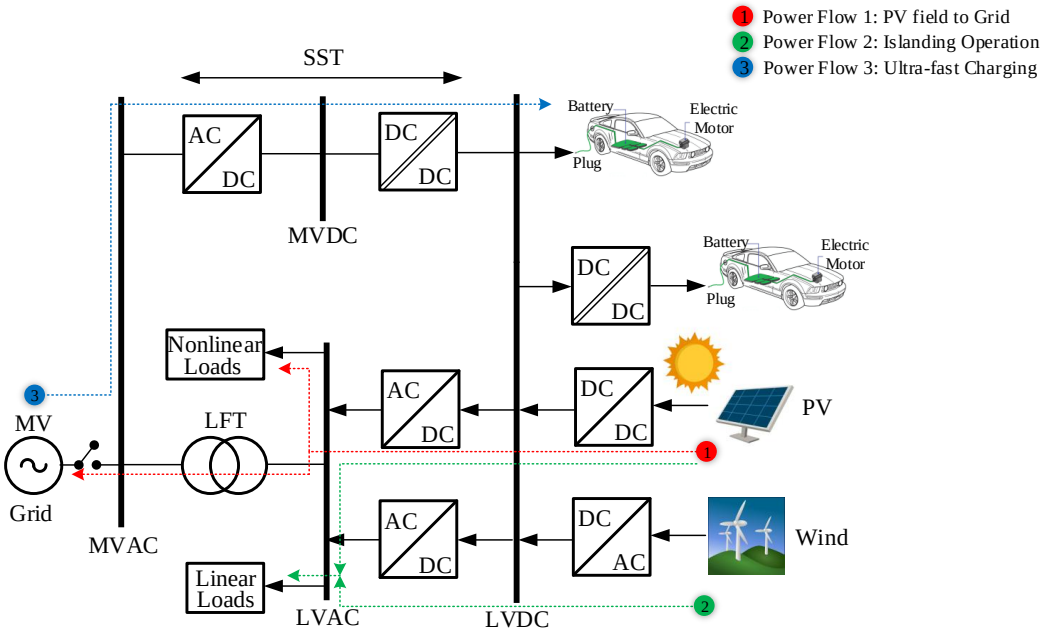

Figure 1.1: The different scenarios of power distribution in a hybrid MG.

- To develop a comprehensive control strategy for a PV-fed multifunctional grid-connected inverter to optimise power extraction from PV arrays, maintain grid compatibility, and compensate for harmonics and reactive power.
- To design and optimise controller parameters for MGs operating in islanded mode to ensure system stability and desirable power sharing among distributed generation units.
- To explore the potential benefits of SSTs in ultra-fast charging stations within MGs, including increased control capability, reduced size, and weight of the MG electrical architecture.

- To review existing SST features and propose a classification of SST-based architectures for charging stations in MGs.
- To address diverse challenges in MGs, including control, stability, power sharing, power converter design, grid connection, and renewable energy integration.
- To contribute to the advancement of MG technologies and facilitate the transition towards sustainable and resilient energy systems.

By achieving these research objectives, the thesis aims to contribute to the advancement of MG technologies, ensuring their effective integration into the modern power system and supporting the transition to a sustainable and resilient energy future.

1.4 Thesis Structure

This thesis is divided into three sub-studies. In the first sub-study, the focus is on the control of a PV-fed multifunctional grid-connected inverter. This study addresses the challenges posed by nonlinear and unbalanced loads, aiming to optimise power extraction from PV arrays while maintaining grid compatibility and compensating for harmonics and reactive power. The proposed control strategy, based on a quasi-PR controller with harmonic compensators, demonstrates superior performance in tracking sinusoidal references and effectively compensating for the impact of nonlinear loads. The methodology, results, and conclusion pertaining to this sub-study can be found in Chapters 2.

The second sub-study attention is directed towards the control of MGs in islanded mode, where the MG operates autonomously without a connection to the main grid. In

this context, the selection and optimisation of controller parameters play a crucial role in maintaining system stability and ensuring desirable power sharing among distributed generation units. The study formulates an optimisation problem based on a state-space model of a VSI and employs PSO, GA, and a hybrid PSO-GA approach to determine optimised controller parameters. This approach offers a simple yet effective design methodology that guarantees stability and enhances performance across various operating conditions, regardless of the number of inverters, system configuration, output impedance differences, and load types. The result is presented in Chapter 3.

In chapter 4, the electrical architecture of ultra-fast charging stations in MGs, considering the replacement of low-frequency service transformers with SSTs. The adoption of SSTs in ultra-fast charging offers advantages such as increased control capability, reduced size, and weight of the MG electrical architecture. The chapter presents a review of existing SST features and proposes a classification of SST-based architectures for charging stations. The findings highlight the potential of SSTs in improving power conversion efficiency and addressing power imbalance issues in ultra-fast charging applications, ultimately contributing to the development of efficient and compact MG electrical architectures.

Chapter 5 serves as the concluding chapter, highlighting the key contributions and main conclusions of the dissertation. It emphasises the significance of these findings. Additionally, the chapter outlines potential avenues for future research and further developments in the field. These proposed research directions aim to enhance the distribution of power in MGs, to improve MG stability and efficiency, and to contribute to the advancement of ultra-fast charging techniques in the future power system grid.

1.5 Publications and Conferences List

Some of the results presented in this thesis are published.

1. **S.Valedsaravi**, A. El Aroudi, J. A. Barrado-Rodrigo, W. Issa, L. Martínez-Salamero. "Control Design and Parameter Tuning for Islanded Microgrids by Combining Different Optimization Algorithms." *Energies* (2022), 15(10).

2. **S.Valedsaravi**, A. El Aroudi, L. Martínez-Salamero. "Review of Solid-State Transformer Applications on Electric Vehicle DC Ultra-Fast Charging Station." *Energies* (2022), 15(15).

3. **S.Valedsaravi**, A. El Aroudi, J. A. Barrado-Rodrigo, M. Hamzeh, L. Martínez-Salamero. "Multi-resonant Controller Design for a PV-Fed Multifunctional Grid-Connected Inverter in Presence of Unbalanced and Nonlinear Load." *Journal of Control, Automation and Electrical Systems* (2023), 34(4).

4. **S.Valedsaravi**, A. El Aroudi, L. Martínez-Salamero. "Control of a PV-fed Cascaded Half-Bridge Multilevel Inverter with Shunt Active Power Filter Capabilities." *IFAC-PapersOnLine* (2022), 55(12).

The results presented in conference proceedings.

1. **S.Valedsaravi**, A. El Aroudi, J. A. Barrado-Rodrigo, M. Hamzeh, A. Cid-Pastor, L. Martínez-Salamero. "Grid-connected LCL Filter Design with Different Damping Methods." *Seminar on Automation, Industrial Electronics and Instrumentation (SAAEI'21)* (2021), University of Castilla-La Mancha, Ciudad Real.

2. **S.Valedsaravi**, A. El Aroudi, L. Martínez-Salamero. "Nine-level PV-fed Cascaded H-Bridge Inverter Operating As a Shunt Active Power Filter." *Seminar on Automation, Industrial Electronics and Instrumentation (SAAEI'22)* (2022), Universitat de Lleida, Lleida.

3. **S.Valedsaravi**, A. El Aroudi, L. Martínez-Salamero. "Control of a PV-fed Cascaded Half-Bridge Multilevel Inverter with Shunt Active Power Filter Capabilities." *14th IFAC Workshop on Adaptive and Learning Control Systems ALCOS 2022* (2022), Casablanca, Morocco.

Chapter 2

PV Field to the Grid

2.1 Abstract

The use of APFs in future power grids with high penetration of nonlinear loads is unavoidable. The VSIs interfacing PV generator could play the APF role in addition to power supply. In this chapter, the control of a PV-fed multifunctional grid-connected three-phase VSI is addressed with nonlinear and unbalanced load. The control objective is threefold. The first one is to deliver the maximum available power from the PV source to the grid satisfying power quality standards. The second one is the Voltage Balancing Control (VBC) for DC-link capacitors to guarantee correct operation of the VSI. The last one is shunt APF control to compensate for nonlinear and unbalanced load harmonics, reactive power, and unbalanced sequences. A quasi-PR controller with harmonic compensators is proposed for the current control loop. The quasi-PR controller parameters are determined through optimization algorithms such as PSO, GA, and a combination of both PSO and GA. The aim of the objective function is to improve static and dynamic behavior. The different gains at the fundamental resonant frequency and the selected odd harmonics are obtained for

the proposed quasi-PR controller. The dynamic characteristics of the optimized quasi-PR controllers show superiority against conventional ones in terms of gain margin, phase margin, overshoot, and robustness. With the proposed control scheme, the harmonics, reactive power, and unbalanced sequences are appropriately compensated. The performance of the PV-fed VSI shunt APF under irradiance change, load change, and distorted grid voltage conditions is validated through numerical simulations performed on PSIM© software. The results show that the grid currents Total Harmonic Distortion (THD) for irradiance change case study are 4.57%, 4.57%, and 3.22% in phase a, b, and c with the proposed control method while they are 9.25%, 5.65%, and 10.12% with conventional instantaneous $p-q$ theory.

2.2 Introduction

Conventional power systems are experiencing serious challenges such as fossil fuel depletion, low energy efficiency, and environmental pollution. These problems are the main driving factors toward using renewable energy resources [9]. These sources of energy are intermittent in nature; hence, interfacing power electronics converters are necessary to regulate voltage, current, and power. These converters are the sources of harmonic pollution in the power system. Nonlinear loads, such as diode-rectifiers, arc furnaces, electrified railways, and frequency control devices could be considered as other sources of harmonic pollution which may jeopardize the power system's safe and stable operation and may create serious power quality problems for both customers and suppliers. The harmonic power losses can lead to a rise in operational costs and create additional heating issues in power system components [11]. This can give rise to a reduction in their life span. As an example, the harmonic losses in facility transformers at the point of common coupling

(PCC) can lead to an increase in the aging costs [12], [22]. Other problems are overheating of capacitors, voltage waveform distortion, voltage flicker, and interference with the communication system. Moreover, the IEEE standard limit is 5% total harmonic distortion (THD) at PCC [23]. To cope with the power quality problems, active power filters (APF) and passive power filters [24] have been extensively used in industrial applications. They can be utilized for harmonic current compensation and harmonic voltage suppression in both shunt and series modes of operation.

In a grid-connected VSI with photovoltaic-fed (PV-fed) system, the connection to the three-phase power grid is realized through a DC-link and an inverter. This inverter could work with multifunctional capability, including APF and power supply [25]. As a consequence, the control of a grid-connected PV-fed VSI can realize different aims such as delivering maximum power to the main grid, guaranteeing grid current high power quality, satisfying IEEE standards, and compensating for the nonlinear local load harmonics, reactive power, and unbalanced sequences.

The most popular control strategies for shunt APF compensation are the instantaneous $p-q$ power theory, based on abc to $\alpha\beta 0$ Clarke transformation, and the abc power theory [13]. The performance from the $p-q$ theory is poor under three-phase unbalanced load current and distorted grid voltage. The algorithm may produce some harmonics in the grid current, namely hidden currents, which are not present in the local load currents [26]. In addition, the algorithm suffers from extra calculation effort in case of multiple harmonic eliminations. In the abc power theory, the active and nonactive components of the currents are obtained through a minimization technique such as the Lagrange Multiplier method and the generalized Fryze currents [27]. In the first method, the constraint of the minimization problem is the three-phase instantaneous active power. This method

results in poor performance for inconstant three-phase active power and in presence of zero-sequence components. Therefore, the compensation technique will draw undesirable zero-sequence current from the network [28]. In the second minimization method, the average value of three-phase instantaneous active power is used to obtain the active components of the currents. As a result, the algorithm is not an instantaneous theory and could have some malfunctions during transient periods [29]. To deal with these barriers, a control strategy is proposed in this chapter for the shunt APF compensation. The proposed control strategy could have desirable performance in both three-phase three-wire and three-phase four-wire systems. Table 2.1 shows a comparative analysis of the different shunt APF compensation methods.

Table 2.1: A comparative analysis of different shunt APF compensation methods.

Shunt APF theories	Unbalanced/Distorted voltage	Zero-sequence	Transient	Calculation effort
Instantaneous $p-q$	Poor	Poor	Good	Acceptable
Lagrange Multiplier	Acceptable	Very poor	Poor	Poor
Generalized Fryze currents	Good	Very poor	Very poor	Poor
The proposed method	Very Good	Good	Good	Acceptable

The proposed shunt APF control strategy is implemented in the *abc* reference frame. Therefore, the current control loop reference signal is a sinusoidal waveform with harmonic contents. The PR controller with harmonic compensators is the most usable one in the current control loop. The PR controller design of a grid-connected VSI with an LCL output filter is a challenging task due to the LCL inherent resonance characteristic [30]. The control design is more challenging when harmonic compensators are added. The PR controller with harmonic compensators is usually limited to several low-order current harmonics since high-order harmonics can be out of control system bandwidth which can lead to instability problems. The stability analysis of PR-controlled grid-connected inverters with LCL filter is carried out in [30] which shows direct dependence on the controller

parameters [31]. To tune controller gains, the values of harmonic resonant coefficients are selected equally to the fundamental harmonic coefficient in [32] and in [33] and are selected inversely proportional to the value of the fundamental harmonic coefficient in [31]. However, these ways of coefficient selection are not optimum way as they don't consider the performance of the controller in terms of steady-state and stability criteria. Moreover, the selection of the same coefficients for the higher-order compensators may lead to system instability. Therefore, in this chapter, the multi-resonant PR controller coefficients are determined through optimization algorithms which considerably reduces controller design complexity. Moreover, the system's static and dynamic behavior are improved.

2.3 System description

Fig. 2.1 shows the scheme of the studied system in this chapter. It consists of a PV source, a three-level boost (TLB) converter, and a three-phase four-wire grid-connected VSI with an LCL filter. It is worth mentioning that a three-phase network with more than one point grounded can also be classified as a three-phase four-wire system. In this system, the TLB converter performs maximum power point tracking (MPPT) control and DC-link voltage balancing control (VBC). The TLB is used to deliver maximum available power from the PV source to the main grid. A three-phase inverter is interfacing with the main grid and local load through an LCL filter to decrease switching harmonics injection. The nonlinear and unbalanced load involving full-wave bridge rectifiers, series resistor and inductor is located in parallel at PCC. The whole system is connected to the main grid through the PCC. Different components of load current such as harmonics, reactive power, and unbalanced sequences are separated through mathematical equations [34]. Using these components, the reference of grid-side inverter current i_2^* is obtained and then used in

the current control loop. The three-phase grid voltages v_{ga}, v_{gb}, and v_{gc} are considered sinusoidal as follows

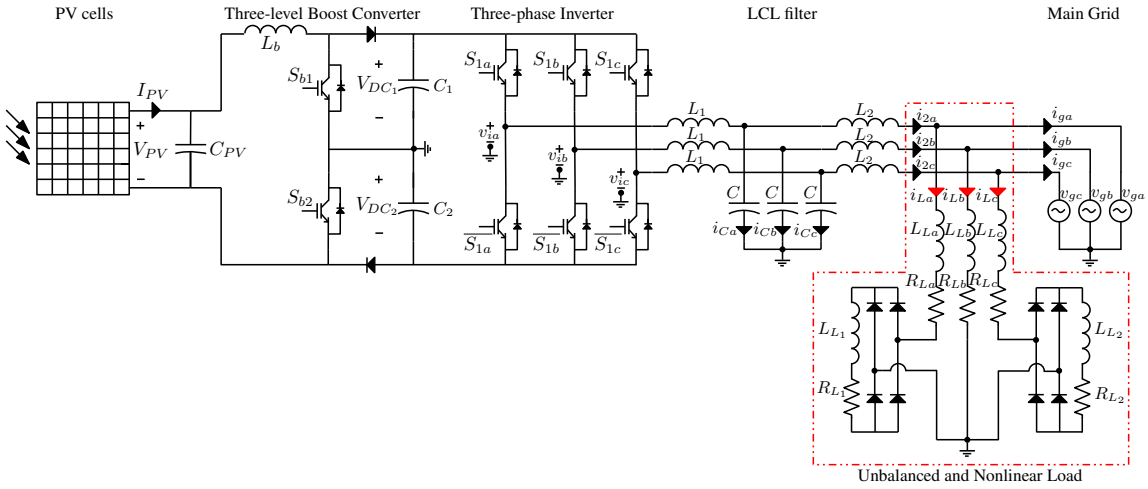

Figure 2.1: The schematic circuit diagram of the studied PV-fed system interfacing TLB converter and grid-connected three-phase inverter with shunt APF capability.

$$
\begin{aligned}
v_{ga} &= V_{ga}\sqrt{2}\sin(\omega_g t) \\
v_{gb} &= V_{gb}\sqrt{2}\sin(\omega_g t - \frac{2\pi}{3}) \\
v_{gc} &= V_{gc}\sqrt{2}\sin(\omega_g t + \frac{2\pi}{3})
\end{aligned}
\tag{2.1}
$$

where V_{ga}, V_{gb}, and V_{gc} are the RMS values of grid voltages and ω_g is the grid angular frequency. Table 2.2 shows the system parameters.

The DC-link consists of two identical capacitors each with a voltage $V_{\mathrm{DC}}/2$ grounded at the midpoint. The LCL filter is used to limit current harmonic pollution at the PCC which should be below 5% according to the [23] standard. The resistive and inductive value of the main grid at the PCC can be neglected [35]. Furthermore, the filter resistances

Table 2.2: The circuit parameters.

Parameters	Symbol	Value
Grid nominal frequency	f_g	50 Hz
PV maximum power	P_{max}	10 kW
DC-link voltage	V_{DC}	1000 V
Inverter switching frequency	f_{sw}	16 kHz
TLB switching frequency	f_{tlb}	10 kHz
RMS values of grid voltages	V_{ga}, V_{gb}, V_{gc}	230 V
Inverter-side inductance	L_1	1.8 mH
Grid-side inductance	L_2	0.9 mH
Filter capacitance	C	11 µF
DC-link capacitance	C_1, C_2	1 mF
TLB inductance	L_b	0.1 mH
PV output capacitance	C_{PV}	1 mF
AD loop gain	K_{AD}	32 Ω

representing parasitic losses slightly change the dynamics of the ideal LCL filter and can also be neglected.

2.4 System control

The whole control diagram of the PV-fed VSI shunt APF is shown in Fig. 2.2. The grid-side inverter current reference i_2^* generation is an important task of the control system. The proposed control method is based on extracting harmonics, negative, and zero sequences of the local load current. First, the harmonic content of the three-phase load current is separated from its fundamental value by subtraction from the measured load current. The load current fundamental components enter the inverse Fortescue transformation to realize the unbalanced sequences of the local load current. The negative and zero sequence of grid-side inverter current references $i_{2_{ref}}^-$ and $i_{2_{ref}}^0$ are set to the load current negative

and zero sequences. Thereafter, the positive sequence of grid-side inverter current $i^{+}_{2_{ref}}$ is obtained according to the PV power, local load reactive power, RMS value of the grid voltage, and grid synchronization term. Then, Fortescue transformation is used to determine compensated currents $i_{2a_{com}}$, $i_{2b_{com}}$, and $i_{2c_{com}}$ for each phase. The load current harmonic contents i_{La_H}, i_{Lb_H}, and i_{Lc_H} are all added to the compensated currents to obtain the grid-side inverter current references i^{*}_{2a}, i^{*}_{2b}, and i^{*}_{2c}. A multi-resonant controller is used for the current control loop. It has 3rd, 5th, 7th, 9th, 11th and 13th harmonic compensators to accurately track the references.

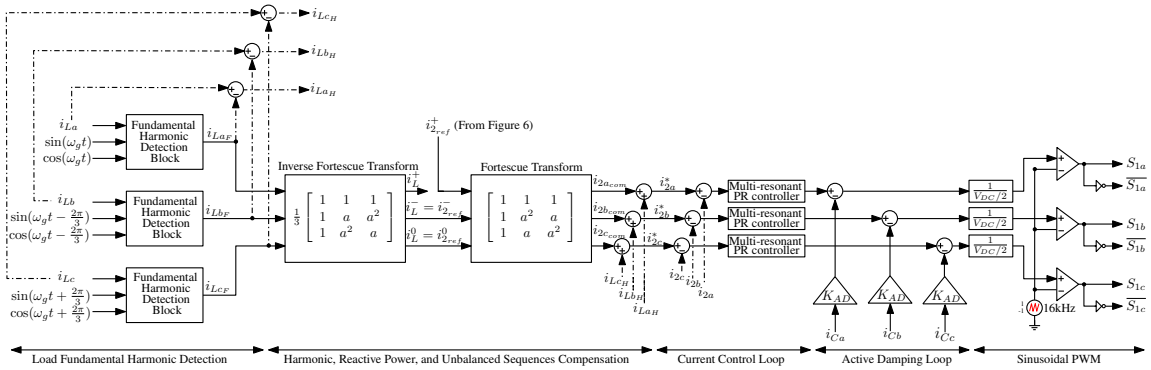

Figure 2.2: The control diagram of the PV-fed VSI shunt APF.

2.4.1 MPPT control of the PV source with TLB converter

The output power of a PV generator is dependent on solar irradiation and ambient temperature. The power-voltage curve of a PV source has a maximum power point (MPP) value. In order to make the system to operate at MPP, different techniques have been proposed such as perturbation and observation (P&O), incremental conductance, and ripple correlation [36]. In this chapter, the most popular algorithm, P&O, is used for MPPT control of the

PV source through the TLB converter. The control diagram of the TLB converter is illustrated in Fig. 2.3. The output voltage V_{PV} and output current I_{PV} of the PV generator are sensed and then applied as inputs to the MPPT block. The current value of the PV power compares with the past value and a step change is applied to the desired voltage reference V_{ref} in the control loop. Proportional integral (PI) controllers are employed to regulate the input voltage of the TLB converter to its reference value. As shown in Fig. 2.3, the VBC is another important task of the TLB converter control to guarantee stable operation of the VSI. It can be performed by a PI controller with the input of DC-link voltages subtraction. The PI controller of VBC is designed in such a way that it should be faster than the MPPT control. The switching patterns of the TLB converter are realized through the pulse-width modulation (PWM) method. The phase difference of sawtooth carrier waveforms in the TLB switches is set to 180°.

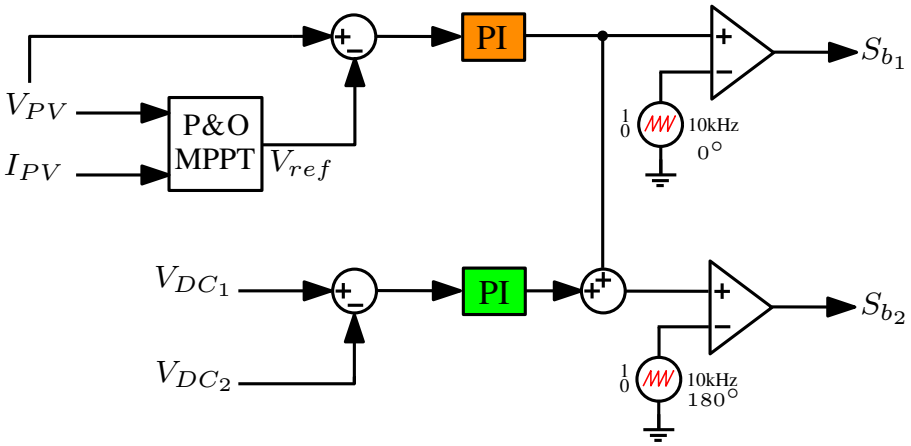

Figure 2.3: The control scheme of the TLB converter.

2.4.2 Grid synchronization

In the grid-connected application of VSI, the generated output voltage should be synchronized with the grid voltage. The injected current to the grid should have high power quality. The phase-locked loop (PLL), zero-crossing detection, artificial neural network, and adaptive linear neuron are some of the synchronization techniques proposed in the literature [37]. In this chapter, the PLL approach is used which has three basic functional blocks known as phase detector, loop filter, and voltage-controlled oscillator as shown in Fig. 2.4. The loop filter cutoff frequency ω_{cf} is selected as 30 Hz. In the proposed PLL technique, the synchronization terms of the three-phase grid voltage, $\sin(\omega_g t)$, $\sin(\omega_g t - \frac{2\pi}{3})$, and $\sin(\omega_g t + \frac{2\pi}{3})$ are obtained. Table 2.3 illustrates the selected PI controllers' parameters for the MPPT, VBC, and PLL determined through Ziegler–Nichols tuning method.

Table 2.3: The PI controllers' parameters.

PI Controller	Gain	Time constant (s)
MPPT	0.002	0.01
VBC	0.000001	0.001
PLL	50	0.005

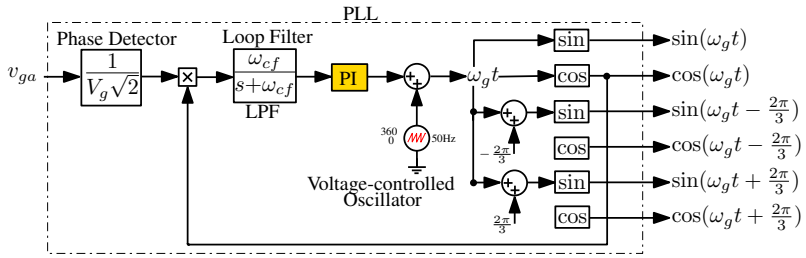

Figure 2.4: The proposed PLL control scheme.

2.4.3 Shunt APF control of VSI

In order to add the shunt APF capability to the three-phase VSI, the harmonic current and positive sequence of grid-side inverter current reference must be determined. The fundamental harmonic detection block is used for the load current harmonic detection. In addition, the PV power, the load reactive power, and the grid voltage are considered for obtaining the positive sequence of the grid-side inverter current reference.

2.4.3.1 Load current harmonic detection

In order to improve power quality in grid-connected VSIs with nonlinear loads, the detection of harmonic components is needed. These components are part of the compensation signal in the control of grid-connected VSI [38]. A wide range of harmonic detection methods has been used in both time and frequency domains [38]. The fast Fourier transform (FFT), discrete Fourier transform, and recursive discrete Fourier transform are the examples of frequency-domain algorithms. In addition, the synchronous reference frame theory, the stationary frame filters, and the notch filters are some examples of the time-domain algorithms. Here in this chapter, the FFT is used to detect load current harmonic content.

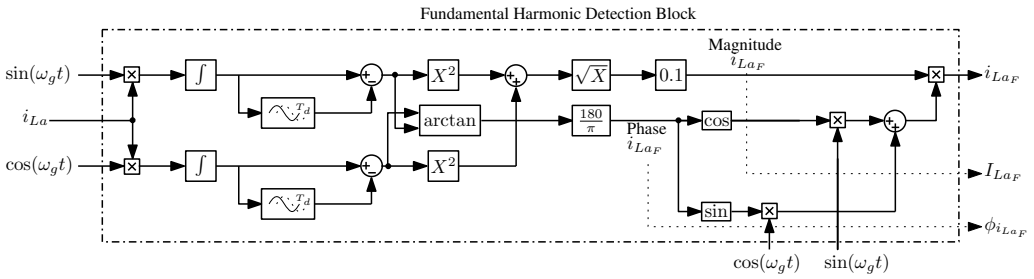

Figure 2.5: The fundamental harmonic detection block.

Figure 2.5 illustrates the block diagram of the fundamental harmonic detection block in phase *a*. The Fourier transform is utilized in each phase to extract the fundamental harmonic magnitudes and phases. Then, the fundamental harmonic signals are built in each phase. They are subtracted from the load currents to create the load current harmonic reference for the current controller. In each phase, the synchronization terms $\sin(\omega_g t)$, $\cos(\omega_g t)$, $\sin(\omega_g t - \frac{2\pi}{3})$, $\cos(\omega_g t - \frac{2\pi}{3})$, $\sin(\omega_g t + \frac{2\pi}{3})$, and $\cos(\omega_g t + \frac{2\pi}{3})$ are applied to the fundamental harmonic detection block. Therefore, the harmonic currents references in phases *a*, *b*, and *c* are extracted independently and imported to the proposed control diagram. The three-phase load current consists of fundamental components i_{La_F}, i_{Lb_F}, i_{La_F} and their harmonic terms i_{La_H}, i_{Lb_H}, i_{Lc_H} which can be expressed as follows

$$\begin{aligned} i_{La} &= i_{La_F} + i_{La_H} \\ i_{Lb} &= i_{Lb_F} + i_{Lb_H} \\ i_{Lc} &= i_{Lc_F} + i_{Lc_H} \end{aligned} \tag{2.2}$$

where i_{La}, i_{Lb}, and i_{Lc} are the three-phase load current. Therefore, the load current harmonic references are obtained as follows

$$\begin{aligned} i_{La_H} &= i_{La} - i_{La_F} \\ i_{Lb_H} &= i_{Lb} - i_{Lb_F} \\ i_{Lc_H} &= i_{Lc} - i_{Lc_F} \end{aligned} \tag{2.3}$$

2.4.3.2 Positive sequence of grid-side inverter current reference

In order to obtain the positive sequence of the grid-side inverter current reference, the fundamental components of load current are used. The positive i_L^+, negative i_L^-, and zero

sequence i_L^0 of the fundamental load current can be obtained using the inverse Fortescue transform [13]

$$\begin{aligned} i_L^0 &= \frac{1}{3}(i_{La_F} + i_{Lb_F} + i_{Lc_F}) \\ i_L^+ &= \frac{1}{3}(i_{La_F} + a i_{Lb_F} + a^2 i_{Lc_F}) \\ i_L^- &= \frac{1}{3}(i_{La_F} + a^2 i_{Lb_F} + a i_{Lc_F}) \end{aligned} \tag{2.4}$$

where $a = e^{j\frac{2\pi}{3}}$ and i_L^+ can be rewritten as follows

$$i_L^+ = I_L^+ \sin(\omega_g t + \phi_{i_L^+}) \tag{2.5}$$

where I_L^+ and $\phi_{i_L^+}$ are the magnitude and phase of the fundamental load current positive sequence respectively. The magnitude of the grid-side inverter current reference positive sequence $I_{2_{ref}}^+$ is dependent on the PV power P_{PV} which can be obtained as follows

$$I_{2_{ref}}^+ = \sqrt{2}\frac{P_{PV}}{3V_{ga}} \tag{2.6}$$

The phase of the grid-side inverter current reference positive sequence $\phi_{I_{2_{ref}}^+}$ is obtained through the PV power and the load reactive power Q_L. By neglecting the TLB power losses, the inverter active power P_i can be considered equal to P_{PV}. The load reactive power is defined as follows

$$Q_L = 3V_{ga}\frac{I_L^+}{\sqrt{2}}\sin\phi_{i_L^+} \tag{2.7}$$

Therefore, the phase of grid-side inverter current reference positive sequence can be found as follows

$$\phi_{I_{2_{ref}}^+} = \frac{180}{\pi}\arctan\frac{Q_L}{P_{PV}} \tag{2.8}$$

As a result, the positive sequence of the grid-side inverter current reference $i^+_{2_{ref}}$ is given by

$$i^+_{2_{ref}} = I^+_{2_{ref}} \sin(\omega_g t + \phi_{I^+_{2_{ref}}}) \tag{2.9}$$

The block diagram of the grid-side inverter current reference positive sequence determination is illustrated in Fig. 2.6.

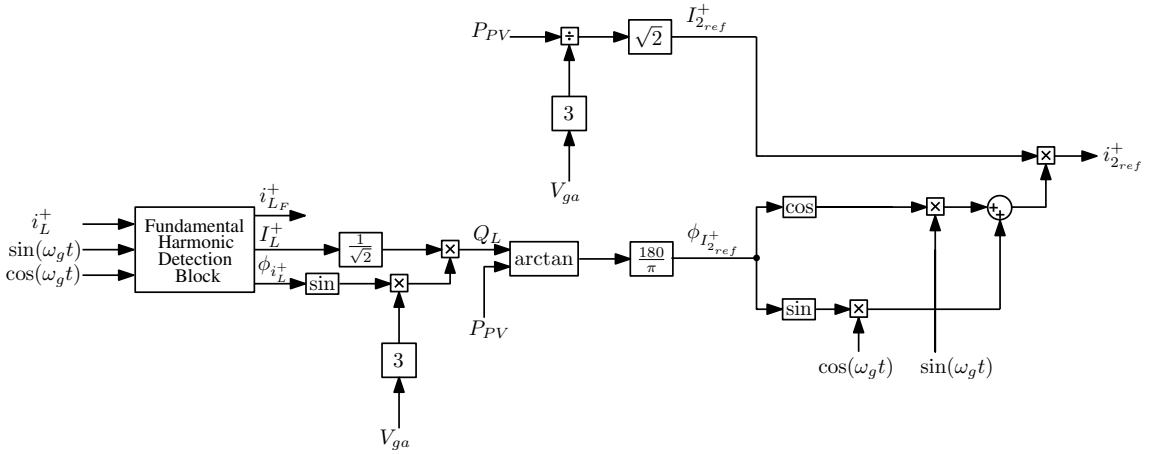

Figure 2.6: The determination of positive sequence of the grid-side inverter current reference involving reactive power compensation.

It could be equivalently expressed in the extended form as follows

$$i^+_{2_{ref}} = I^+_{2_{ref}} (\sin \omega_g t \cos \phi_{I^+_{2_{ref}}} + \cos \omega_g t \sin \phi_{I^+_{2_{ref}}}) \tag{2.10}$$

At last, the compensated currents $i_{2a_{com}}$, $i_{2b_{com}}$, and $i_{2c_{com}}$ in each phase can be found as follows

$$\begin{aligned} i_{2a_{com}} &= i^0_{2_{ref}} + i^+_{2_{ref}} + i^-_{2_{ref}} \\ i_{2b_{com}} &= i^0_{2_{ref}} + a^2 i^+_{2_{ref}} + a i^-_{2_{ref}} \\ i_{2c_{com}} &= i^0_{2_{ref}} + a i^+_{2_{ref}} + a^2 i^-_{2_{ref}} \end{aligned} \tag{2.11}$$

where $i^{-}_{2_{ref}} = i^{-}_{L}$ and $i^{0}_{2_{ref}} = i^{0}_{L}$. By the summation of the compensated current reference and harmonic current reference, the reference of the grid-side inverter currents i^{*}_{2a}, i^{*}_{2b}, and i^{*}_{2c} for shunt APF control of the VSI are given by

$$\begin{aligned} i^{*}_{2a} &= i_{2a_{com}} + i_{La_H} \\ i^{*}_{2b} &= i_{2b_{com}} + i_{Lb_H} \\ i^{*}_{2c} &= i_{2c_{com}} + i_{Lc_H} \end{aligned} \tag{2.12}$$

2.4.4 Current control loop with AD

Different types of controllers have been used for the current control of grid-connected VSIs such as PI, PR [39], predictive [40], hysteresis, and sliding mode control [41]. The PI control strategy in the dq reference frame is the widely used one [42]. It has a desirable performance in balanced systems. However, it has poor performance in unbalanced and nonlinear systems [43]. In this chapter, since all the reference signals are sinusoidal; therefore, the PR controller is utilized. This controller has less steady-state error and selective harmonics compensation capability [44].

Furthermore, the high peaking at LCL filter resonant frequency may lead to instability issues. To solve this problem, different damping techniques such as passive damping (PD) and active damping (AD) have been proposed. The PD consists of adding a resistor to one of the filter elements. The use of a resistor as a damper leads to extra losses and less efficiency. Another damping method is the AD method which consists of adding a feedback path to the control system. The advantage of this technique is the removal of power loss. However, it needs an extra sensor and adds complexity to the control system [45]. The damping technique used in this chapter is an AD based on the capacitor current

feedback loop as illustrated in Fig. 2.2.

2.4.4.1 Quasi multi-resonant controller design

The transfer function of the LCL output filter with the additional AD feedback from the inverter output voltage v_{ia}^{*} to the grid-side inverter current i_{2a}^{*} is

$$G_{sys}(s) = \frac{1}{L_1 L_2 C s^3 + L_2 C K_{AD} s^2 + (L_1 + L_2)s} \tag{2.13}$$

In the current control loop, a multi-resonant PR controller is used. The transfer function of the proposed multi-resonant PR controller with odd harmonic compensators up to 13^{th} can be expressed as follows

$$G_c(s) = K_P + \sum_{h=1}^{7} \frac{2K_{i(2h-1)}\omega_c s}{s^2 + 2\omega_c s + \omega_{2h-1}^2} \tag{2.14}$$

where K_P is the proportional gain, $K_{i(2h-1)}\ |_{h=1\ldots7}$ are the resonant gains at the fundamental and selected odd harmonics, ω_c is the cutoff frequency, and ω_{2h-1} is the frequency of the $2h-1$-th odd harmonics. Therefore, the transfer function of open-loop system $G_c(s).G_{sys}(s)$ is

$$G_{op}(s) = \frac{a_1 s^{14} + a_1 s^{13} + \cdots + a_{15}}{b_1 s^{17} + b_2 s^{16} + \cdots + b_{18}} \tag{2.15}$$

where $a_1, \cdots, a_{15}$ are the nominator and $b_1, \cdots, b_{18}$ are the dominator coefficients of open-loop system. As shown in (2.15), the system loop is 17^{th} order. Therefore, tuning the multi-resonant PR controller parameters is a challenging task. To select the controller parameters, different contradictory constraints should be considered. The first one is the requirement of steady-state error for the grid current. It is related to the magnitude of the

loop gain at the fundamental frequency f_g. The second and the last constraints are the gain margin and the phase margin respectively. Hence, a satisfactory region detection for the controller parameters is complex [46]. It is worth mentioning that if the steady-state error, phase margin, and gain margin specifications are excessively strict, the parametric region may be very small or perhaps non-existent. Therefore, in the literature, a simple PR controller is designed for the fundamental component and then its gain is used for all harmonic compensators.

The nine parameters ω_c, K_P, K_{i1}, K_{i3}, K_{i5}, K_{i7}, K_{i9}, K_{i11}, and K_{i13} need to be selected for the proposed quasi-PR current controller. The first one is ω_c which is related to the grid frequency by $2\pi f_g \Delta f_g$ [47]. To design ω_c, the standard limit of grid frequency variation Δf_n is considered $\pm 1\%$; thereby leading to $\omega_c \approx 3$. This value can satisfy a desirable bandwidth around the resonant frequencies. The application of optimization theories is vastly adopted in modern power systems [48], [49]. Also in this chapter, to determine the next eight quasi-PR controller parameters, PSO, GA, and a combination of PSO and GA named PSO-GA are employed. The objectives of the optimization algorithm are to improve dynamic behavior, stability margins, and reduce the steady-state error at selected odd harmonics. In the rest of this sub-section, firstly, the PSO, GA, and PSO-GA algorithms are briefly reviewed and then an optimum quasi-PR current controller is designed.

2.4.4.2 Optimization algorithms definition

The most popular optimization method is the PSO algorithm. The PSO evolutionary algorithm imitates the social interaction of flocks of birds. It makes sufficient use of probabilistic transition rules to do parallel searches of the huge solution space. The feasibility and

simplicity of the PSO algorithm make it a popular method for many optimization problems. The PSO algorithm utilizes a swarm of particles, which seek out a multidimensional search space to find the best solution. Each particle has the potential to be the best solution and is affected by the neighbor's experiences. In each iteration of PSO algorithm, $i-$th particle have a present position $x_i(t)$, previous position $x_i(t-1)$, and moving velocity $v_i(t)$ in the $t-$th iteration. The position and velocity of the particle are updated as follows

$$\begin{cases} x_i(t) = x_i(t-1) + v_i(t) \\ v_i(t) = Wv_i(t-1) + c_1\rho(pbest - x_i(t-1)) + \cdots \\ \qquad + c_2\rho(gbest - x_i(t-1)) \end{cases} \tag{2.16}$$

where W is the PSO inertia weight, c_1 and c_2 are acceleration factors and ρ is a uniformly distributed random number between 0 and 1. The variables $pbest$ and $gbest$ are the personal best experience and global best experience respectively. From equation (2.16), it is obvious that each particle velocity contains three parts. The first one introduces the searching ability of the PSO. The second one is related to the personal experience of the particle, called private thinking, and the last one is related to the global experience of all particles, named collaboration thinking. The PSO coefficients c_1, c_2 determine the movement speed of particles to $pbest$ and $gbest$ locations. Particles may become away from target zones with small values of c_1, c_2. However, large values of these coefficients may result in fast movement in the searching zone. Many research works proved that the acceleration constants c_1 and c_2 should be selected between 1 and 2 [50]. The inertia weight W is chosen to make a balance between global and local exploration which results in less number of iterations to find a relatively optimal solution [51]. Figure 2.7 shows the flowchart of the proposed PSO algorithm.

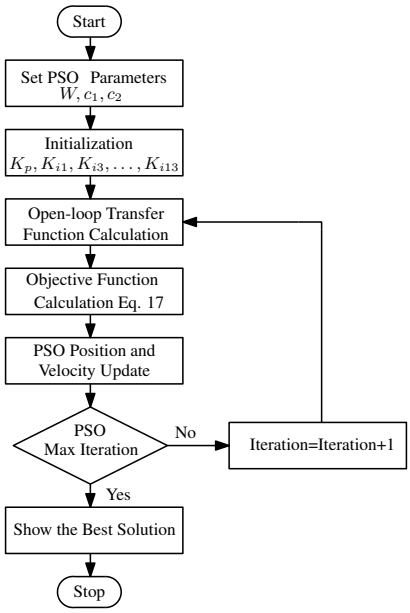

Figure 2.7: The PSO algorithm flowchart.

Another popular optimization algorithm is the GA method. This algorithm is based on a natural selection process mimicking biological evolution. First, a random population of individual solutions is considered. Then, crossover and mutation are applied to the current population in order to create new children. The best solutions for the current population and the created children are considered for the next generation. The algorithm will stop searching when a certain criterion is achieved. The flowchart of the proposed GA algorithm is shown in Figure 2.8.

The last optimization technique used in this chapter is the combination of the two previous optimization algorithms, called as PSO-GA. In the PSO-GA, both abilities of PSO and GA coexist in one optimization algorithm [52]. In this method, both operators of PSO and GA, including personal experience, global experience, crossover, mutation, and selection are applied in each iteration. Figure 2.9 shows the flowchart of the proposed PSO-GA algorithm.

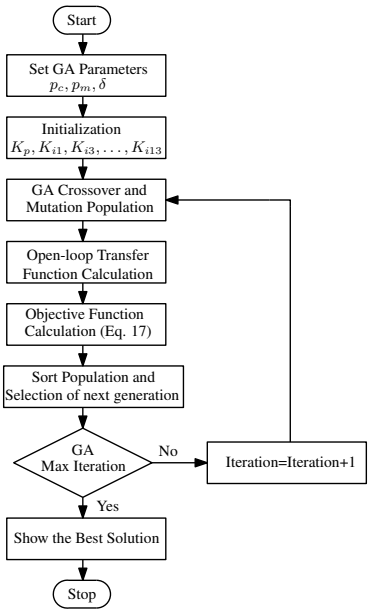

Figure 2.8: The GA algorithm flowchart.

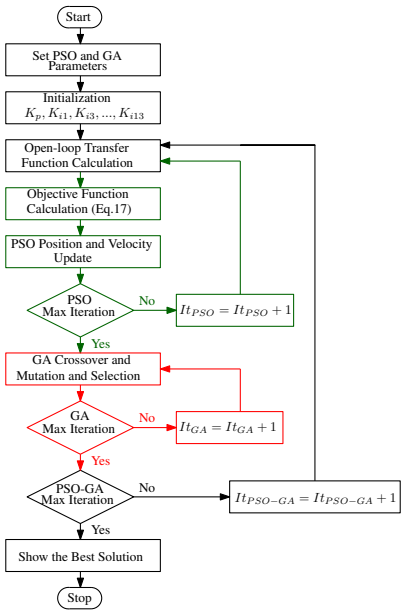

Figure 2.9: The PSO-GA algorithm flowchart.

2.4.4.3 Designing multi-resonant PR parameters by optimization algorithms

In this section, the proposed design approach of multi-resonant controllers' coefficients is presented. The design approach is formulated as an optimization problem. The optimum values for the control system coefficients K_P, K_{i1}, K_{i3}, K_{i5}, K_{i7}, K_{i9}, K_{i11}, and K_{i13} are obtained through different optimization techniques including PSO, GA, and PSO-GA. The objective function is selected to improve the system dynamic behaviour, stability region, and steady-state response and it is expressed as follows

$$\text{Objective Function} = -(Gm + Pm + \alpha \sum_{h=1}^{7} Mag_{2h-1}) \tag{2.17}$$

where Gm, Pm, and Mag_{2h-1} are the gain margin, phase margin, and harmonic magnitudes in the open loop system respectively. It should be noticed that the more magnitude at the selected frequencies, the least steady-state error at that harmonics. The factor α is added to the objective function in order to make a trade-off between stability and steady-state error at selected frequencies. This factor is set to 0.3 based on the authors' experience in the optimization running. The optimization techniques parameters are shown in Table 2.4.

Table 2.4: The optimization techniques parameters.

Parameters	Value
Population size	50
PSO acceleration coefficients	1.5
PSO inertia weight	0.73
GA crossover rate	0.7
GA mutation rate	0.2
Arithmetic crossover parameter	0.1
Search interval of variables	[0,1000]

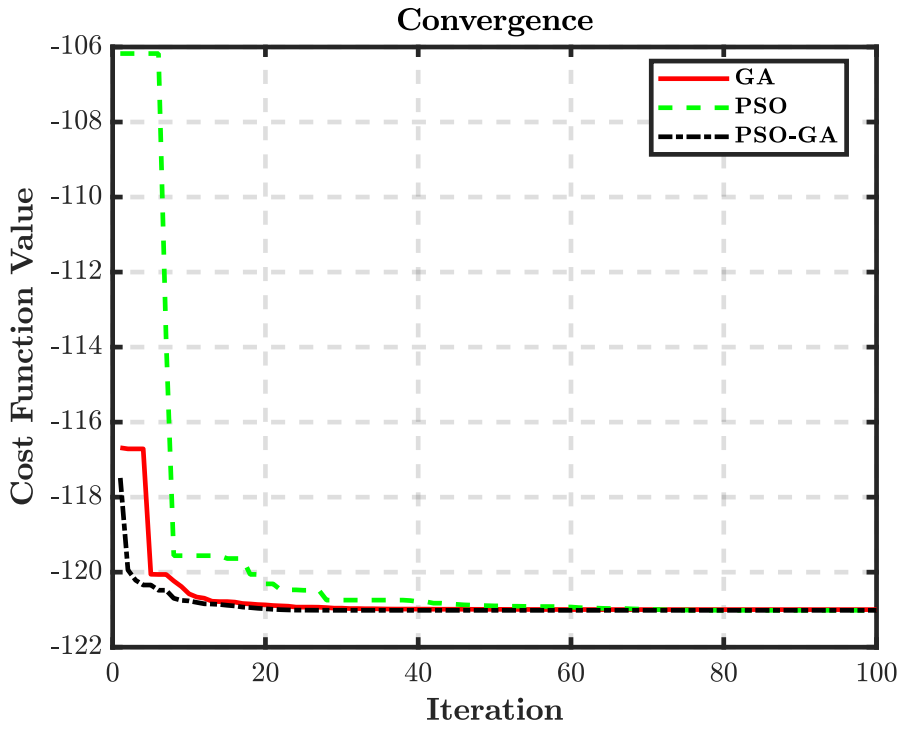

Figure 2.10: The objective function convergence for different optimization algorithms.

The optimum values of the control system coefficients obtained through different optimization techniques are given in Table 2.5.

Figure 2.10 shows the evolution of the objective function in terms of the iteration number with the proposed PSO, GA, and PSO-GA algorithms. The figure shows that the objective function convergence is very close to its optimum value with less than 40 iterations.

Table 2.6 shows the comparative analysis among the PSO-tuned, GA-tuned, and PSO-GA-tuned quasi-PR controllers and conventional PR controller (Conv.) with fixed gains at harmonic compensators. It can be seen that the gain margin, phase margin, and overshoot of the control system designed with optimization algorithms are more desirable than

Table 2.5: The obtained quasi-PR controller parameters through PSO, GA, and PSO-GA algorithms.

Parameters	Conv.	PSO	GA	PSO-GA
K_P	15	15.56	15.71	15.56
K_{i1}	850	650.80	661.91	650.27
K_{i3}	850	635.33	653.22	635.09
K_{i5}	850	605.16	620.66	604.75
K_{i7}	850	559.33	575.42	559.12
K_{i9}	850	498.21	512.82	498.07
K_{i11}	850	421.79	438.28	421.37
K_{i13}	850	328.83	344.44	328.66

the conventionally designed controller. The phase margin, gain margin, and minimum magnitude at selected frequencies for the proposed quasi-PR controller with optimized parameters are obtained as 8.11 dB, 31.8°, and 29.8 dB respectively. These values are appropriate for the practical control systems [53]. With these values, the control system has satisfactory performance in terms of asymptotic stability and steady-state error at selected odd harmonics.

The comparative bode plot of the open-loop system with optimized quasi-PR controllers and the conventional controller is shown in Fig. 2.11 where the previous values of gain margin and phase margin can be appreciated. It is noteworthy that such stable margins cannot be obtained without the necessary damping which had been applied to the system.

Table 2.6: The dynamic performance comparative analysis.

Variable	Conv.	GA	PSO	PSO-GA
Gain Margin	7.01 dB	7.98 dB	8.11 dB	8.11 dB
Phase Margin	20.52°	31.33°	31.85°	31.86°
Overshoot	59.4%	46.9%	46.1%	46.03%
Robustness	Unstable	Stable	Stable	Stable

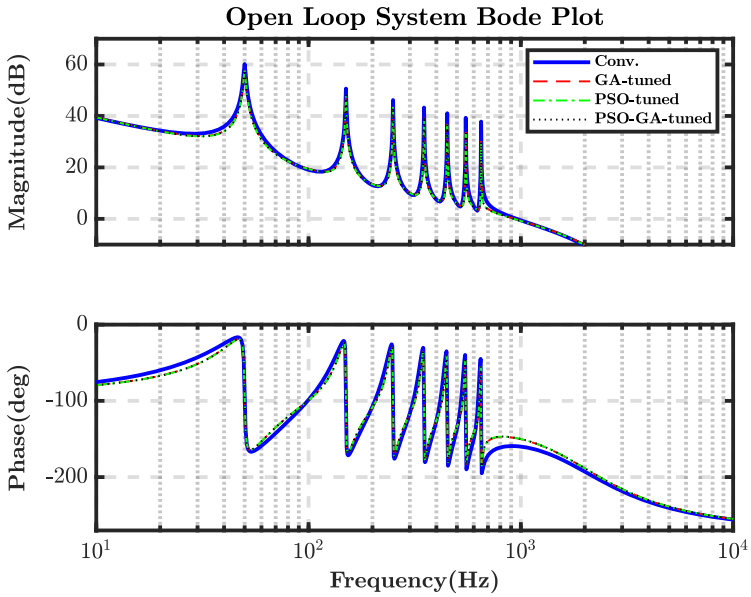

Figure 2.11: The bode-diagram of the open loop system with different controllers.

In Fig. 2.12, the step response of the closed-loop system with optimized quasi-PR controllers has been compared with the conventional PR controller. Moreover, the robustness of the optimized controllers against system parameter changes is shown in Fig. 2.13. The filter inductances and capacitance increase 50% which leads to instability in the system with conventional controller. However, the systems with optimized controllers are still stable. From these figures, it can be seen that the stability and robustness of system has improved with optimized quasi-PR controllers.

2.4.5 Inverter modulation technique

The last step is to obtain switching patterns of the VSI. There are different modulation techniques for three-phase inverters. The sinusoidal PWM (SPWM) and space vector PWM (SVPWM) are the widely used ones. In this chapter, the SPWM technique is used.

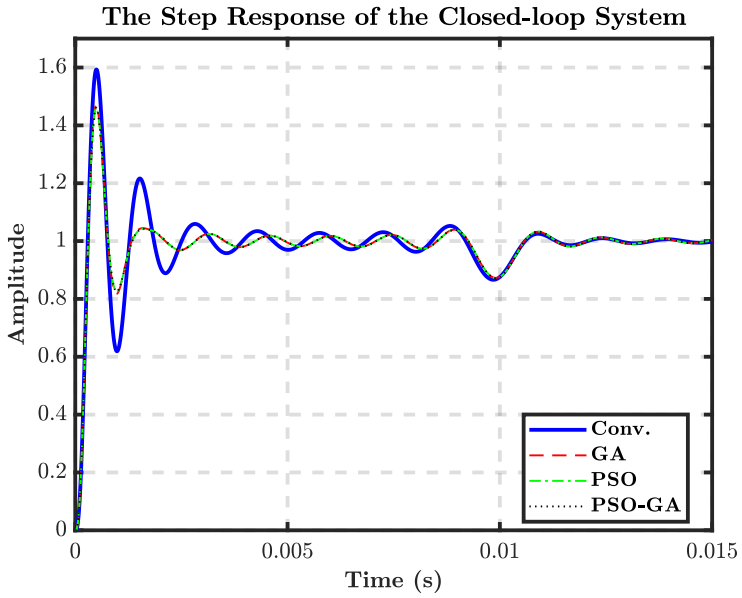

Figure 2.12: The step response of the closed-loop system with different controllers.

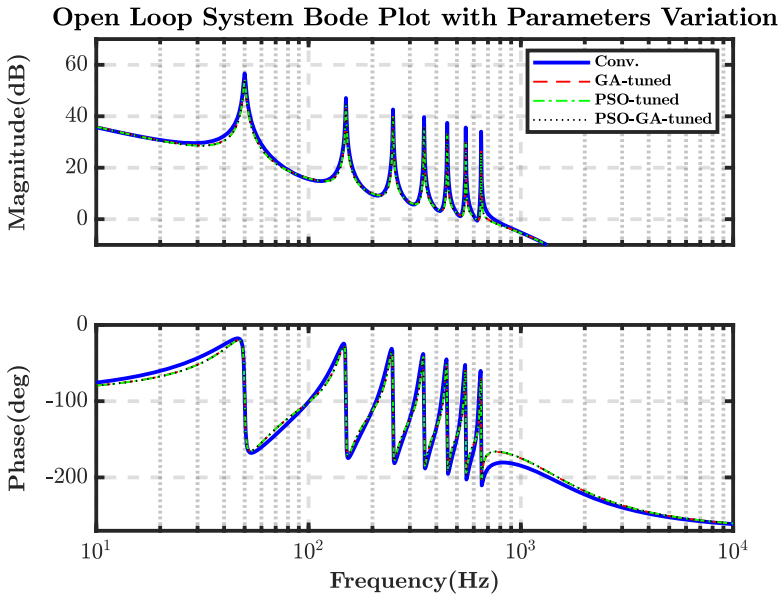

Figure 2.13: The bode-diagram of the open loop system when LCL filter parameters increase by 50%.

In this method, the same amplitude triangular carriers between -1 to 1 are applied for each phase. The switching pattern of VSI is determined as previously shown in Fig. 2.2.

2.5 Simulation results

In this section, the effectiveness of the proposed control approach using optimized controller is validated through numerical simulation performed on PSIM© software. The performance of the system is thoroughly analyzed under PV irradiation step change, nonlinear and unbalanced load step change, and distorted grid voltage. Moreover, the performance of proposed control method is compared with the conventional instantaneous $p-q$ theory. The nonlinear and unbalanced load parameters are given by Table 2.7.

Table 2.7: The nonlinear and unbalanced load parameters.

Variable	Value	Variable	Value
R_{La}	$40\,\Omega$	L_{Lc}	60 mH
R_{Lb}	$20\,\Omega$	R_{L_1}	$20\,\Omega$
R_{Lc}	$10\,\Omega$	R_{L_2}	$20\,\Omega$
L_{La}	60 mH	L_{L_1}	60 mH
L_{Lb}	20 mH	L_{L_2}	100 mH

2.5.1 PV irradiation step change

In the first case study, in order to analyze the PV-fed VSI shunt APF performance, an irradiation step change for the PV is applied at $t = 0.2$ s from $1000\,\mathrm{W/m^2}$ to $700\,\mathrm{W/m^2}$. The three-phase grid current, load current, and grid-side inverter current are illustrated in

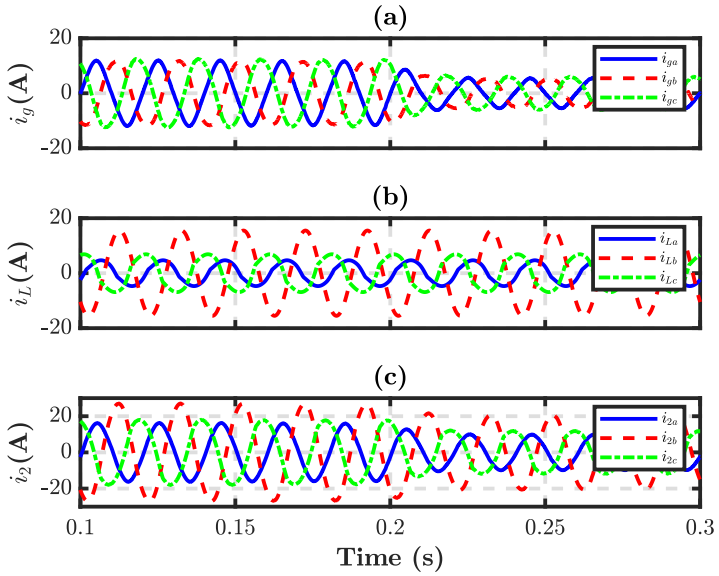

Figure 2.14: The three-phase currents under PV irradiation step change at $t = 0.2$ s: (**a**) grid; (**b**) load; (**c**) inverter.

Fig. 2.14. The grid currents THD are 4.57%, 4.57%, and 3.22% in phase a, b, and c. The harmonic content of nonlinear and unbalanced load three-phase currents i_{La_H}, i_{Lb_H}, and i_{Lc_H} are shown in Fig. 2.15. The performance of MPPT and VBC control are illustrated in Fig. 2.16. As shown in this figure, the PV output voltage is appropriately tracking the reference voltage provided by the MPPT. Moreover, the DC-link voltages in the TLB converter output are balanced.

The grid current and voltage are shown in Fig. 2.17(a). It can be seen in this figure that the grid current and voltage are in phase. It means that the reactive power is effectively compensated. Fig. 2.17(b) and Fig. 2.17(c) illustrate the active and reactive power of the inverter, grid, and load. It can be seen that the injected grid power decreases when the PV output power reduces.

The results from the instantaneous $p - q$ theory and from the proposed method are

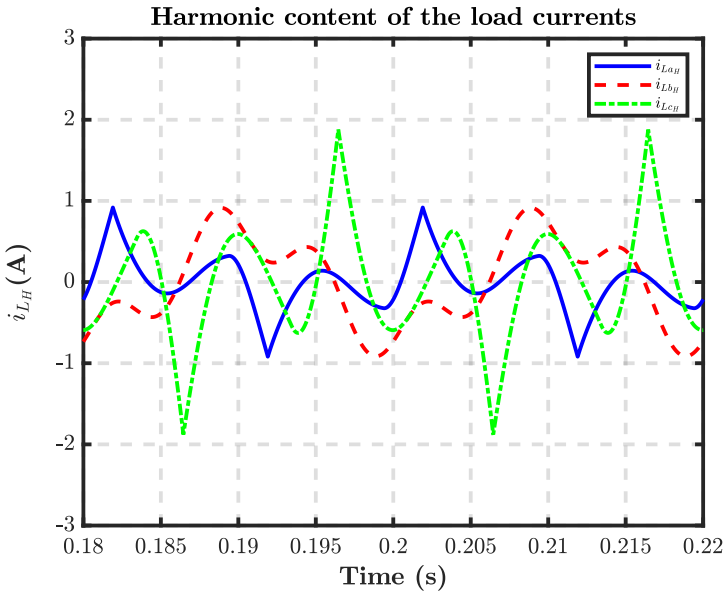

Figure 2.15: The harmonic content of nonlinear and unbalanced load three-phase current.

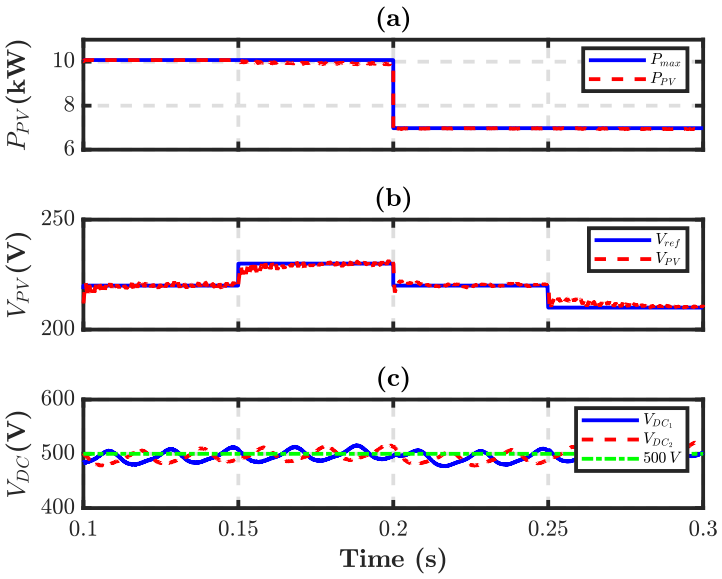

Figure 2.16: The TLB performance under PV irradiation step change at $t = 0.2$ s: (**a**) MPPT power tracking; (**b**) MPPT voltage tracking; (**c**) DC-link voltages.

shown in Fig. 2.18. As shown in this figure, the THD and the current unbalance factor (CUF) of the three-phase grid current for the proposed shunt APF control method are better than instantaneous $p-q$ theory. Namely, the CUF of negative and zero sequences of the grid current are 5% and 1.4% for the proposed shunt APF control method. However, they are 15% and 1.7% for the conventional instantaneous $p-q$ theory.

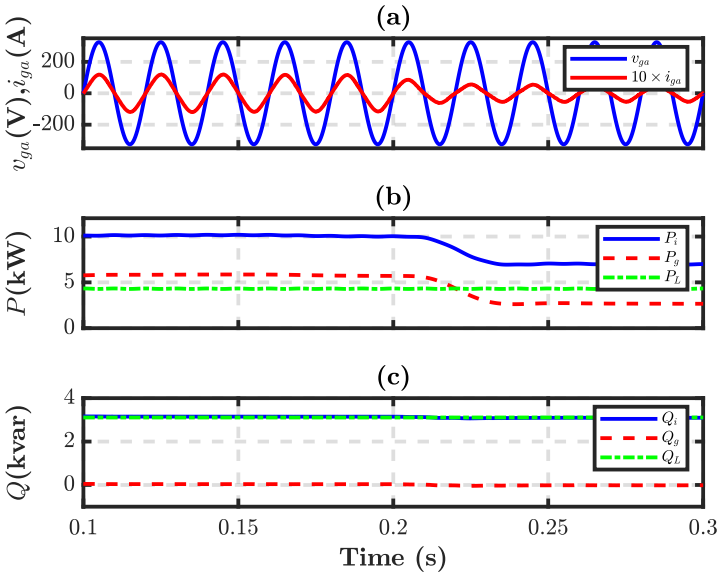

Figure 2.17: The grid current and voltage, active power, and reactive power under PV irradiation step change at $t = 0.2$ s: (**a**) grid current and voltage; (**b**) active power; (**c**) reactive power.

2.5.2 Nonlinear and unbalanced load step change

In the second case study of analyzing the PV-fed shunt APF inverter, a load step change is applied at $t = 0.2$ s. The resistances of R_{Lc}, R_{L_1}, and R_{L_2} reduce to their half values and R_{La} changes to $8\,\Omega$ at $t = 0.2$ s. The three-phase grid current, load current, and grid-side inverter current are illustrated in Fig. 2.19. The nonlinear and unbalanced load three-phase

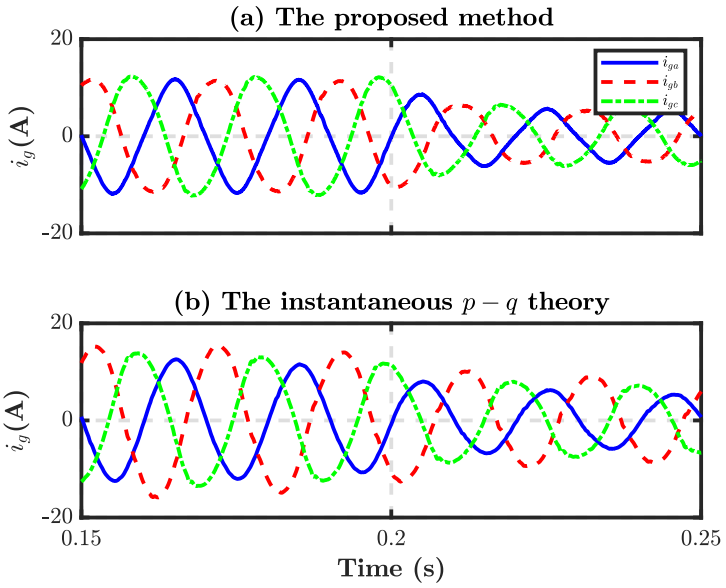

Figure 2.18: The comparison of three-phase grid current between instantaneous $p-q$ theory and the proposed control method under PV irradiation step change.

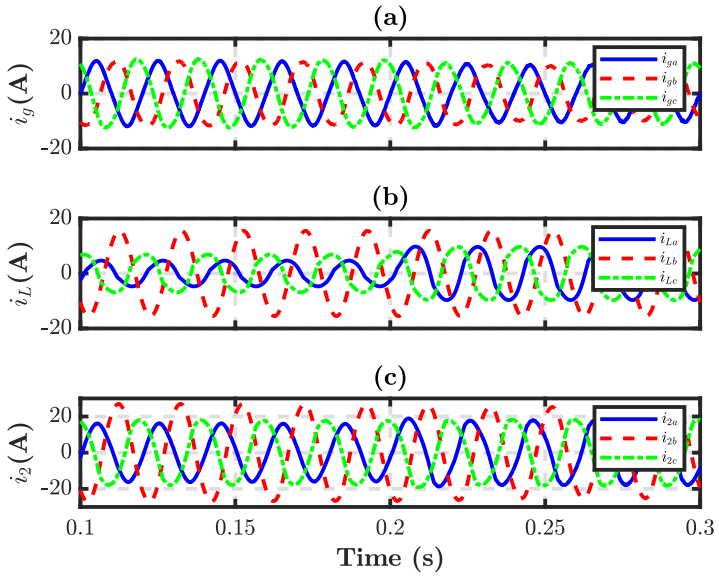

Figure 2.19: The three-phase currents under load step change at $t = 0.2$ s: (**a**) grid; (**b**) load; (**c**) inverter.

current and its harmonic content are shown in Fig. 2.20. The performance of MPPT and VBC control under load step change is depicted in Fig. 2.21. As shown in this figure, the MPPT and VBC are properly tracking the references.

In Fig. 2.22(a), the grid current and voltage are illustrated. As shown in this figure, the grid current and grid voltage are in phase. Therefore, the load reactive power is totally compensated through the VSI. The active and reactive power of the inverter, the grid, and the load are illustrated in Fig. 2.22(b) and Fig. 2.22(c). The PV power is fixed at 10 kW. Therefore, when the load power undergoes a step change, the main grid's active power decreases.

The three-phase grid current is shown in Fig. 2.23 for both when the instantaneous $p-q$ theory used and the proposed control method. From this figure, the THD of i_{ga}, the THD of i_{gb}, the THD of i_{gc}, negative sequence CUF, and zero sequence CUF are 5.34%, 5.79%, 3.8%, 8.2%, and 2.34% for the proposed shunt APF control method respectively. These values validate the more satisfactory performance of the proposed method in comparison with conventional instantaneous $p-q$ theory.

2.5.3 Distorted grid voltage

The performance of the proposed PV-fed shunt APF inverter is also analyzed under distorted grid voltages. The third harmonic with a magnitude of 60 V is added to the grid voltage v_{ga}. The three-phase distorted grid voltage is illustrated in Fig. 2.24. The three-phase grid current, load current, and grid-side inverter current are illustrated in Fig. 2.25. The grid currents THD with the proposed control method are 5.87%, 5.12%, and 3.73% while they are 10.33%, 7.97%, and 8% with instantaneous $p-q$ theory. In addition,

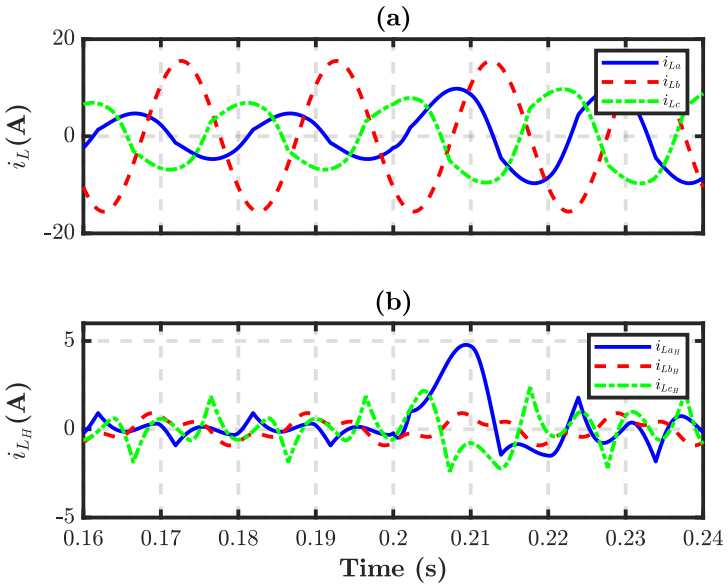

Figure 2.20: Nonlinear and unbalanced load three-phase current and its harmonic content.

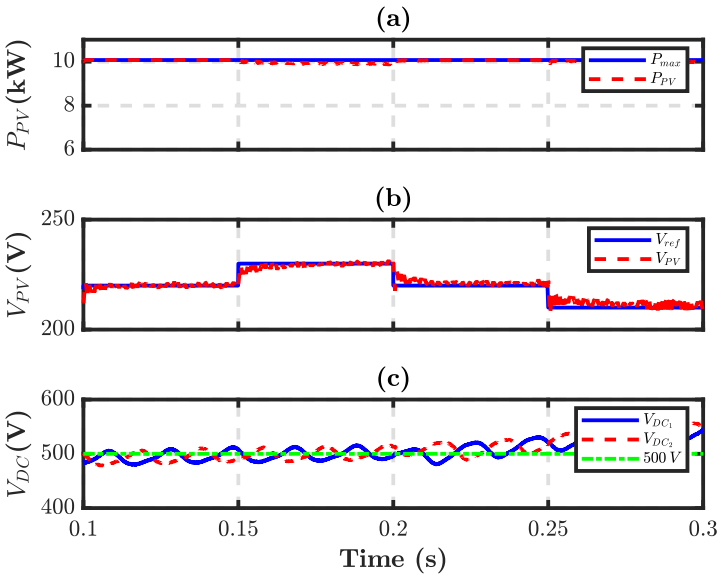

Figure 2.21: The TLB performance under load step change at $t = 0.2$ s: (**a**) MPPT power tracking; (**b**) MPPT voltage tracking; (**c**) DC-link voltages.

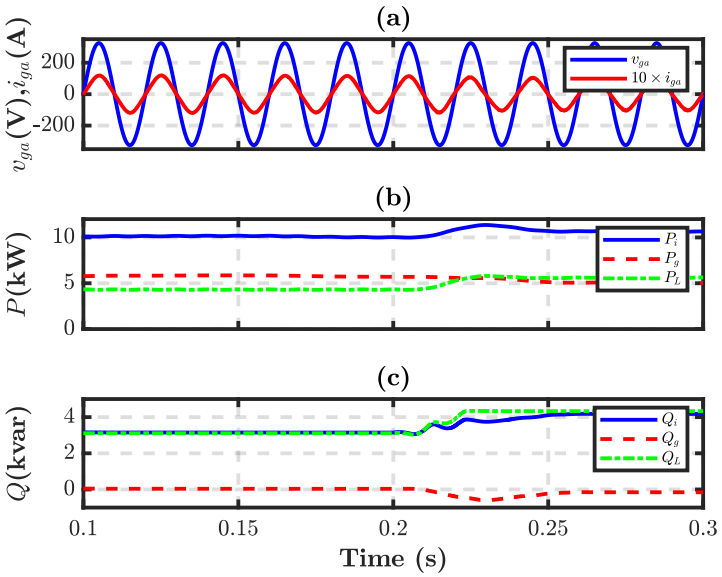

Figure 2.22: The grid current and voltage, active power, and reactive power under load step change at $t = 0.2$ s: (**a**) grid current and voltage; (**b**) active power; (**c**) reactive power.

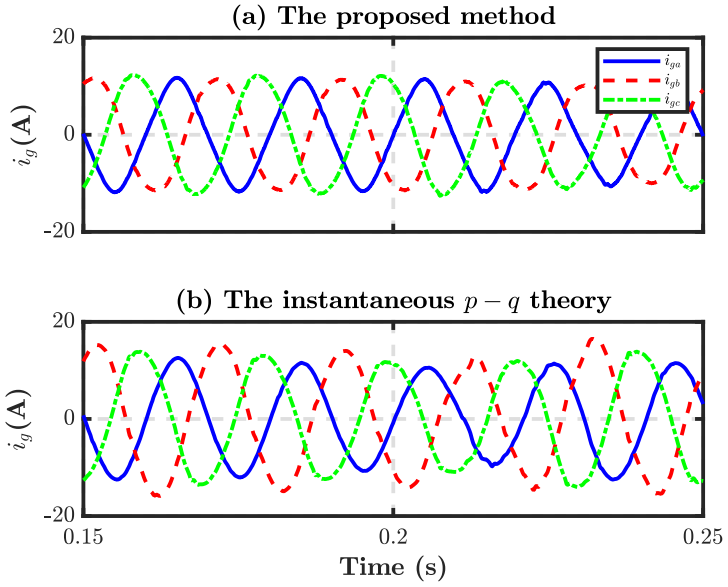

Figure 2.23: The comparison of three-phase grid current between instantaneous $p - q$ theory and the proposed control method under load step change.

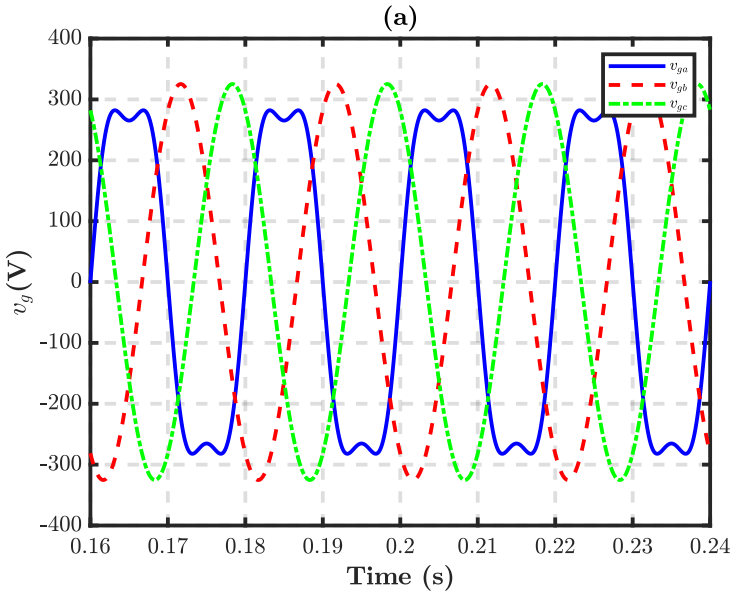

Figure 2.24: The distorted grid voltages.

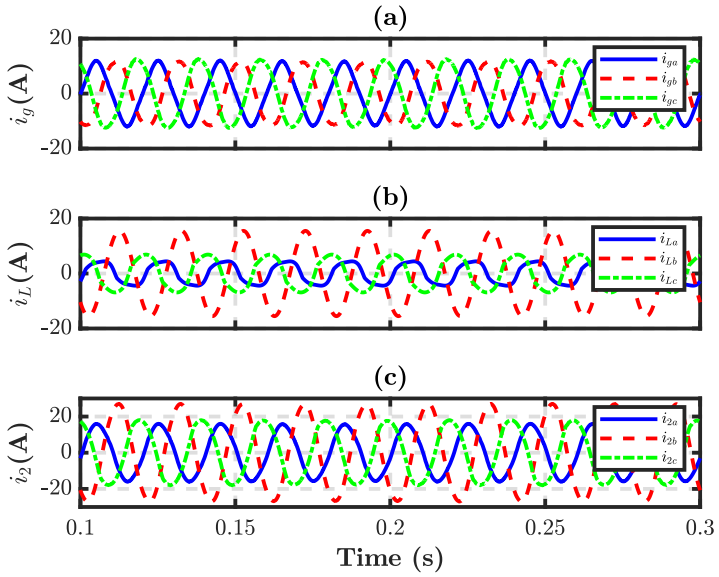

Figure 2.25: The three-phase currents under distorted grid voltage: (**a**) grid; (**b**) load; (**c**) inverter.

the three-phase grid current negative and zero CUF with the proposed control method are 8.2% and 2% respectively. However, they are 24.2% and 3% with instantaneous $p-q$ theory.

The performance of MPPT and VBC control under distorted grid voltage is illustrated in Fig. 2.26. It can be seen from this figure that the MPPT control and VBC have the desirable performances.

The grid current and voltage are illustrated in Fig. 2.27(a). As shown in this figure, there is no any reactive power consumption from the main grid. Fig. 2.27(b) and Fig. 2.27(c) illustrate the active and reactive power of the inverter, the grid, and the load. The PV power is fixed at P_{max}, 10 kW.

The instantaneous $p-q$ theory and the proposed control method are compared in Fig. 2.28. It can be observed that the three-phase grid current with the proposed shunt APF control method is balanced and has less harmonic pollution than the conventional instantaneous $p-q$ theory.

The comparative analysis of the proposed control method and the conventional instantaneous $p-q$ theory for different case studies are given by Table 2.8.

Table 2.8: The grid current THD and CUF in both instantaneous $p-q$ and proposed method for different case studies.

Variables	PV irradiation step change		Load step change		Distorted grid voltage	
	$p-q$ theory	proposed method	$p-q$ theory	proposed method	$p-q$ theory	proposed method
THD of i_{ga}	9.25%	4.57%	6.21%	5.34%	10.33%	5.87%
THD of i_{gb}	5.65%	4.57%	7.84%	5.79%	7.97%	5.12%
THD of i_{gc}	10.12%	3.22%	6.69%	3.8%	8%	3.73%
CUF I_g^- / I_g^+	15%	5%	15.6%	8.2%	24.2%	8.2%
CUF I_g^0 / I_g^+	1.7%	1.4%	2.56%	2.34%	3%	2%

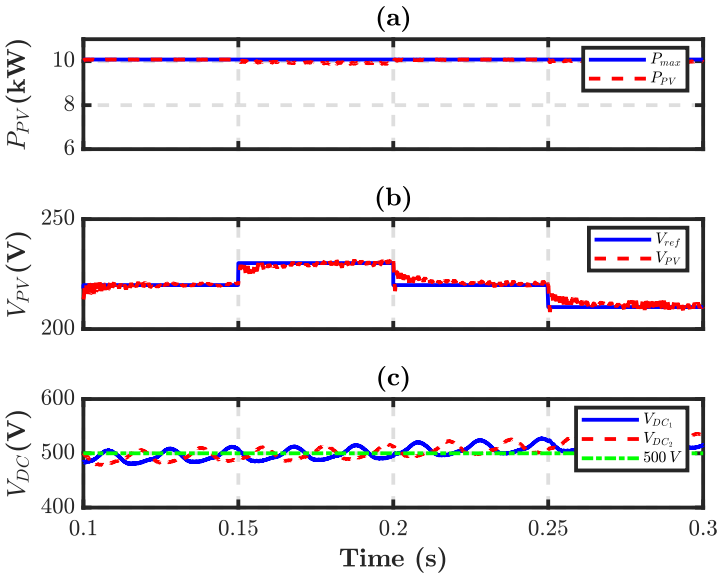

Figure 2.26: The TLB performance under distorted grid voltage: (**a**) MPPT power tracking; (**b**) MPPT voltage tracking; (**c**) DC-link voltages.

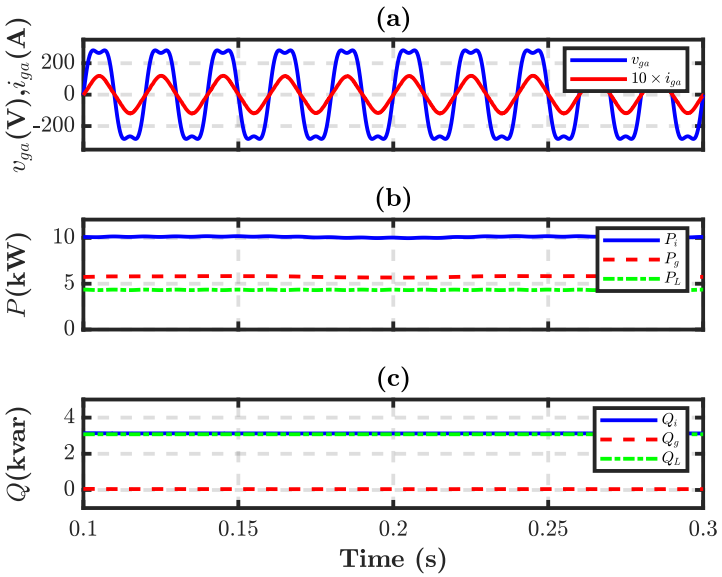

Figure 2.27: The grid current and voltage, active power, and reactive power under distorted grid voltage: (**a**) grid current and voltage; (**b**) active power; (**c**) reactive power.

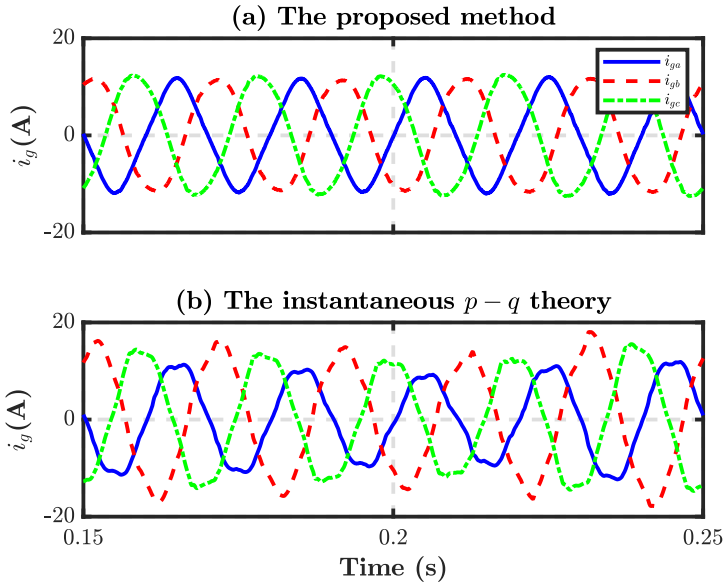

Figure 2.28: The comparison of three-phase grid current between instantaneous $p-q$ theory and the proposed control method under distorted grid voltage.

2.6 Conclusions

In this chapter, the control of a PV-fed multifunctional grid-connected inverter has been addressed. The studied system consists of a TLB, a three-phase VSI, an LCL output filter, and a nonlinear and unbalanced load. The shunt APF control strategy has been presented to control the grid-side three-phase inverter current. A quasi-PR controller was employed to track the sinusoidal references properly due to the presence of nonlinear local load, containing harmonic pollution. To determine controller parameters, optimization algorithms with novel objective function have been used. The parameters of the objective function have been chosen based on static and dynamic performances. Each harmonic compensator of the quasi-PR controller has its own resonant gain with zero steady-state error at that particular harmonic. By virtue of the proposed control method, the PV-fed VSI can act as a shunt APF, capable of compensating harmonic currents, reactive power,

and load unbalanced sequences. The proposed method with an optimized controller shows superiority against the conventional control technique. Its effectiveness has been verified by detailed simulations performed on the switched model of the system implemented in PSIM© software. Its advantages can be summarized as follows

- Injecting the PV power adaptively in grid-connected application with low grid current THD;
- Desirable performance under irradiation step change, load step change, and distorted grid-voltage;
- Operating of the VSI as a shunt APF and a reactive power compensator;
- Removing zero and negative sequences from the main grid current and desirable CUF;
- Optimized quasi-PR controller for grid-side inverter current control;
- Desirable dynamic stability and reference tracking for the control system.

Chapter 3

Islanding Operation of a Microgrid

3.1 Abstract

Load and supply parameters may be uncertain in MGs due for instance to the intermittent nature of renewable energy sources among others. Guaranteeing reliable and stable MGs despite parameter uncertainties is crucial for their correct operation. Their stability and dynamical features are directly related to the controllers' parameters and power-sharing coefficients. Hence, to maintain power good quality within the desirable range of system parameters and to have a satisfactory response to sudden load changes, careful selection of the controllers and power-sharing coefficients are necessary. In this chapter, a simple design approach for the optimal design of controllers' parameters is presented in an islanded MG. To that aim, an optimization problem is formulated based on a small-signal state-space model and solved by three different optimization techniques including PSO, GA, and a proposed approach based on the combination of both PSO and GA. The optimized coefficients are selected to guarantee desirable static and dynamic responses in a wide range of operations regardless of the number of inverters, system configuration, output

impedance differences, and load types. Through the proposed design and tuning method, the performance of the MG is improved as compared to those obtained using state-of-art techniques. This fact is demonstrated by using numerical simulations performed on a detailed model implemented in PSIM© software.

3.2 Introduction

With the use of distributed renewable energy sources that can be utilized locally to produce and feed electric power, the concept of MGs has emerged. The MGs have two operating modes: grid-connected and islanded mode [54]. The issue of power balance between production and consumption, which is equivalent to the load and frequency control has been one of the major challenges in the islanded mode of operation [14]. Imbalances between DGs and loads in MGs create frequency fluctuation which leads to a decrease in power quality or even may put the system stability at risk [55]. Furthermore, high penetration of renewable energies in MGs can bring uncertainties due to unpredictable environmental changes in terms of solar irradiance, temperature, wind speed, etc. [56]. Therefore, a robust control technique is needed to guarantee the small-signal stability of MGs despite load or source changes. In the islanded mode of operation, the most usable controller is the PI corrector which is implemented in a two-loop hierarchical structure. Namely, power control is performed by an outer control loop with low bandwidth while an inner control loop with higher bandwidth than the outer loop is responsible for voltage and current control [9]. The responsibility of the inner current and voltage controller loops is to track voltage and current reference values during disturbances as well as to damp output filter resonances [57]. The aim of the outer loop is to guarantee active and reactive power-sharing with other DGs. Various types of power-sharing control strategies

have been proposed in islanding operation of MGs [58], e.g., master/slave control [59], distributed control [60], and droop control [15]. Among them, the droop control strategy inspired by the behaviour of synchronous generators has more advantages such as the capability of applying in both modes of MG operations, needless communication lines among DGs, and plug-and-play functionality [61].

Based on the type of common bus voltages, MGs are classified into AC [62], DC [63] and hybrid AC/DC [64]. In the case of AC MGs, voltage-source inverters (VSI) are used as interfaces between the common bus voltage and the load. These VSIs have lower physical inertia in comparison with synchronous generators [65] which means that their dynamic response is much faster. This fast dynamic response makes them vulnerable in front of different disturbances. Therefore, for the reliable operation of MGs, small-signal stability is required in a wide range of operations [66]. The power quality and stability of MGs are affected by droop control coefficients and controllers' parameters. In [67], it is proved, by using root locus and sensitivity analysis, that the low-frequency eigenvalues of the MG are strictly sensitive to the droop controller parameters. Therefore, the selection of controllers' coefficients needs careful attention [16] to satisfy MG power quality conditions and smooth and stable operation during load changes. In addition, by optimally selecting these parameters, it is conceivable that the islanded MG can be stable in a wide range of operations with less voltage and frequency steady-state errors. Also, in [68], even with similar parallel inverters and identical parameters, the uncertainty brought by different output impedances might destabilize the system. Different approaches have been presented in the literature to select the controllers' coefficients [69]. The most used ones are based on a trial and error approach which is time-consuming, especially in a complex MG and the tuned parameters are not the optimum ones. Furthermore, this approach does not provide a systematic guideline for the design of controllers' coefficients in the MGs. Another

approach is to design the controllers' parameters in such a way that the dynamics of the outer loop be slower than that of the inner loop [70]. Under this assumption, the inner and outer control loops can be separately designed. Normally, the bandwidth of the outer loop is limited to $1/10$ of the inner loop [71]. However, this approach has similar disadvantages to the trial and error method. The last approach to design the controllers' coefficients is to employ optimization algorithms such as GA [72] and PSO. They are widely used in the MGs for different areas, such as harmonic mitigation [73] and optimal scheduling [74]. The authors in [75] used the PSO algorithm to optimally select the MG control parameters. In their approach, the problem constraints are not exactly specified which can jeopardize the stability of the MG. In addition, the objective function can only remove the steady-state error of the active power. In [76] a two-layer PSO algorithm was used for parameter selection in the inverter side inductor current control theory framework. In that work, only the effect of PI controller parameters was investigated. However, the impact of power-sharing coefficients is also important and the choice of these parameters is critical [77]. In [78] an online intelligent method, based on the combination of fuzzy logic and PSO techniques, was proposed for the selection of PI parameters to control the MG frequency. In [79] Grasshopper Optimization Algorithm (GOA) was used, and in [80] PSO was used to tune the PI controller parameters. PSO was also used in [81] to design triple-action controllers' parameters for an islanded AC MG. In [82], GA was used to design controller parameters in the secondary control level of an AC MG, and in [83] a non-dominated sorting genetic algorithm-II was used to design the parameters for the fractional order PID controller. However, the performance of GA shows premature convergence in some cases [84].

None of the above-mentioned references provides a universal and simple design approach to tune the controllers' parameters which guarantees the small-signal stability in the

whole range of operation. In this chapter, regardless of the number of inverters, MG configuration, output line impedance, or types of loads, a straightforward design approach is presented. This can minimize designers' efforts to the tuning MG controllers' parameters when the output impedances, the number of inverters, and MG configuration may change. Since the VSIs are interfaced to a common bus voltage with huge coupling inductances and the distribution lines have resistive-inductive impedances, it can be concluded that the stable and optimal operation of each VSI can guarantee stable and optimal operation of the whole MG provided that interacting effects are neglected. Therefore, in the proposed design approach, the small signal analysis of a VSI is considered. A novel eigenvalues-based objective function is defined which involves stability criteria eliminating the need of performing sophisticated stability analysis and making the control design method simpler than traditional techniques. Power controller coefficients, PI current and voltage controller gains are determined through the optimization problem which is solved through different algorithms such as PSO, GA, and proposed PSO-GA intending to improve both system static and dynamic performances. The proposed combined PSO-GA uses both PSO and GA. The controllers' coefficients can be determined off-line for the worst-case scenario of the operating point. In order to validate the proposed method, different case studies including load changes in the two-inverter system are simulated in the islanded mode of operation using PSIM© software. A comparative analysis among optimization algorithms is carried out for the different case studies. The main contributions of the chapter are listed below.

- Proposing a new simple design approach and tuning method for the optimal setting of power, voltage, and current controllers' coefficients.

- Proposing novel objective function evaluating optimized parameters for the controllers while ensuring the VSI stability in the whole range of operation.
- Proposing a combination of PSO and GA for parameter tuning for a VSI in an MG application.

The rest of this chapter is organized as follows. In, Section 3.3, a complete small-signal model of the VSI inverter in an MG application is derived. Section 3.4 is devoted to defining the proposed design approach and formulating the optimization problem which is solved through GA, PSO, and the proposed PSO-GA algorithm. Section 3.5 presents simulation results for different case studies. Section 3.6 concludes the chapter.

3.3 State-Space Modelling of the Inverter

Figure 3.1 shows the control schematic diagram of a VSI in an islanded MG. The used control strategy consists of power, voltage, and current controllers in a hierarchical structure. The current controller is the fastest one and the power controller is the slowest one. The control is implemented in the dq reference frame. The most appropriate and simplest controller in this frame is a PI controller [85] which is used in this study, for both current and voltage loops. For the power controller, the droop control method is employed. As the inverter is connected to the AC common bus through an inductor (L_c), the power control can be carried out by using two artificial linear characteristics in the inverter frequency and voltage as shown in Figure 3.2. The frequency is set based on droop gain m_p and the voltage is set according to the droop gain n_q. The inverter phase can be determined

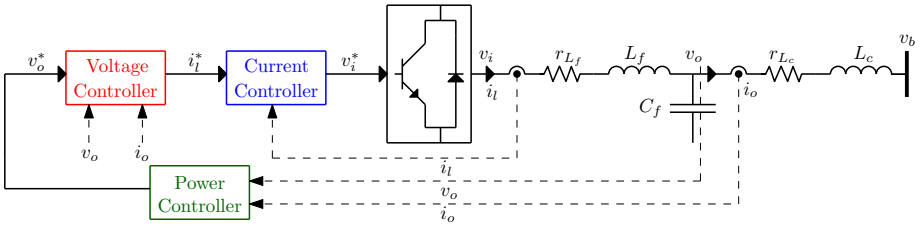

Figure 3.1: The control schematic diagram of an islanded MG.

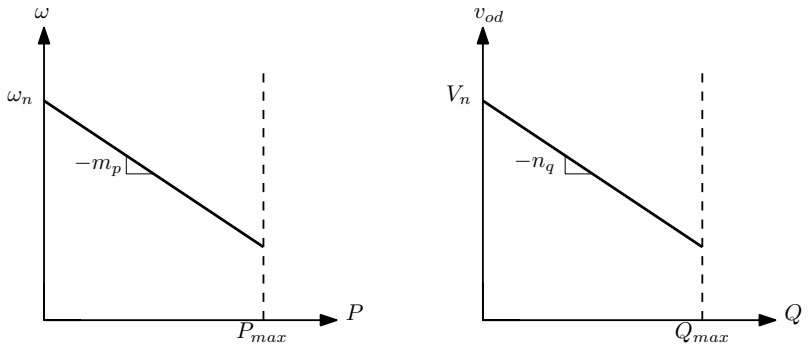

Figure 3.2: Artificial linear characteristics with the slope of $-m_p$ for the inverter frequency and the slope of $-n_q$ for the inverter voltage.

by integrating the frequency. Droop control technique arises from synchronous generator governor and inertia characteristics. As an example, when the generator has drawn, power increases, and the rotation speed decreases [86]. Therefore, MG active and reactive power can be controlled in the dq reference frame by manipulating inverter output voltage magnitude and frequency as follows:

$$\begin{cases} \omega = \omega_n - m_p P \\ v_{od}^* = V_n - n_q Q \\ v_{oq}^* = 0 \end{cases} \tag{3.1}$$

where ω_n and V_n are the nominal frequency and voltage respectively. P and Q are the DC components of instantaneous active and reactive power. It should be noted that in presence

of more than one inverter in the MG, to build the complete small-signal model, the rotation speed of one inverter δ should be considered as a reference frame. Then, all other inverters' rotation speeds should translate to the one which is considered as a reference. Figure 3.3 illustrates the block diagram of the control scheme in dq reference frame. First, measured currents and voltages go through the dq transform block. Then, DC values of active and reactive power are calculated with a low pass filter. The low pass filter is used to guarantee the proper current sharing of nonlinear loads [87]. According to the dq synchronous reference frame theory, harmonic components will appear in the nonlinear load active and reactive power. These should be removed from the DC values. The DC values of active and reactive power enter the frequency and voltage droop loops and build the rotation angle and d-axis voltage reference value for the outer voltage controllers. The q-axis voltage reference value is set to zero. Thereafter, the outputs of PI voltage controllers plus a portion of dq-axis voltages and dq-axis output currents make the reference value of inner current controllers. The calculated reference value for the inverter voltage goes through an inverse dq transform block to build three-phase signals for the inverter pulse width modulation.

A complete small-signal model of an islanded MG, which is detailed by [67], [88], is briefly presented here. Combining the state-space model of power, voltage, and current controllers and linearizing the models at the operating point yields to (3.2).

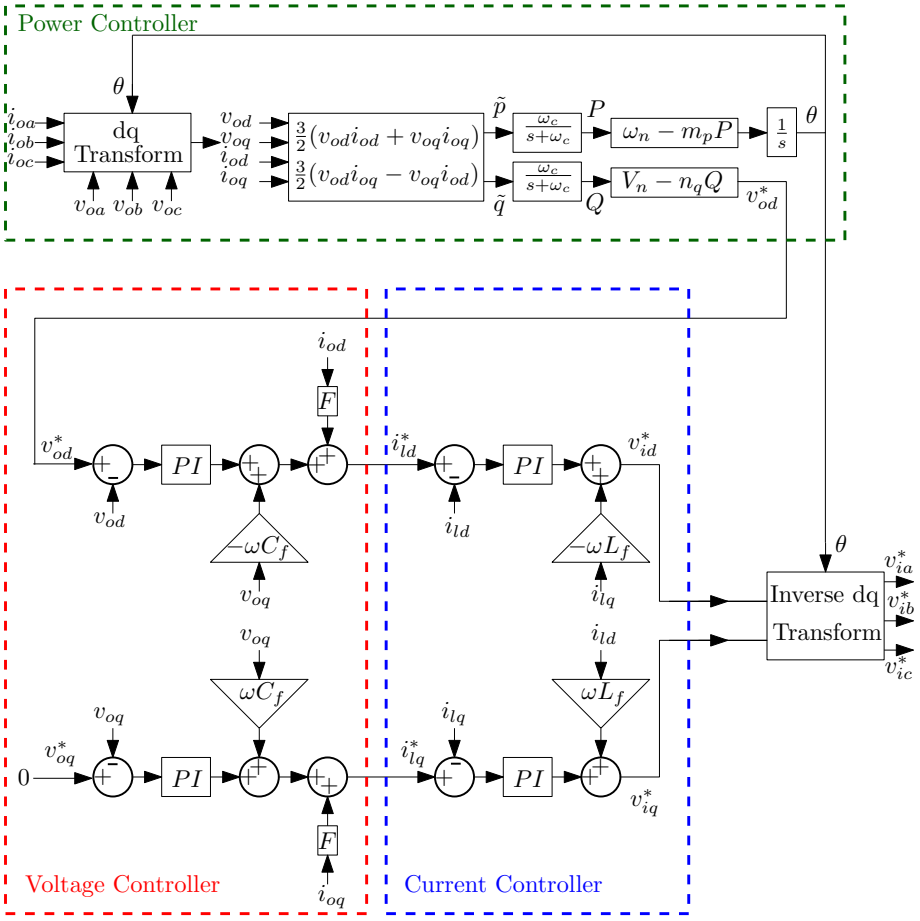

Figure 3.3: Block diagram of control scheme in *dq* reference frame.

$$\begin{bmatrix} \Delta\dot{\delta} \\ \Delta\dot{P} \\ \Delta\dot{Q} \\ \Delta\dot{\phi}_d \\ \Delta\dot{\phi}_q \\ \Delta\dot{\psi}_d \\ \Delta\dot{\psi}_q \\ \Delta\dot{i}_{ld} \\ \Delta\dot{i}_{lq} \\ \Delta\dot{v}_{od} \\ \Delta\dot{v}_{oq} \\ \Delta\dot{i}_{od} \\ \Delta\dot{i}_{oq} \end{bmatrix} = \begin{bmatrix} 0 & -m_p & 0 & 0 & 0 & 0 & 0 & 0 & 0 & 0 & 0 & 0 & 0 \\ 0 & -\omega_c & 0 & 0 & 0 & 0 & 0 & 0 & 0 & \omega_c I_{od} & \omega_c I_{oq} & \omega_c V_{od} & \omega_c V_{oq} \\ 0 & 0 & -\omega_c & 0 & 0 & 0 & 0 & 0 & 0 & \omega_c I_{oq} & -\omega_c I_{od} & -\omega_c V_{oq} & \omega_c V_{od} \\ 0 & 0 & -n_q & 0 & 0 & 0 & 0 & 0 & 0 & -1 & 0 & 0 & 0 \\ 0 & 0 & 0 & 0 & 0 & 0 & 0 & 0 & 0 & 0 & -1 & 0 & 0 \\ 0 & 0 & -n_q K_{pv} & K_{iv} & 0 & 0 & 0 & -1 & 0 & -K_{pv} & -\omega_n C_f & F & 0 \\ 0 & 0 & 0 & 0 & K_{iv} & 0 & 0 & 0 & -1 & \omega_n C_f & -K_{pv} & 0 & F \\ 0 & -m_p I_{lq} & \frac{-n_q K_{pc} K_{pv}}{L_f} & \frac{K_{pc} K_{iv}}{L_f} & 0 & \frac{K_{ic}}{L_f} & 0 & \frac{-r_{L_f} - K_{pc}}{L_f} & \omega_0 - \omega_n & \frac{-K_{pc} K_{pv} - 1}{L_f} & \frac{-\omega_n C_f K_{pc}}{L_f} & \frac{F K_{pc}}{L_f} & 0 \\ 0 & m_p I_{ld} & 0 & 0 & \frac{K_{pc} K_{iv}}{L_f} & 0 & \frac{K_{ic}}{L_f} & \omega_n - \omega_0 & \frac{-r_{L_f} - K_{pc}}{L_f} & \frac{\omega_n C_f K_{pc}}{L_f} & \frac{-K_{pc} K_{pv} - 1}{L_f} & 0 & \frac{F K_{pc}}{L_f} \\ 0 & -m_p V_{oq} & 0 & 0 & 0 & 0 & 0 & \frac{1}{C_f} & 0 & 0 & \omega_0 & -\frac{1}{C_f} & 0 \\ 0 & m_p V_{od} & 0 & 0 & 0 & 0 & 0 & 0 & \frac{1}{C_f} & -\omega_0 & 0 & 0 & -\frac{1}{C_f} \\ \frac{-V_{bq}}{L_c} & -m_p I_{oq} & 0 & 0 & 0 & 0 & 0 & 0 & 0 & \frac{1}{L_c} & 0 & -\frac{r_{L_c}}{L_c} & \omega_0 \\ \frac{-V_{bd}}{L_c} & m_p I_{od} & 0 & 0 & 0 & 0 & 0 & 0 & 0 & 0 & \frac{1}{L_c} & -\omega_0 & -\frac{r_{L_c}}{L_c} \end{bmatrix} \begin{bmatrix} \Delta\delta \\ \Delta P \\ \Delta Q \\ \Delta\phi_d \\ \Delta\phi_q \\ \Delta\psi_d \\ \Delta\psi_q \\ \Delta i_{ld} \\ \Delta i_{lq} \\ \Delta v_{od} \\ \Delta v_{oq} \\ \Delta i_{od} \\ \Delta i_{oq} \end{bmatrix} \tag{3.2}$$

In (3.2), ϕ_d, ϕ_q, ψ_d, and ψ_q are the state variables of current and voltage controllers. V_{bd}, V_{bq}, I_{ld}, I_{lq}, I_{od}, I_{oq}, V_{od}, V_{oq} are the operating points of the MG and ω_c is the cut-off frequency of power controller. $K_{pv}, K_{iv}, K_{pc}, K_{ic}$ are the proportional and the integral gains of the voltage and current controllers respectively while F is the gain of dynamic improvement loop. As it is shown in (3.2), the state matrix for an islanded MG with only one inverter has 13×13 dimension. Therefore, it has 13 eigenvalues and their locus in the complex plain are shown in Figure 3.4. The comparison of the small-signal average

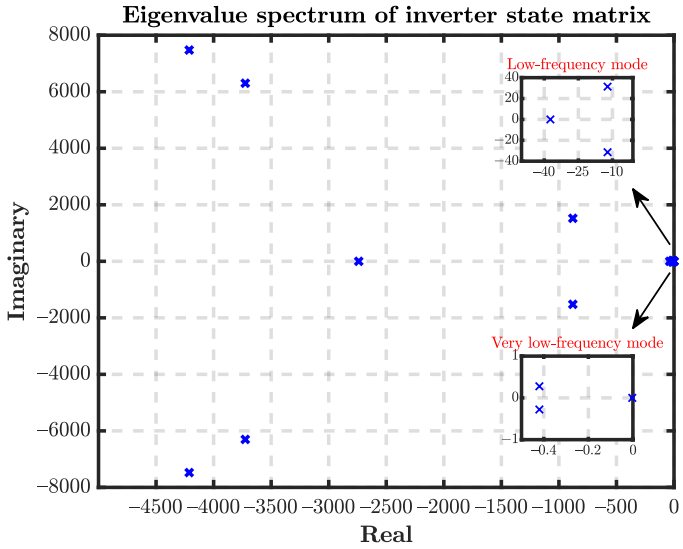

Figure 3.4: The eigenvalues of the small-signal model of the islanded MG with one inverter.

model of the islanded MG with one inverter and the large-signal switched model is shown in Figure 3.5. The islanded MG operation point changes from a normal one to another operating condition with 100% load step change.

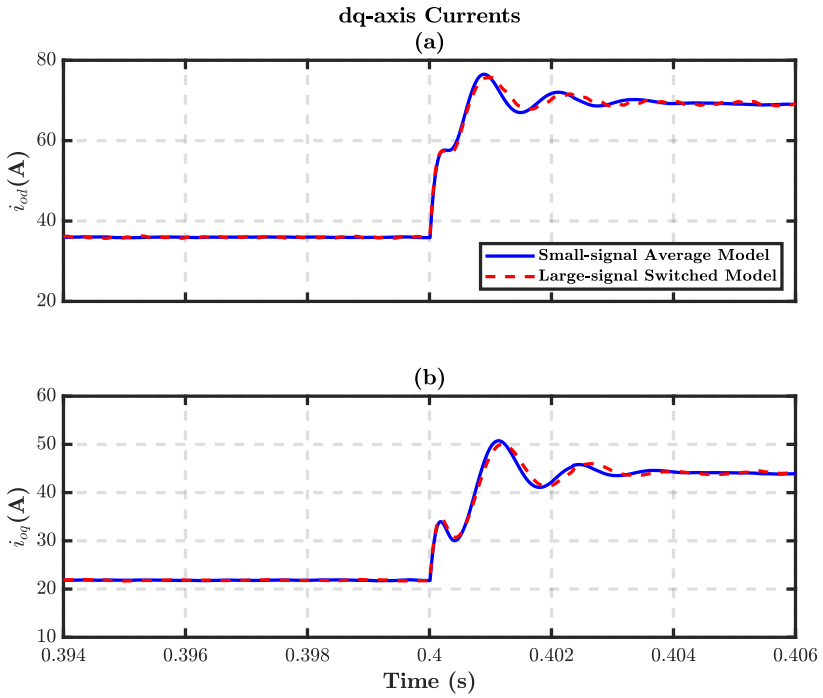

Figure 3.5: The validation of the small-signal model of the islanded MG with one inverter: (**a**) d-axis current; (**b**) q-axis current.

3.4 Proposed Design Approach

In this section, the proposed design approach of controllers' coefficients is presented. The design approach is formulated as an optimization problem to find the best-fitted values for the control system coefficients $[m_p\ n_q\ K_{pv}\ K_{iv}\ K_{pc}\ K_{ic}]$. The optimization problem is solved through different optimization techniques including PSO, GA, and the proposed PSO-GA which is the combination of PSO and GA.

3.4.1 Formulation of Optimization Problem

The aim of minimising the objective function is to improve system dynamic behaviour and damping characteristics as well as to keep the stability of the whole system under load changes. This can be done by making all the eigenvalues of the state matrix with a damping ratio close to an appropriate value [89]. The selection of damping ratio is to make a trade-off between magnitude and time of system overshoot. Therefore damping ratio selection is a subjective choice and is usually selected between 0.4 and 0.7. As it is mentioned previously, the state matrix of the inverter has 13 eigenvalues all can be expressed as follows

$$s = -\zeta\omega_n \pm j\omega_n\sqrt{1-\zeta^2} \tag{3.3}$$

where ζ and ω_n are the modes damping ratio and natural frequency. In this chapter, the objective function is selected in such a way that all the 13 system eigenvalues are such that the damping ratio is 0.5. Another important thing is the stability of the closed-loop system with PI controllers. To have a stable system, a term is added to the objective function to guarantee the stability of the whole system with designed controller parameters. This term

is `isstable()` function in MATLAB environment which returns zero when a state matrix is unstable and returns one when it is stable. Adding this term to the objective function eases the stability analysis of the system. Therefore, the resulted parameters through all optimization algorithms guarantee the stability of the whole system. The definition of the objective function is illustrated in the following equation

$$\text{Objective Function} = -\texttt{isstable}\left(\text{state matrix}\right) + \sqrt{\frac{\sum_{i=1}^{13}(\zeta_i - 0.5)^2}{13 \times 0.25}} \tag{3.4}$$

where in the denominator of the objective function second term, 13×0.25 would normalize the value between 0 and 1 [90].

3.4.2 Proposed PSO-GA

The proposed optimization technique is the combination of two powerful optimization algorithms, PSO and GA, and is called here PSO-GA. The proposed PSO-GA provides both powers of PSO and GA in one optimization algorithm. PSO has the ability to traverse the search space continuously like birds flocking to find the optimum value. Furthermore, it is powerful for solving multiobjective optimization problems. However, PSO may stick in the local optima and suffer from low-quality solutions. The ability of GA can solve this problem since the candidate solutions are randomized and muted. Moreover, GA has the ability in both continuous and discrete optimization problems. Therefore, in the proposed PSO-GA, the risk of sticking to local optimums significantly decreases. The proposed PSO-GA starts with population initialization. Then, PSO operators are applied in a predetermined sub-iteration of PSO. Thereafter, GA operators including crossover, mutation,

and selection are applied to the fitted population in a predetermined sub-iteration of GA. Finally, the best population is drawn when the iteration condition of PSO-GA is satisfied. Figure 3.6 shows the flowchart of the proposed PSO-GA algorithm.

3.4.3 Designing Controllers' Coefficients for a Case Study

Table 3.1 shows the considered values of the islanded MG, including a VSI, an LC output filter, and a grid coupling inductance. In order to select the cutoff frequency of the low pass filter for the power controller, a trade-off between filtering capability and dynamic response exists. The lower the cutoff frequency, the better the filtering feature but the slower the dynamic response. To make this trade-off, the best cutoff frequency proposed in the literature is within 5–25 Hz [91]. Therefore, in this chapter, the cutoff frequency is selected as $5\,\mathrm{Hz}$ ($\omega_c = 31.41\,\mathrm{rad/s}$). It should be noted that, since the low pass filter frequency is fixed and included in the state-space matrix, the designed voltage and current controller parameter ranges obtained from optimization algorithms will not interfere with the low pass filter cutoff frequency ranges. To compare the performance of different optimization techniques, a case study is considered. The operating point values for the case study are shown in Table 3.2.

PSO, GA, and the PSO-GA algorithms are run offline. The number of population, PSO parameters [92], [93], GA coefficients [94], and search interval of variables are shown in Table 3.3. The controllers' parameters are calculated with the different optimization algorithms and are shown in Table 3.4. In addition, the designed parameters based on Ziegler–Nichols method, labelled as conventional (conv.), are taken from [67] to make a comparison with the proposed methods in this chapter. Figure 3.7 shows the convergence

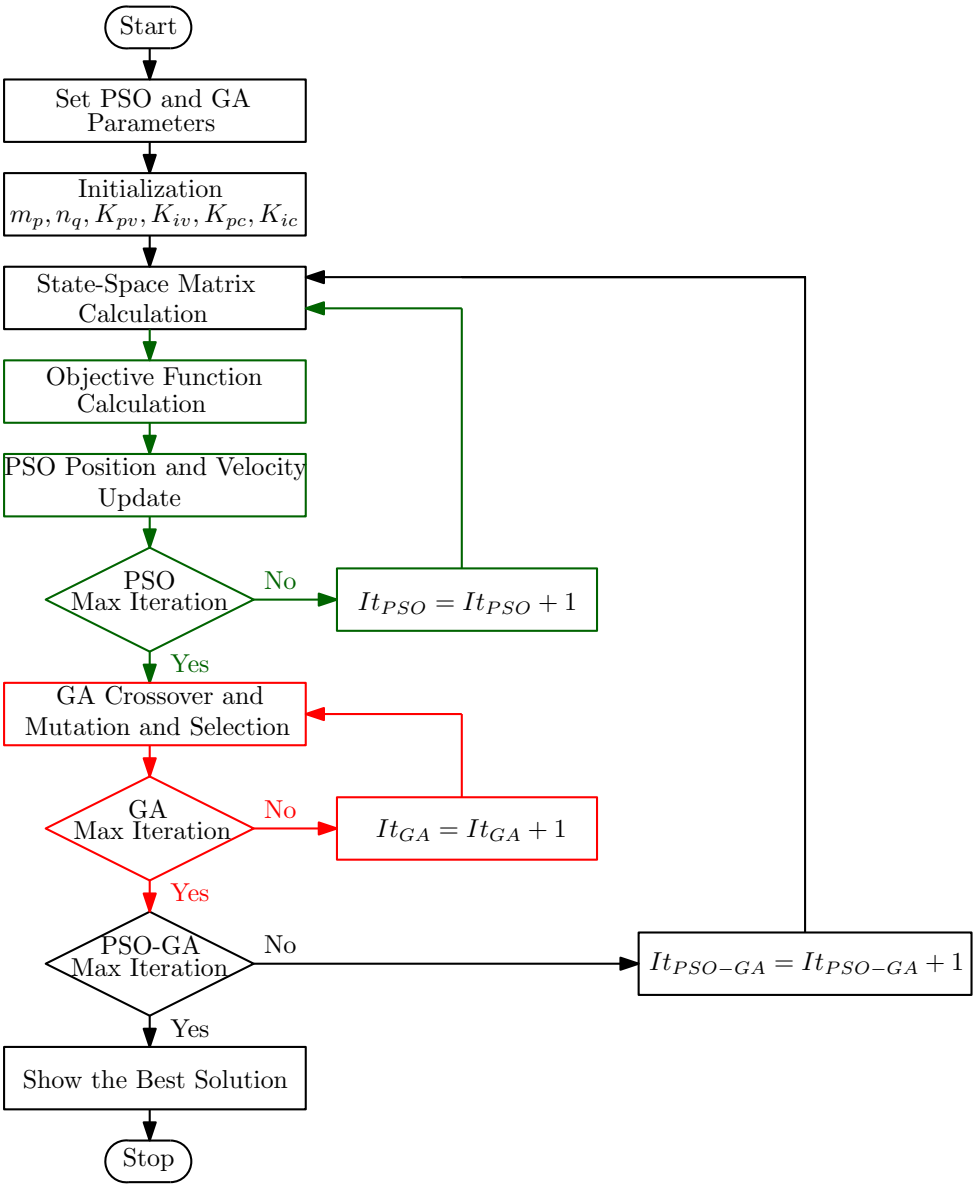

Figure 3.6: The proposed PSO-GA algorithm flowchart.

Table 3.1: The network parameters.

Parameters	Symbol	Value
Filter inductance	L_f	1.35 mH
Filter capacitance	C_f	50 µF
Grid coupling inductance	L_c	0.35 mH
Power controller bandwidth	ω_c	31.41 rad/s
Filter inductor resistance	r_{L_f}	0.1 Ω
Filter capacitor resistance	r_{L_c}	0.03 Ω
Switching frequency	f_s	8 kHz
Nominal frequency	f_n	50 Hz
Dynamic improvement loop	F	0.75
MG nominal power	S	50 kVA

Table 3.2: The operating point values of MG.

Parameters	Value	Parameters	Value	Parameters	Value
V_{od}	380 V	V_{oq}	0 V	V_{bd}	380 V
I_{od}	0 A	I_{oq}	−50 A	V_{bq}	0 V

of the three used optimization techniques. As it can be seen from this figure, the PSO-GA converges in less than 100 iterations and the value of the objective function is improved.

Table 3.3: The optimization techniques parameters and search interval of variables.

Parameters	Value	Variable	Search Interval
Population size	100	m_p	$[0, 5 \times 10^{-3}]$
PSO acceleration coefficients	2	n_q	$[0, 5 \times 10^{-3}]$
PSO inertia weight	1	K_{iv}	[0, 100,000]
GA crossover rate	0.7	K_{pv}	[0, 100,000]
GA mutation rate	0.2	K_{ic}	[0, 100,000]
Arithmetic crossover parameter	0.4	K_{pc}	[0, 100,000]

Table 3.4: The controllers' parameters.

Parameters	Conventional	GA	PSO	PSO-GA
m_p	9.4×10^{-5}	3.54×10^{-5}	4.34×10^{-7}	3.91×10^{-7}
n_q	1.3×10^{-3}	1.87×10^{-4}	3×10^{-4}	1.42×10^{-5}
K_{iv}	390	29.85	406.09	980.89
K_{pv}	0.05	0.2	1.386	1.386
K_{ic}	16,000	37,469.11	43,762.88	1564.94
K_{pc}	10.5	19.40	3740.72	10

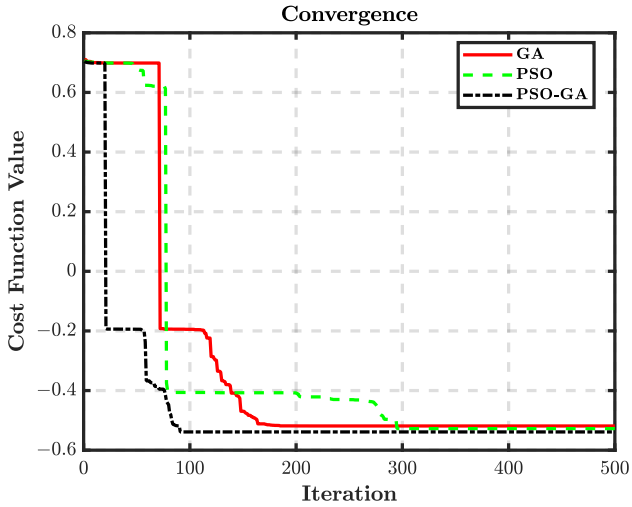

Figure 3.7: Convergence of the objective function with different optimization algorithms.

3.4.4 Effect of Operating Point Changes

As it can be seen in Figure 3.4, there are three frequency modes as follows:

- High-frequency modes which consist of seven poles;
- Low-frequency modes which consist of three poles;
- Very low-frequency modes which consist of three poles.

In addition, the small-signal state-space matrix of the inverter is related to the operating point, $V_{bd}, V_{bq}, I_{ld}, I_{lq}, I_{od}, I_{oq}, V_{od}, V_{oq}$. The very low-frequency modes are so close to the right half-plane. Therefore, they have an inherent capability to jeopardize the inverter stability when the operating point changes. The changes in the MG common bus voltages v_b are normally small as the common bus is supported by different sources of energy in the MG. The reference value for v_{bd} is set to the nominal voltage V_n, 380 V and the reference value for v_{bq} is set to 0 V. Nevertheless, the trace of inverter eigenvalues when $200 \leq V_{bd} \leq 380$ and $-20 \leq V_{bq} \leq 20$ is shown in Figure 3.8. It should be noted that v_o is imposed by v_b since there is a negligible voltage drop along coupling inductance; hence, V_{od} and V_{oq} are approximately the same as V_{bd} and V_{bq}. Similarly, in the nominal frequency, the filter capacitor has a huge impedance; so its current is significantly smaller than the inverter output current. As a result, I_{ld} and I_{lq} are approximately the same as I_{od} and I_{oq}. The ranges of I_{od} and I_{oq} are related to the maximum active power P_{max} and maximum reactive power Q_{max} of the DG which can be obtained by the following

$$\begin{aligned} 0 \leq I_{od} \leq I_{od}^{max} &= \frac{P_{max}}{1.5\ V_{od}} \\ I_{oq}^{min} = -\frac{Q_{max}}{1.5\ V_{od}} \leq I_{oq} \leq I_{oq}^{max} &= \frac{Q_{max}}{1.5\ V_{od}} \end{aligned} \tag{3.5}$$

The trace of inverter eigenvalues when $0 \leq I_{od} \leq 75$ and $-50 \leq I_{oq} \leq 50$ is shown

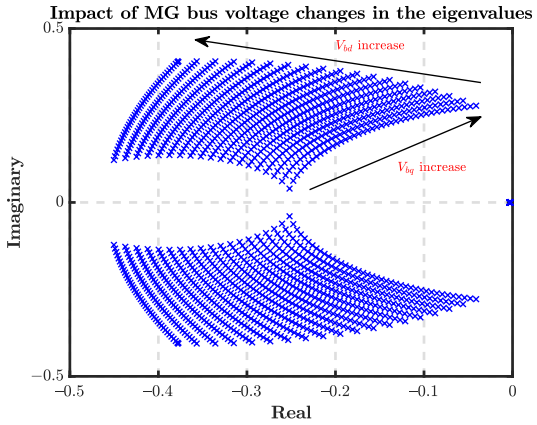

Figure 3.8: The trace of eigenvalues for $200 \leq V_{bd} \leq 380$ and $-20 \leq V_{bq} \leq 20$.

in Figure 3.9. As it can be seen in this figure, the worst case scenario for the inverter stability would happen when I_{od} is zero and I_{oq} is I_{oq}^{min}. Therefore, if the control system coefficients are designed for the worst-case scenario, they would guarantee the stability of the inverter in the whole range of operating points. This is the reason why the operating point in Table 3.2 is chosen.

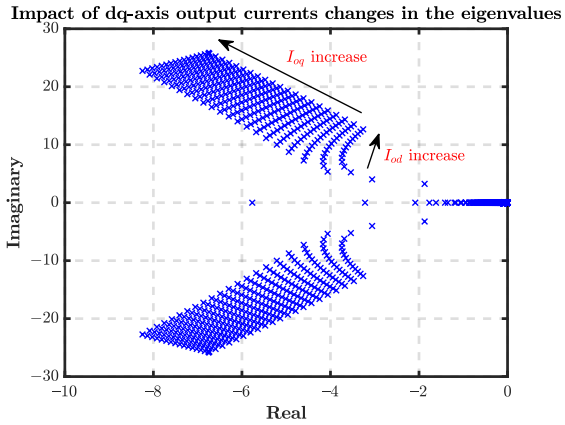

Figure 3.9: The trace of eigenvalues for $0 \leq I_{od} \leq 75$ and $-50 \leq I_{oq} \leq 50$.

3.4.5 Effect of Output Impedance Changes

As it is shown in (3.2), the state-space matrix of the inverter is also dependent on the output impedance ($r_{L_c} + j\omega L_c$). The impact of its changes in the very low-frequency modes is shown in Figure 3.10. From this figure, it can be concluded that the system is stable for a wide range of output impedance. In case of huge output impedance changes, the optimization problem can run again with the new values of output impedances to optimally select the controllers' parameters.

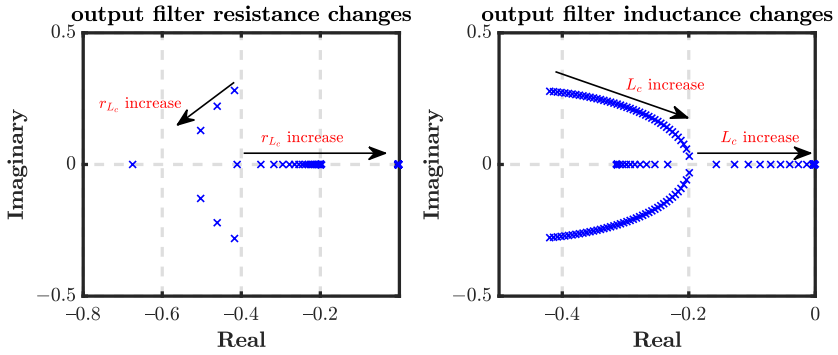

Figure 3.10: The eigenvalues loci for $0\,\Omega \leq r_{L_c} \leq 10\,\Omega$ and $0.35\,\text{mH} \leq L_c \leq 3\,\text{mH}$.

3.4.6 Plug-and-Play Capability of the Design Approach

Plug-and-play functionality and MG configuration independency of the proposed design approach with three different inverters and output impedances are illustrated in Figure 3.11. The controller parameters for each inverter are selected by solving the optimization problem. The value of inverter output filter, output impedance, and worst case scenario of operation point are the input variables for the optimization problems. The output values of the optimization problem are the controller parameters for each inverter. In the case

of adding a new DG to the AC common bus, the optimization problem will be solved to optimally select the controller parameters of the newly added DG.

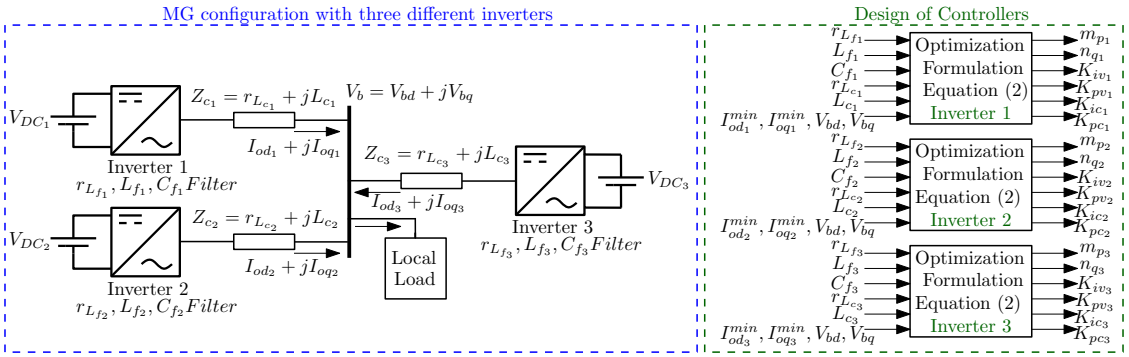

Figure 3.11: The design of MG controllers for three different inverters with different output impedances.

3.5 Simulation Results

In this section, the effectiveness of the proposed design approach using the GA, PSO, and the PSO-GA optimization algorithms is validated through numerical simulation performed in PSIM© software. The simulation is carried out for three different case studies to show the robustness of the designed controllers against various disturbances and in different MG configurations. The first one is a one-inverter system with a linear load and the second one is a one-inverter system with a nonlinear load. The last case study is a higher-order system with two inverters and a linear load. A comparative analysis among different optimization algorithms is performed in each case study.

3.5.1 Case Study I: One Inverter with Linear Load

Figure 3.12 shows the first case study considered in this chapter. First, a linear three-phase load is connected to the islanded MG ($R = 5\,\Omega$, $L = 1\,\text{mH}$). A 100% load step change is applied to the islanded MG at $t = 0.4$ s. The load three-phase current is shown in Figure 3.13. The controllers' parameters were previously presented in Table 3.4.

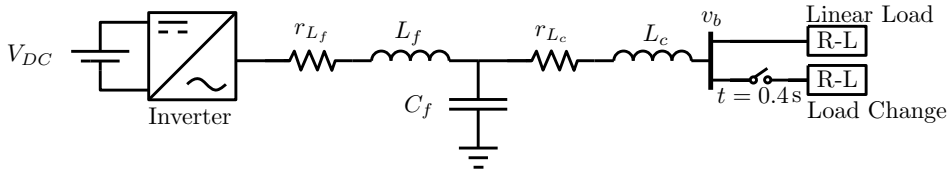

Figure 3.12: The first case study.

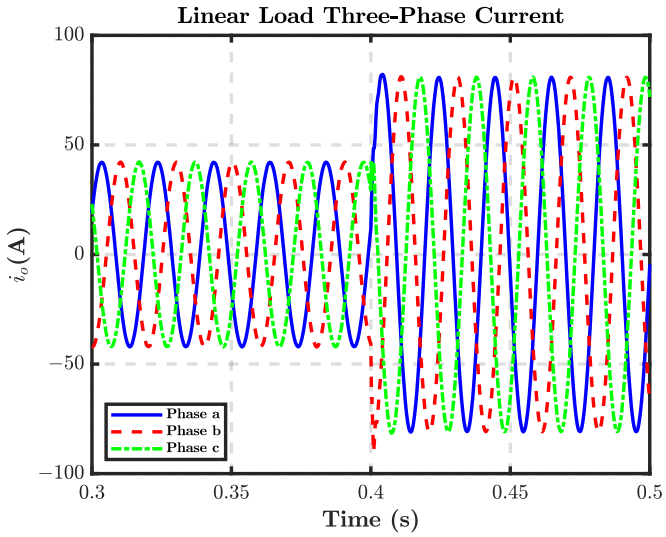

Figure 3.13: Linear load three-phase currents.

Figure 3.14 shows the evolution of the frequency of the islanded MG under linear load step changes. As it can be observed from this figure, the desired steady-state frequency of the MG in which controllers' parameters are selected with PSO and PSO-GA is more accurate

than that obtained from other designed controllers. The steady-state values of frequency after load step change with conventional, GA, PSO, and PSO-GA parameters are 49.46, 49.76, 49.971, and 49.972 Hz respectively. Figure 3.15 shows the dq-axis output currents with different designed controllers.

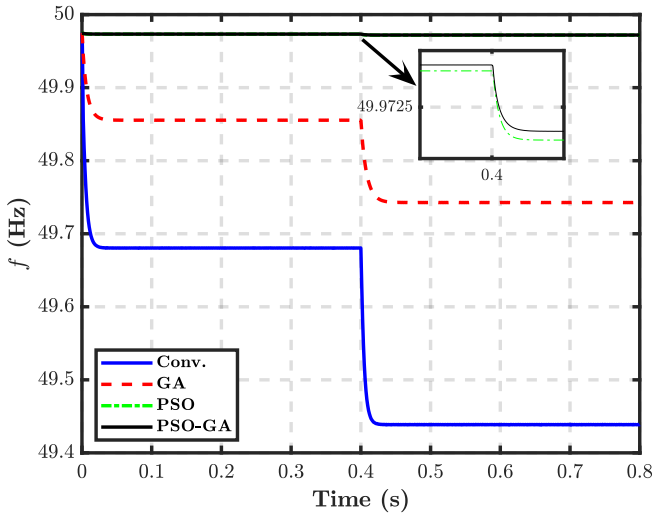

Figure 3.14: Islanded MG response under linear load changes showing the evolution of frequency.

The d-axis output voltage and q-axis output voltage are shown in Figure 3.16. From these figures, it can be concluded that the steady-state values of dq-axis output voltages for controllers designed with PSO-GA are 379.61 and 0.0004 V which approximately match the desired reference values 380 and 0 V. Table 3.5 shows the transient performance of the PI controllers in terms of settling time t_s and rising time t_r. The settling times of the d-axis PI current controller are 0.0084, 0.013, 0.0039, and 0.0029 s for conventional, GA, PSO, and the proposed PSO-GA respectively. It is obvious in this table that the transient performance of the controllers designed with the proposed PSO-GA is the most appropriate one. The dynamic response of MG active and reactive power are illustrated in Figure 3.17.

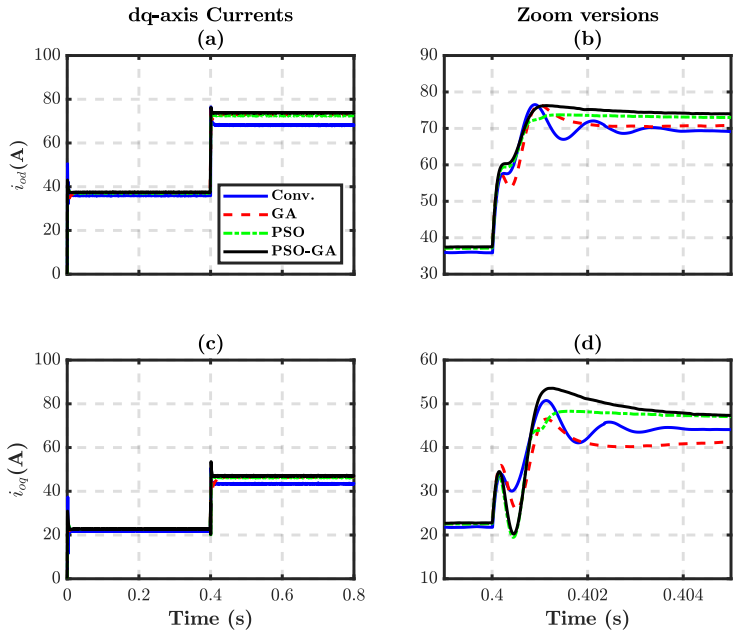

Figure 3.15: The dq-axis inverter output current with different designed parameters: (**a**) d-axis current; (**b**) d-axis current zoom version; (**c**) q-axis current; (**d**) q-axis current zoom version.

The capability of providing active and reactive power is improved by the controllers designed with PSO-GA. This is because the final values of dq-axis output currents are 73.85 and 47.08 A, while in the conventional method, they are 68.17 and 43.41 A.

The three-phase output voltage of the islanded MG under linear load changes with different designed controllers is shown in Figure 3.18. It can be seen that all voltages are sinusoidal but the dynamic response and steady-state values obtained from controllers designed with PSO-GA show superiority over other designed controllers. The steady-state values of three-phase voltage magnitudes are 351.44, 375.65, 372.7, and 380.28 V in conventional, GA, PSO, and PSO-GA methods respectively.

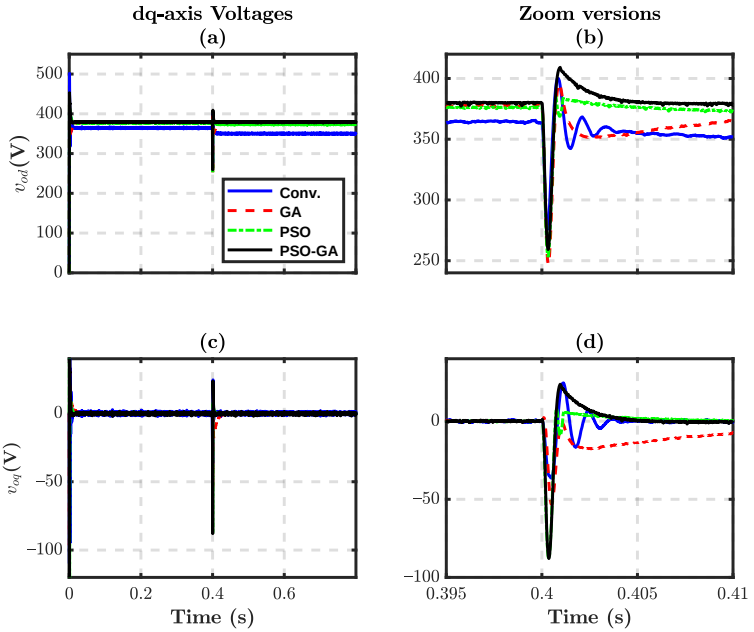

Figure 3.16: The dq-axis inverter output voltage with different designed parameters: (**a**) d-axis voltage; (**b**) d-axis voltage zoom version; (**c**) q-axis voltage; (**d**) q-axis voltage zoom version.

Table 3.5: The comparison of the PI controllers transient performance.

Parameters	Conv.	GA	PSO	PSO-GA
i_{od} control t_s (s)	0.0084	0.013	0.0039	0.0029
i_{od} control t_r (s)	0.0017	0.0008	0.00091	0.0008
i_{oq} control t_s (s)	0.0076	0.0259	0.0077	0.0044
i_{oq} control t_r (s)	0.00082	0.0011	0.0011	0.00087
v_{od} control t_s (s)	0.0074	0.019	0.0058	0.0038
v_{od} control t_r (s)	0.0017	0.00073	0.0007	0.00069
v_{oq} control t_s (s)	0.0128	0.033	0.0106	0.0051
v_{oq} control t_r (s)	0.00082	0.00016	0.00073	0.00072

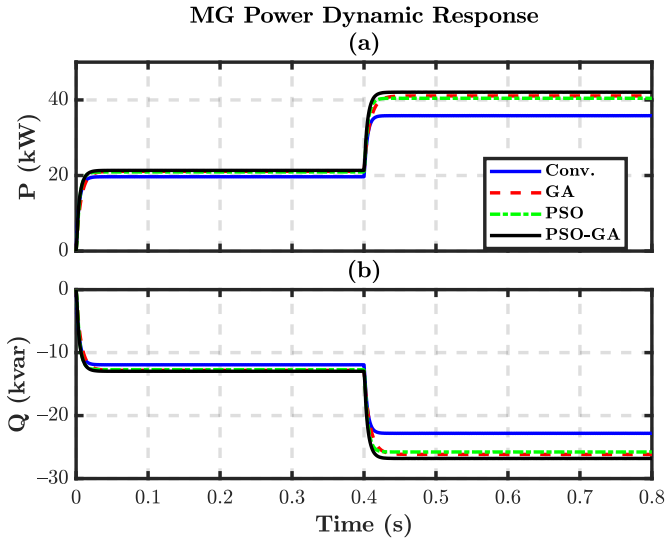

Figure 3.17: Active and reactive power of the MG under linear load changes for different designed parameters: (**a**) active power; (**b**) reactive power.

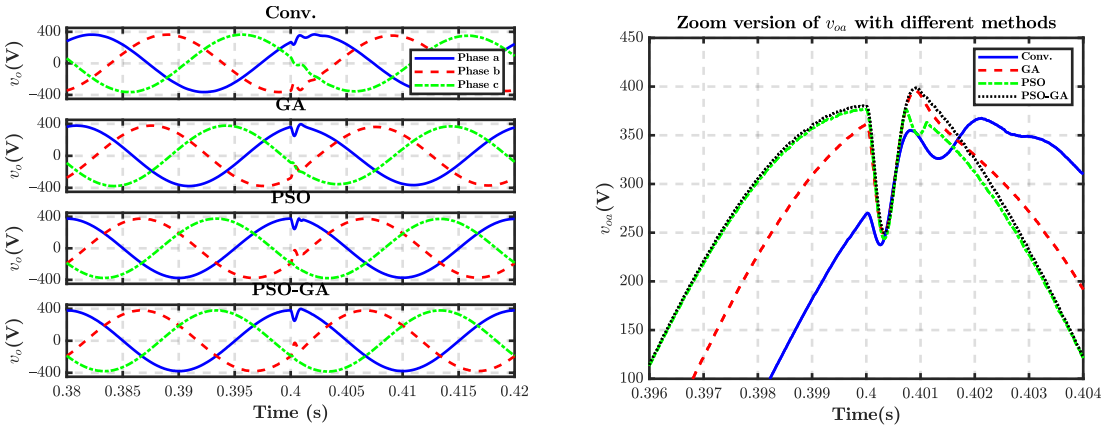

(**a**) Three-phase voltages.

(**b**) Zoom version of phase a voltage.

Figure 3.18: Three-phase voltages and phase a voltage of the MG common bus with different designed parameters.

3.5.2 Case Study II: One Inverter with Nonlinear Load

The second case study investigated in this chapter is shown in Figure 3.19. A nonlinear load is connected to the islanded MG and a step load change is applied at $t = 0.4$ s. Figure 3.20 shows the nonlinear load three-phase currents. Figure 3.21 shows the time evolution of the frequency of the islanded MG under the nonlinear load changes with four control approaches: controllers with Ziegler–Nichols classically designed parameters, controllers with optimized tuned parameters through GA, controllers with optimized tuned parameters through PSO, and controllers with optimized tuned parameters through proposed PSO-GA. It can be seen that the steady-state frequency error with optimized controllers decreases in comparison with controllers with classically designed parameters. The proposed PSO-GA has a more acceptable steady-state frequency among others and it is 49.972 Hz. For example, in the first method, the frequency deviation from nominal frequency 50 Hz is 0.56 Hz while in the proposed PSO-GA, the frequency deviation is less than 0.03 Hz. The dynamic performance of the dq-axis currents is shown in Figure 3.22

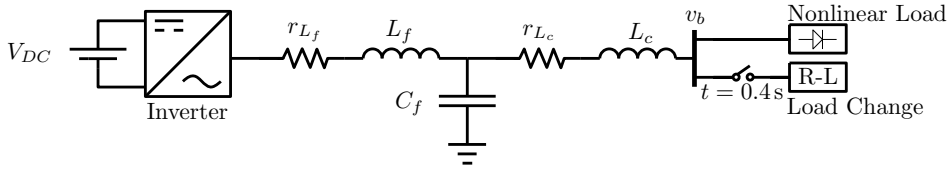

Figure 3.19: The second case study.

from which it can be observed that the dq current magnitudes steady-state errors with the proposed PSO-GA control parameters are less than the other controllers. Furthermore, from this Figure, it can also be seen that no matter of 100% increase in the magnitude of dq currents, the control system has a proper and smooth transient response under nonlinear load changes. There is only an oscillation in the dq-axis voltages and currents which

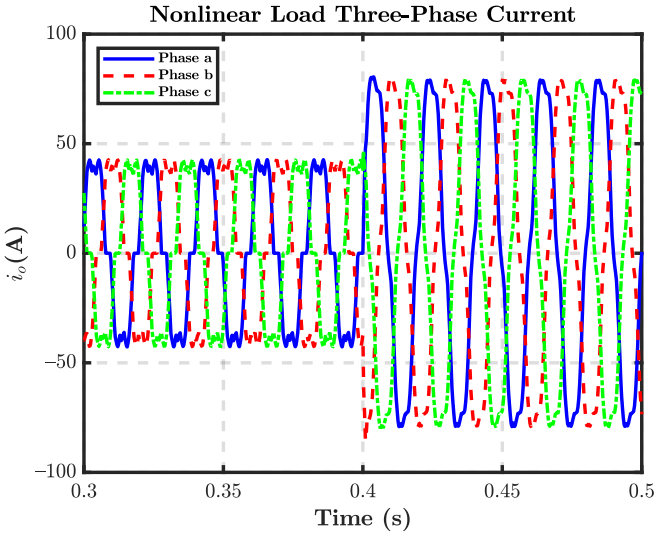

Figure 3.20: Nonlinear load three-phase current.

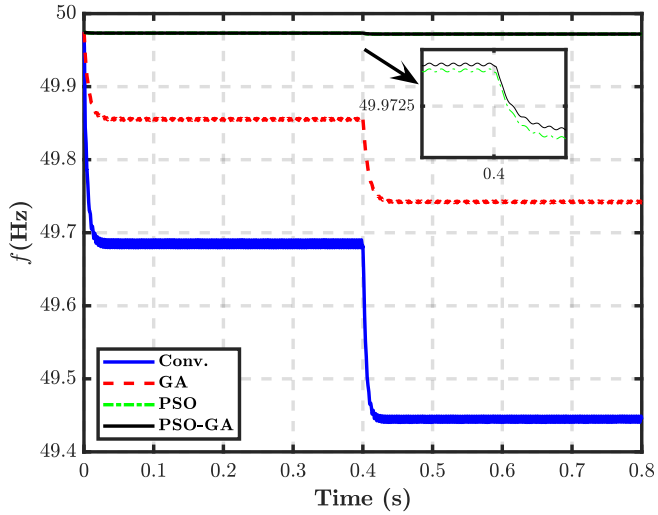

Figure 3.21: Evolution of the frequency of the islanded MG under nonlinear load changes.

comes from the nonlinearity of the load. The dynamic performance of the dq-axis voltages is illustrated in Figure 3.23.

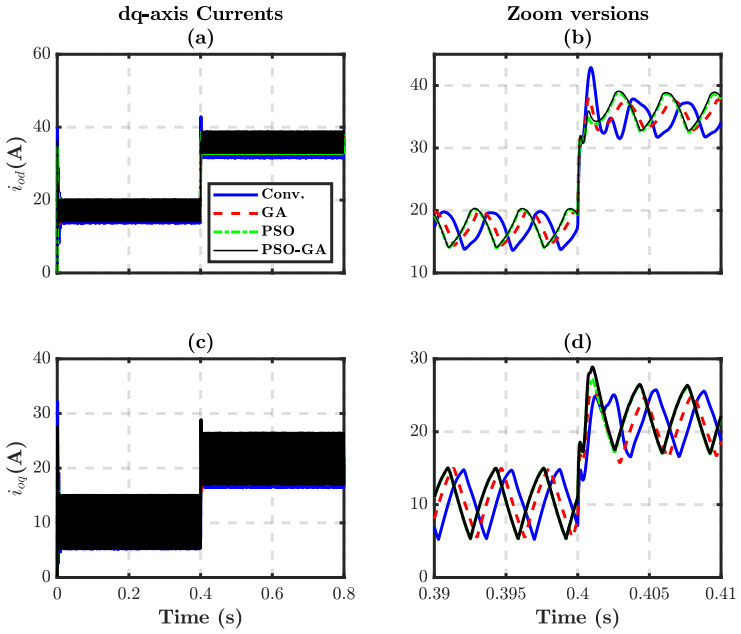

Figure 3.22: The dq-axis output current with different designed parameters under nonlinear load changes: (**a**) d-axis current; (**b**) d-axis current zoom version; (**c**) q-axis current; (**d**) q-axis current zoom version.

The same as with current controllers, it can be observed that the steady-state errors of dq-axis voltage magnitudes with the proposed PSO-GA control parameters are 0.62 V and 0.001 V which are hugely less than the conventionally designed controllers 25.37 V and 0.082 V. The dynamic response of MG active and reactive power are illustrated in Figure 3.24. The capability of providing active and reactive power is improved by the controllers designed with PSO-GA. Figure 3.25 shows the three-phase output voltage under nonlinear load changes. At $t = 0.4$ s, load step change is applied. Note that the voltages have appropriate transient responses and pure sinusoidal waveforms under nonlinear load changes. The steady-state values of three-phase voltage magnitudes under

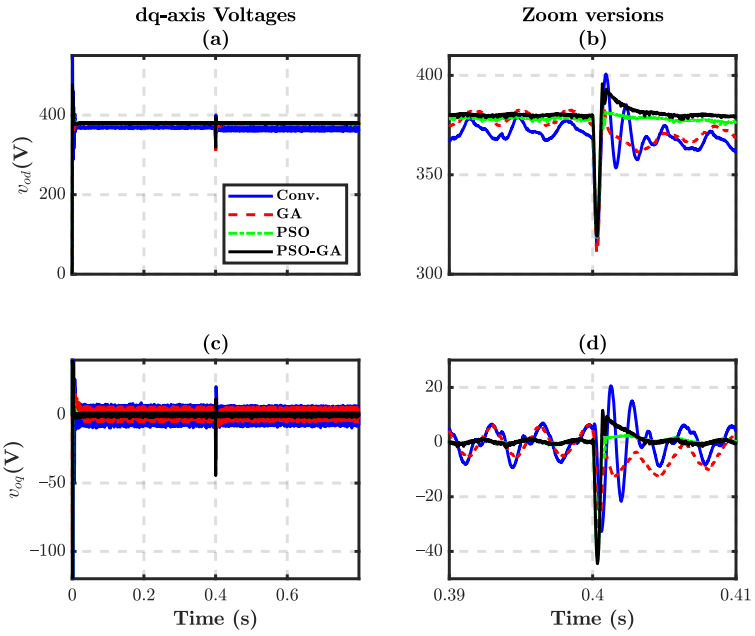

Figure 3.23: The dq-axis output voltage with different designed parameters under nonlinear load changes: (**a**) d-axis voltage; (**b**) d-axis voltage zoom version; (**c**) q-axis voltage; (**d**) q-axis voltage zoom version.

controllers tuned with conventional, GA, PSO, and PSO-GA are 354.63, 369.22, 371.75, and 379.38 V respectively. Therefore, the MG bus steady-state voltages under controllers tuned with PSO-GA are closer to 1 pu and there is no decrease in the magnitude of three-phase voltages after nonlinear load changes take place.

3.5.3 Case Study III: Two Inverter with Linear Load

In order to investigate the performance of the designed controllers in high-order systems, a two-inverter MG is considered. Figure 3.26 shows another considered case study in which two inverters feed a linear load. A 100% load step change is applied to the islanded MG with two inverters at $t = 0.4$ s. Figure 3.27 shows the dq-axis output currents and

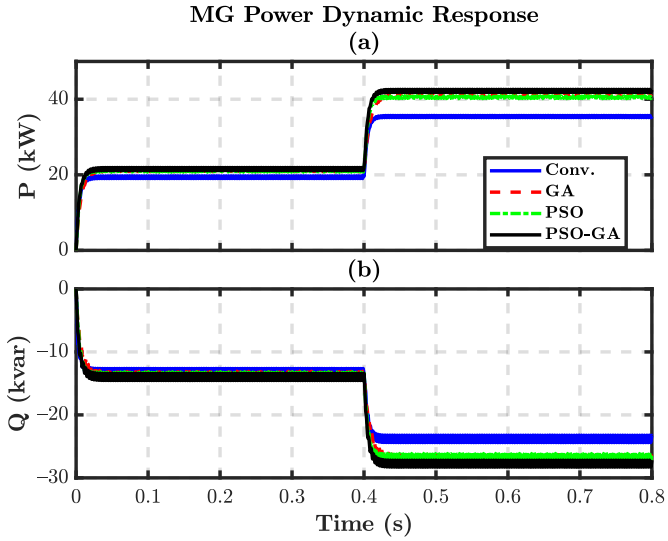

Figure 3.24: MG active and reactive power under nonlinear load changes: (**a**) active power; (**b**) reactive power.

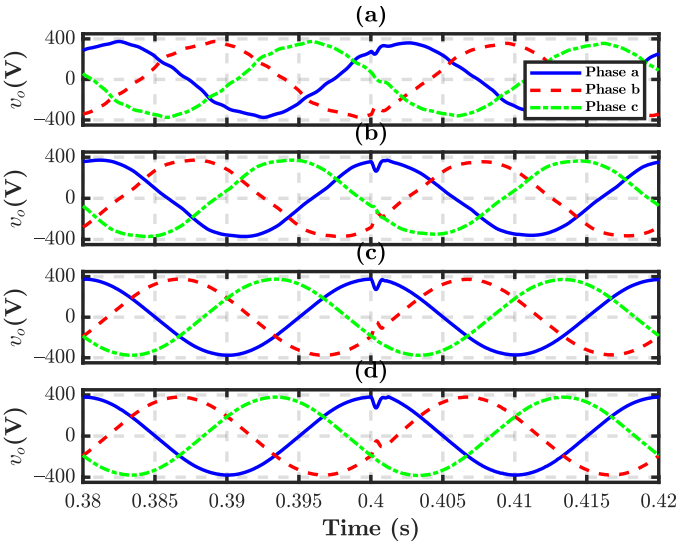

Figure 3.25: MG three-phase voltages under nonlinear load changes with different designed parameters: (**a**) conv.; (**b**) GA; (**c**) PSO; (**d**) PSO-GA.

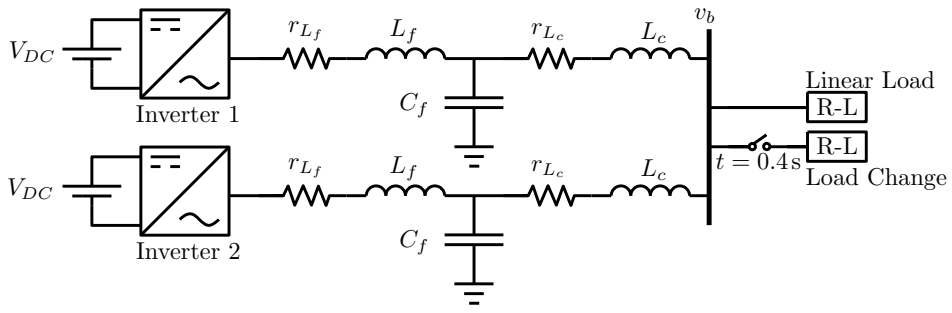

Figure 3.26: The third case study.

dq-axis output voltages for each inverter with classically designed controllers, controllers tuned with GA, PSO, and PSO-GA. It can be clearly observed that the two inverters with classically designed controllers are unstable after load step change. It should be noted that the system would only be stable with the considered transmission line impedance. For example, in the compact MGs in which the inductive value of the transmission line is so small, the system designed in [67] with conventional controllers would be unstable. However, all the systems with optimized designed controllers are stable after loading step change at $t = 0.4$ s. It can be seen in these figures that the d-axis inverter output voltage with controllers designed by proposed GA, PSO, and PSO-GA are 377.6, 376.18, and 379.8 V respectively. Therefore, the dq-axis voltage controllers' steady-state values from the proposed PSO-GA are closer to the desired reference values.

The frequency, the active, and the reactive power of the two-inverter MG controlled by conventionally tuned, GA-tuned, PSO-tuned, and PSO-GA-tuned controllers are shown in Figure 3.28. It can be seen that the system with conventional controllers is unstable. Since each inverter has the same characteristics and the same output filter, the load power-sharing between them is the same as illustrated in Figure 3.28B(b), Figure 3.28C(b), and Figure 3.28D(b) for the GA, PSO, and the PSO-GA-tuned controllers respectively.

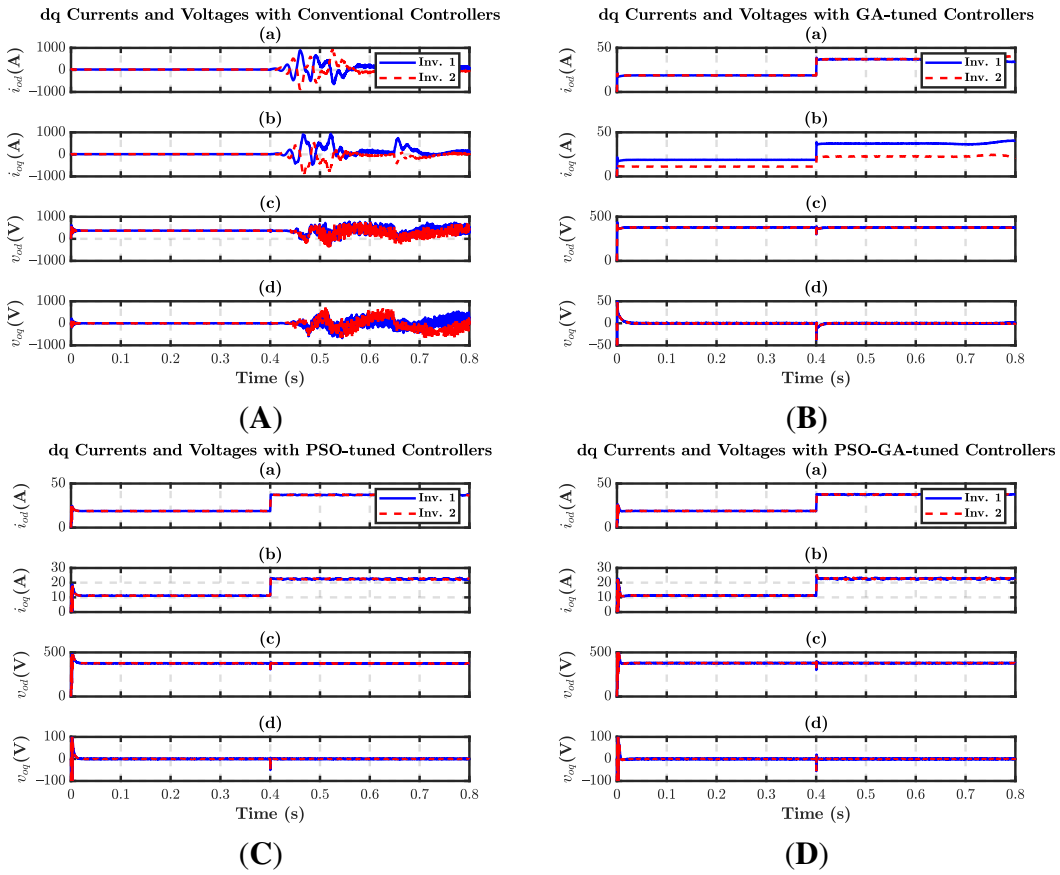

Figure 3.27: The dq-axis output currents and voltages in two-inverter MG: (**A**) conv.; (**B**) GA; (**C**) PSO; (**D**) PSO-GA. (**a**) d-axis current; (**b**) q-axis current; (**c**) d-axis voltage; (**d**) q-axis voltage.

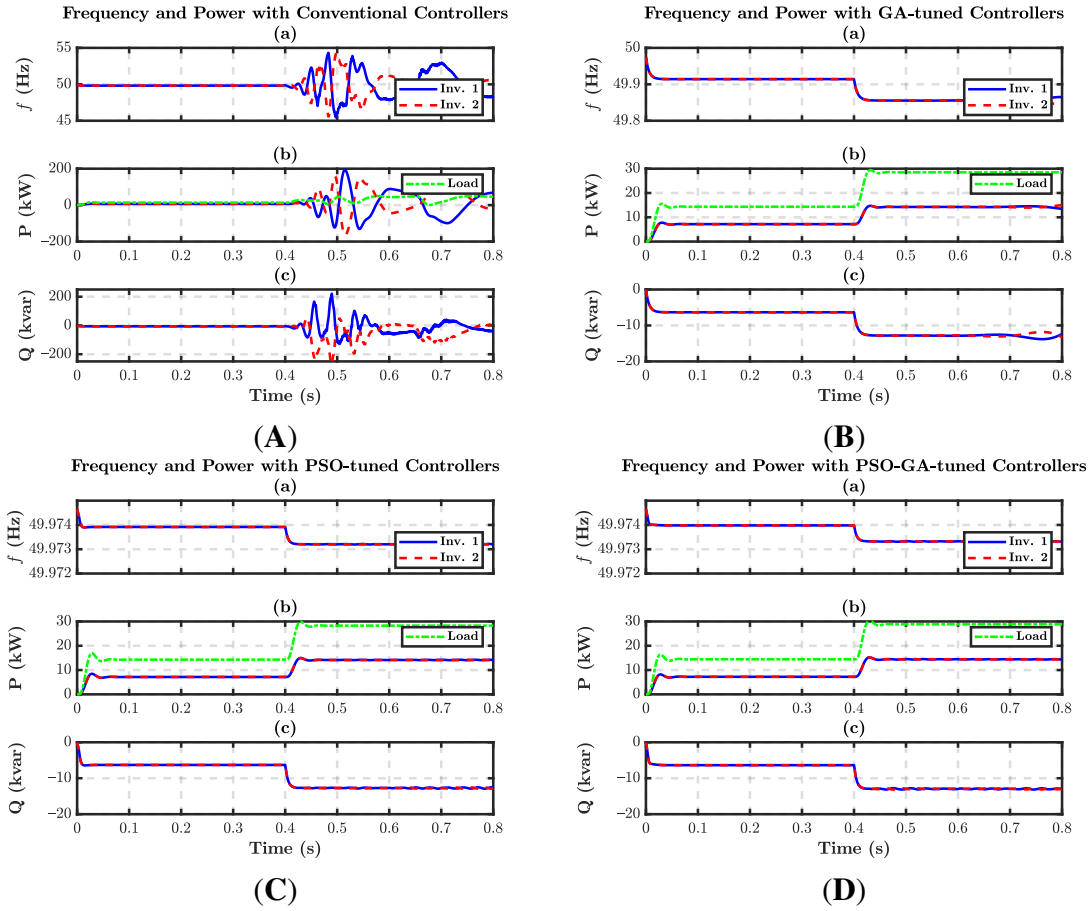

Figure 3.28: The frequency, the active, and the reactive power in two-inverter MG: (**A**) conv.; (**B**) GA; (**C**) PSO; (**D**) PSO-GA. (**a**) frequency; (**b**) active power; (**c**) reactive power.

Three-phase output voltages of two-inverters MG with different designed controllers are shown in Figure 3.29. Figure 3.29a is the three-phase output voltage of the first inverter and Figure 3.29b is the three-phase output voltage of the second inverter with classically designed controllers. As can be observed in this figure, the three-phase output voltages are unstable for both inverters. Three-phase output voltages of inverters controlled by optimized controllers are pure sinusoidal and balanced. Figure 3.29c,d shows the three-phase output voltages of two inverters in which GA is used to design their controllers, while Figure 3.29e,f are the three-phase output voltages of two inverters in which PSO is used. The three-phase output voltages of two-inverter MG controlled by the proposed PSO-GA-designed controllers are shown in Figure 3.29g,h.

After investigating all the case studies above, it can be concluded that the proposed design approach is universal for any MG size and configuration no matter of line impedances and loads types. This helps designers to minimize their efforts to tune the controllers if the output impedance or the number of inverters changes. In addition, from all the presented figures, it can be inferred that the controllers tuned with the proposed PSO-GA have better performance than others in different case studies such as linear load step changes, nonlinear load step changes, and linear load step changes in an MG with two inverters. Table 3.6 shows the comparative analysis of the designed controllers in different case studies. As it can be seen from this table, the steady-state values of the frequency, the three-phase output voltage magnitude, the dq-axis currents, the dq-axis voltages, and the frequency and voltage magnitude deviation from their nominal values are better with the proposed PSO-GA algorithm.

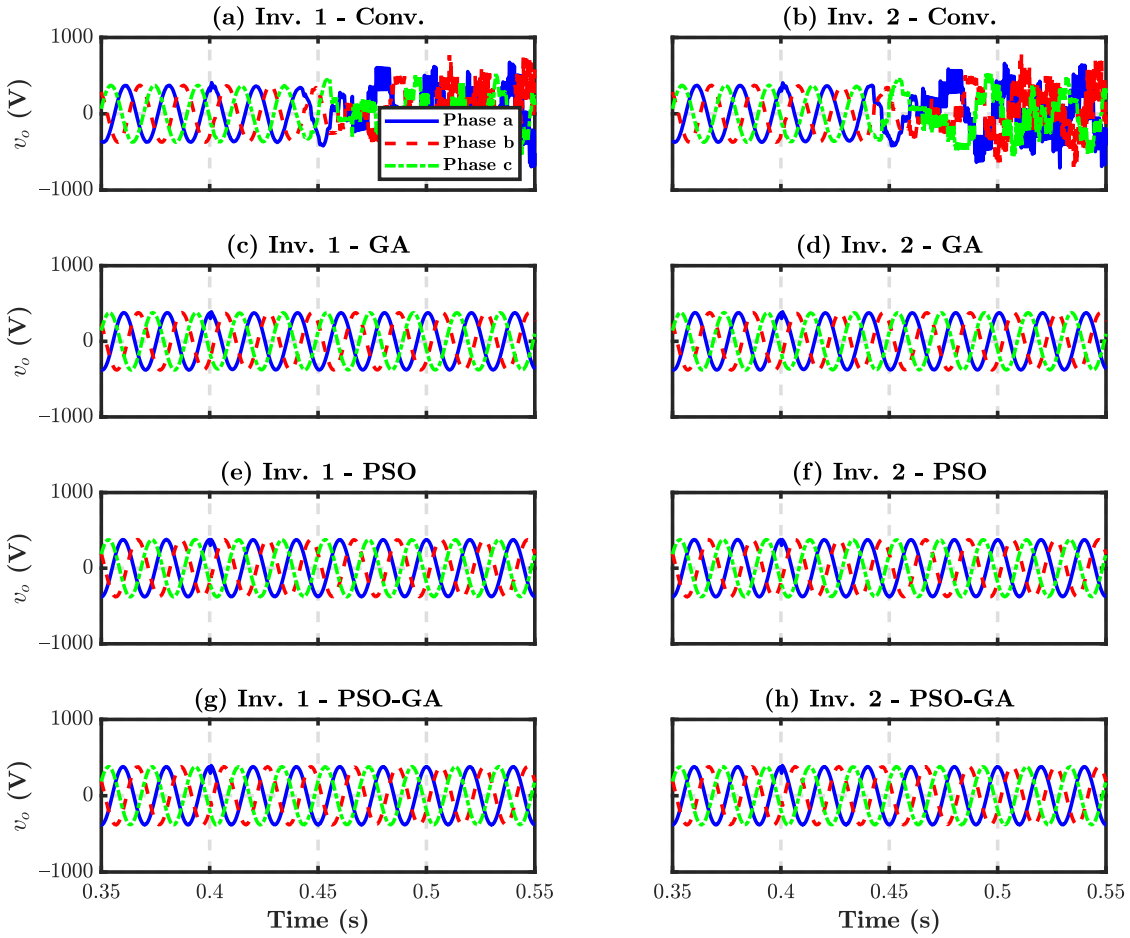

Figure 3.29: The inverters three-phase output voltages with different designed parameters in two-inverter MG: (**a**) inv. 1 with conv.; (**b**) inv. 2 with conv.; (**c**) inv. 1 with GA; (**d**) inv. 2 with GA; (**e**) inv. 1 with PSO; (**f**) inv. 2 with PSO; (**g**) inv. 1 with PSO-GA; (**h**) inv. 2 with PSO-GA.

Table 3.6: The comparative analysis of designed controllers' steady-state values in different case studies.

Variables	Case Study I				Case Study II				Case Study III [1]			
	Conv.	**GA**	**PSO**	**PSO-GA**	**Conv.**	**GA**	**PSO**	**PSO-GA**	**Conv.**	**GA**	**PSO**	**PSO-GA**
f	49.46	49.76	49.971	49.972	49.44	49.74	49.971	49.972	Unstable	49.85	49.97	49.97
$f_n - f$	0.54	0.24	0.029	0.028	0.56	0.26	0.029	0.028	Unstable	0.15	40.03	0.03
V_o	351.44	375.65	372.7	380.28	354.63	369.22	371.75	379.38	Unstable	377.37	376.70	380.32
$V_n - V_o$	28.56	4.35	7.3	-0.28	25.37	10.78	8.25	0.62	Unstable	2.63	3.3	-0.32
I_{od}	68.17	72.98	72.41	73.85	67.66	73.33	72.69	74.17	Unstable	37.26	37.12	37.48
I_{oq}	43.41	46.50	46.16	47.08	45.28	47.73	47.70	48.69	Unstable	22.66	22.54	22.75
V_{od}	350.33	375.03	372.26	379.61	348.94	374.96	372	379.6	Unstable	377.60	376.18	379.81
V_{oq}	0.0076	0.0011	0.0004	0.0004	0.082	0.037	-0.0018	-0.001	Unstable	0.008	0.00008	0.0003

[1] The values of two inverters are the same.

3.6 Conclusions

In this chapter, a new design approach is presented for the optimized selection of controllers' parameters in an islanded MG. The state-space model of a VSI involving power, voltage, and current controllers are used for the formulation of the optimization problem. The impact of operating point and output impedance changes in the eigenvalues of the inverter small-signal state-space matrix are investigated. Then, the optimization problem is solved through different optimization algorithms, including the PSO, the GA, and the proposed PSO-GA for the worst-case scenario of the operating point. This can guarantee the stability of the system in the whole range of operations. As a result, the power, voltage, and current control coefficients are determined. The performance of the control system with tuned parameters through PSO, GA, and PSO-GA has been compared with classically-designed controller parameters under linear and nonlinear load changes with one and two parallel-connected inverters. The system is unstable in the islanded MG with two parallel-connected inverters without significant line impedance under classically-designed controllers parameters while it is stable with tuned parameters through PSO, GA, and PSO-GA. The simulation results showed that the performance of the control system with the proposed PSO-GA-tuned controller's parameters is much better than the classically-designed controller's parameters. By virtue of this method, the bus frequency

and voltage of the islanded MG are in the allowable and appropriate range. The effectiveness of the presented method was verified by simulation results from PSIM© software. The main advantages of the proposed method are summarized below.

- Proposing a simple guideline for engineers to design controllers' parameters in an islanded MG regardless of the number of inverters, MG configuration, output impedances, and loads types which significantly reduces the effort and complexity of the design issue.
- Improvement in the steady-state frequency, the dq currents, and the three-phase voltages response under linear load changes, nonlinear load changes, and linear load changes in the islanded MG with two grid-forming inverters.
- Needless of coefficient readjustment for the whole range of operating points.
- Providing a plug-and-play design approach when a new DG wants to be added to the MG.

Chapter 4

Ultra-fast Charging Station

4.1 Abstract

The emergence of DC fast chargers for electric vehicle batteries (EVBs) has prompted the design of ad-hoc MGs, in which the use of a SST instead of a low-frequency service transformer can increase the efficiency and reduce the volume and weight of the MG electrical architecture. Mimicking a conventional gasoline station in terms of service duration and service simultaneity to several customers has led to the notion of ultra-fast chargers, in which the charging time is less than 10 minutes and the MG power is higher than 350 kW. This survey reviews the state-of-the-art of DC ultra-fast charging stations, SST transformers, and DC ultra-fast charging stations based on SST. Ultra-fast charging definition and its requirements are analyzed, and SST characteristics and applications together with the configuration of power electronic converters in SST-based ultra-fast charging stations are described. A new classification of topologies for DC SST-based ultra-fast charging stations is proposed considering input power, delta/wye connections, number of output ports,

and power electronic converters. More than 250 published papers from the recent literature have been reviewed to identify the common understandings, practical implementation challenges, and research opportunities in the application of DC ultra-fast charging in EVs. In particular, the works published over the last three years about SST-based DC ultra-fast charging have been reviewed.

4.2 Introduction

The technical requirements of battery fast charging cannot be fulfilled by the EV onboard charger, which is connected to a single-phase or three-phase AC domestic supply [18]. To decrease the charging time, a huge amount of DC power is required [95], so it is mandatory to supply the charging station MG from a medium voltage (MV) AC source. This connection could be carried out through a LFT, a HT, or a SST [96]. It is worth mentioning that the notion of SST is used here in a broad sense, which means that it can be considered as such any conversion structure implemented with switching converters that is capable to transform MV-AC into DC in the region between 200 V and 500 V.

This chapter is motivated by the identification of the state of the art of ultra-fast charging stations, which can be based either on LFT or SST as illustrated in Figure 4.1(a) and Figure 4.1(b) respectively. It is apparent in that figure that the DC SST-based ultra-fast charging station allows the integration of renewable energies, energy storage, and AC/DC loads, so the resulting electrical architecture can be considered as an AC/DC/Hybrid MG. In a clear-cut contrast, a LFT-based ultra-fast charging station does not facilitate the integration of renewable energies but it offers the advantage of high reliability at the expense of a relatively big size (Table 4.1).

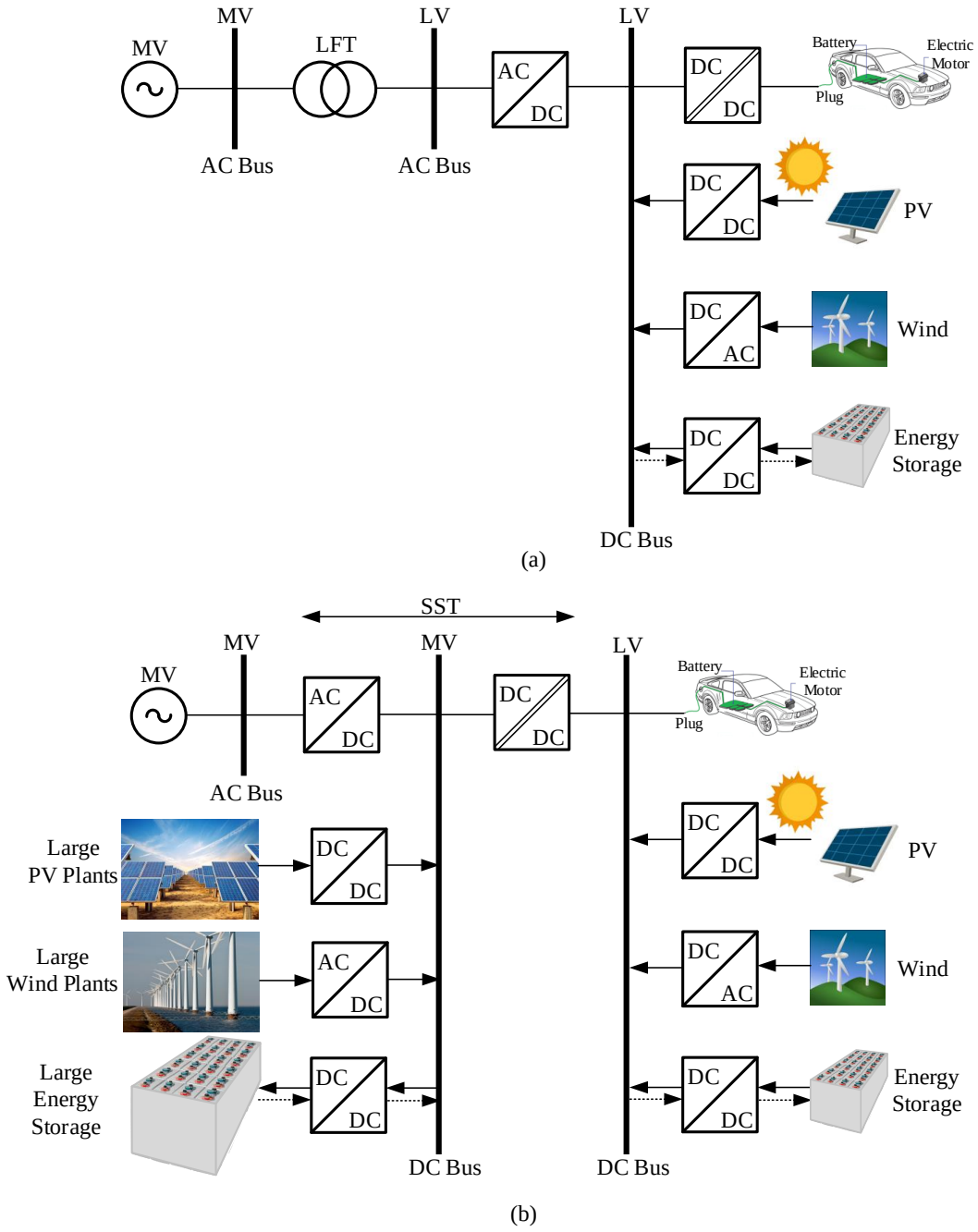

Figure 4.1: The ultra-fast charging stations: (**a**) DC LFT-based ultra-fast charging station; (**b**) DC SST-based ultra-fast charging station.

Table 4.1: A comparative analysis of DC LFT-based and SST-based ultra-fast charging stations.

Ultra-fast charging station	Size	Controllability	Integration of large power plants	Fault protection	Modularity	Reliability
LFT-based	Big	Limited	No	No	No	High
SST-based	Small	Unlimited	Yes	Yes	Yes	Medium

4.2.1 State of the Art

Carbon dioxide emissions have directly impact on climate changing and global warming. Nowadays, the significant portion of carbon dioxide emissions is issued by fossil fuel vehicles (FFV) [17]. According to statistics, the portion of transportation in carbon production is more than 20% [97]. Therefore, FFVs are being replaced by EVs. The EVs have higher efficiency and less maintenance in comparison with FFVs [98] which can be refueled within two minutes. The EVs charging time is much longer since they are normally charged in the residential distribution network with AC on-board chargers (OBCs) (120 V-240 V)[18]. The provided power through this slow OBCs are within [1.44-22] kW [99]. Therefore, for a 100 kWh battery, it takes more than 5 hours to be fully charged, which is not satisfiable for long trips and it increases the anxiety of the drivers. Advancement of OBCs is still continuing but there are some barriers in high-power AC OBC such as charger size, cost, weight, maintenance, and EV safety requirements [100]. The next solution is to utilize integrated charging structure by means of a traction motor which was previously used in railway traction industry [101]. Three-phase electrical motor winding can get the high power and charge the battery through the inverse operation of the drive inverter [102]. However, this technique has some adverse effects on EV such as high stress on the traction system, torque production, acoustic noise, and mechanical vibrations which reduce the lifespan of the whole EV [103]. Another alternative solution is to build a DC

ultra-fast charging station like traditional fuel stations to directly communicate and charge the EV battery [95]. In a DC ultra-fast charging station, the charging time of EVs should significantly decrease to be competitive with traditional fuel stations. In order to decrease EV's charging time, the amount of the delivered power to the EV's battery charger should increase. Until now the maximum DC power delivered to the EV battery in the market is 250 kW. The limit is due to the high temperature [104] and state of health (SOH) issues of the battery [105]. However, it is forseen to reach 1200 kW maximum delivered DC power [106] as an aftermath of advancement in battery structure design, vehicle electrical architecture and material in the near future [107].

In order to build a DC ultra-fast charging station, this should be fed by MV transmission lines. In order to decrease the voltage level to the one required for the EV's battery chargers, LFT, HT [19], and SST [108] can be used in the charging stations. The first one suffers from low efficiency, bulky size, high maintenance cost, slow dynamics, limited controllability, and lacking of plug-and-play functionality [10]. These shortcomings make LFT less functional in DC ultra-fast charging stations. The HT is the combination of partially-rated power converters, normally between 5%-20% of the rated power, in the input or output of a LFT. The HT also suffers from bulky size but it is more efficient and controllable than LFT. A 2 kVA small-scale HT is experimentally validated in [109]. The last promising solution to change the MV level into the EV battery charger voltage level is to utilize a SST. It has higher degree of control freedom, storage integration capability, harmonic filtering, smaller size, fault current limitation, bidirectional power flow capability, and higher operational frequency [20]. In addition, advancement of high-voltage high-power SiC and GaN devices has paved the way for the extensive use of SSTs in the high-power applications [21]. The performances of SST, HT with integrated energy storage, and LFT have been technically and economically compared in [96] for distribution

grid applications. Since the use of SST in power systems is still new, there exist many issues and challenges specially in the DC ultra-fast charging applications which should be addressed.

4.2.2 Objectives of the Chapter

The aim of this chapter is to provide a step-by-step comprehensive review about DC ultra-fast charging stations where SST is used. This chapter provides information about ultra-fast charging definition and requirement, SST definition, structure, and challenges, as well as DC SST-based ultra-fast charging station configuration, control and challenges. A new topology configuration for DC SST-based ultra-fast charging station is classified based on the input type, number of the output ports, and the converter type. The DC SST-based ultra-fast charging station is considered as a MG and possible challenges of MGs are discussed.

4.2.3 Organization of the Chapter

The rest of this chapter is organized as follows. In section 4.3, a complete description of the battery charging is surveyed. Section 4.4 describes the state of the art of DC ultra-fast charging stations. In section 4.5, a comprehensive review of SST topologies is presented. Section 4.6 investigates all the technical and research works performed in DC SST-based ultra-fast charging stations. Finally, section 4.7 concludes the chapter.

4.3 Battery Charging Definition and Barriers

The battery charging procedure has different definitions and requirements. One of the most important definitions is the battery C rating. The battery capacity is usually rated at 1C (1C current) [110]. As an example, a 400 V battery with 100 kWh capacity can be charged or discharged with 250 A within one hour. It means that by the use of 1 kA current, the battery can be recharged in 1/4 h. Therefore, increase in C rating yields faster charging or discharging time. However, C rate increase has technically some limitations, including increase in internal energy losses, battery thermal tolerance, and reducing battery's life-cycle [111]. The 6C rate of charging is considered as an ultra-fast charging according to the US Department of Energy (DOE) [112]. As a result, a trade-off exists between ultra-fast charging and battery health [113].

The battery discharging procedure is related to the demanded power and it is not controllable. However, the battery charging task can be controlled with optimal charging strategies. Monitoring and estimating of the state of charge (SOC) and the state of health (SOH) play a significant role in battery charging methods [114], [115]. Different charging strategies have been proposed in the literature for the Lithium-ion (Li-ion) batteries [116], [117]. Some of them are independent from the battery chemical model and dynamic, e.g. constant-current (CC) [118], constant-current constant-voltage (CCCV) [119], multi-stage CCCV [120], and pulse charging techniques [121]. The typical CCCV charging method is illustrated in Figure 4.2 [122]. Some others are based on empirical models [123], including circuit-based models [124] and neural network models [125]. The pseudo-two-dimensional (P2D) [126] and single particle model (SPM) [127], [128] are the most usable circuit-based models for the battery charging optimization, battery SOC

prediction [129], and control. The last charging approach is based on battery electrochemical model in which all the physical parameters are observed. This approach is the most complicated and accurate one among others. However, due to the high computational burden, its real-time charging controller implementation is not practical yet.

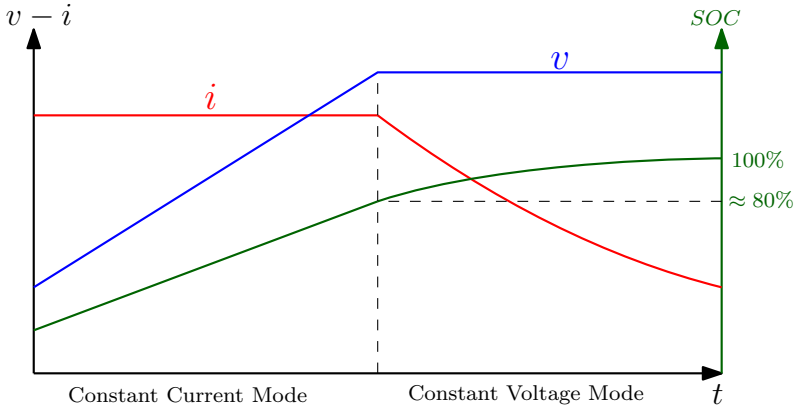

Figure 4.2: The typical CCCV charging method.

To summarize, the optimal charging strategies should be fast as far as possible while the temperature limitation and battery SOH are maintained within the desirable range [130]. In EVs application, the responsible part for the optimal operation of battery charging is battery management system (BMS) which analyses and monitors all the information taken from the EV battery pack [131]. The BMS cooperates with battery charging circuit through the exchange of data in order to control the injected current and voltage to the battery cells [132]. Battery charging circuits can be placed on-board inside EVs [133], off-board in the charging stations, wireless (inductive) with unidirectional or bidirectional power flow [134]. The OBCs connect to the residential single-phase or three-phase AC voltage and the off-board chargers connect to the DC voltages with different kinds of cables, some of them are illustrated in Figure 4.3. The connectors are categorized to four

levels according to their maximum power transfer capability. The level 1 and level 2 AC chargers are supplied with 120 V and 240 V AC respectively [99]. In the market, their maximum supplied power for the battery is 1.92 kW in level 1 and 19.2 kW in level 2. International Electrotechnical Commission (IEC) has published standard requirements for EV's plugs, socket-outlets, connectors and inlets (IEC 62196) [135]. According to the IEC 62196-2:2016 [136], the maximum power for the level 2 on-board charging mode is 33.6 kW (480 V AC, 70 A). In the pre-release version of IEC 62196-1:2022 PRV [137], the AC charger maximum power was determined as 172.5 kW (690 V AC, 250 A) and the DC ultra-fast charging maximum power was 1200 kW (1500 V DC, 800 A). Table 4.2 shows some of the charging connectors' voltage and power ratings existing in the market categorized by their charging speed. It should be noted that due to the weight and size limitation in EVs, utilization of OBCs is limited to the low-voltage low-power applications [138]. Therefore, they can not be charged as fast as enough to mimic the same refueling experience in conventional gasoline stations. Commercial on-board charging including dedicated and integrated as well as off-board charging infrastructures are surveyed in [139]. Different charging topologies such as bidirectional active front end (AFE) [140], interleaved unidirectional charger topology [141], and bridgeless power factor correction (PFC) stages [142] are reported in detail in [143].

To increase the distance traveled by the EVs, the first solution is to raise the EV's battery capacity which yields bigger EV size, cost and weight [144]. Different types of batteries have been used in EVs such as Lead-acid (Pb-acid), Nickel-Cadmium (NiCd), Nickel-Metal-Hydrid (NiMH), Li-ion, Li-ion Polymer, and Sodium Nickel Chloride (NaNiCl) [145]. Among them, Li-ion batteries have been extensively commercialized in the EV industry thanks to their higher energy density, longer life cycle, and lower maintenance [146]. The EV's battery characteristics for some of vehicle manufacturers are shown in

Table 4.2: Characteristics of battery charging connectors.

Model	Charging level	Voltage	Maximum power	100 kWh Battery charging time	Charger location	Maximum current
SAE J1772	Level 1 (Slow)	120 V_{AC} (1ϕ)	1.44-1.92 kW	52-69 h	on-board	12-16 A
	Level 2 (Slow)	208-240 V_{AC} (1ϕ)	5.0–19.2 kW	5-20 h	on-board	24-80 A
	Level 3 (Fast)	50-1000 V_{DC}	80 kW	75 m	off-board	80 A
	Level 4 (Ultra-fast)	50-1000 V_{DC}	400 kW	15 m	off-board	400 A
Mennekes/EU	Level 1	250 V_{AC} (1ϕ)	4-8 kW	12.5-25 h	on-board	16-32 A
	Level 2	480 V_{AC} (3ϕ)	13.3-22 kW	4.5-7.5 h	on-board	27-45 A
	Level 3	500 V_{DC}	70 kW	85 m	off-board	140 A
	Level 4	500-1000 V_{DC}	200 kW	30 m	off-board	200 A
GB/T	Level 1	250 V_{AC} (1ϕ)	7 kW	14 h	on-board	28 A
	Level 2	400 V_{AC} (3ϕ)	12.8 kW	7.8 h	on-board	32 A
	Level 3	250-950 V_{DC}	60 kW	100 m	off-board	250-400 A
	Level 4	250-950 V_{DC}	237.5 kW	25 m	off-board	250-400 A
Tesla	Level 1	120/240 V_{AC} (1ϕ)	1.9-7.7 kW	13-52 h	on-board	16-32 A
	Level 2	208/250 V_{AC} (1ϕ)	2.8-11.5 kW	9-35 h	on-board	48 A
	Level 3	300–480 V_{DC}	250 kW	24 m	off-board	800 A
	Level 4	300–480 V_{DC}	350 kW	17 m	off-board	800 A

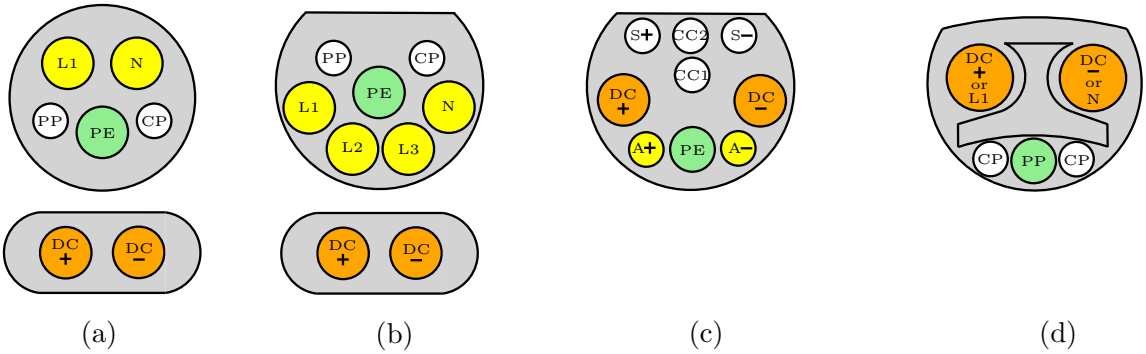

L1	Single-phase AC voltage	S+	Charging Communication CAN 0V-30V 2A
N	Neutral	S−	
CP	Control Pilot	CC1	Charging Connection Confirmation 0V-30V 2A
PP	Proximity Pilot	CC2	
PE	Protective Earth	A+	Low-voltage auxiliary power supply 0V-30V 20A
L1-L2-L3	Three-phase AC voltages	A−	

Figure 4.3: Examples of EV connectors : (**a**) SAE J1772 (Type 1); (**b**) SAE J3068/EU (Type 2); (**c**) BB (GB/T 20234.3); (**d**) Tesla (Ultra-fast charging).

Table 4.3 [147]–[149]. As can be observed from this table, the battery capacity and supercharger maximum power reaches 103 kWh and 250 kW respectively which reduces full-charging time within 30 minutes. From material point of view, fast charging of Li-ion batteries is reviewed in [150]. The research is still ongoing in the material engineering for the advancement of the energy storage systems and improving their energy density. Their charging time should be reduced to the range 5-10 minutes to be competitive with conventional fuel stations. Another solution is to build a DC ultra-fast charging station like traditional gasoline stations [151]. This can give the opportunity to the drivers to frequently charge their vehicles in urban or interurban DC ultra-fast charging stations. From economical point of view, building DC ultra-fast charging stations is more appropriate [100] as will be detailed in the next section.

Table 4.3: Battery characteristics for some of EV manufacturers.

Car model	**Battery type**	**Capacity**	**Voltage**	**Range**	**Fast-charging time**	**Supercharger maximum power**
Tesla Model Y	Li-ion	75 kWh	360 V	487 km	31 min	250 kW
Tesla Model X	Li-ion	100 kWh	350-375 V	536 km	28 min	250 kW
Tesla Model 3	Li-ion	50-75 kWh	350-400 V	507 km	31 min	250 kW
Tesla Model S	Li-ion	103 kWh	400 V	637 km	27 min	250 kW
Volkswagen ID.3	Li-ion	62 kWh	408 V	415 km	38 min	125 kW
Volkswagen ID.4	Li-ion	77 kWh	400 V	514 km	38 min	125 kW
Volkswagen ID.5 GTX	Li-ion	82 kWh	400 V	490 km	33 min	135 kW
Renault Zoe E-Tech	Li-ion	52 kWh	375 V	390 km	78 min	50 kW
Renault Megane	Li-ion	60 kWh	400 V	360 km	54 min	130 kW

4.4 DC Ultra-fast Charging Station

Different possible configurations of DC ultra-fast charging station are AC-coupled, DC-coupled, and hybrid-coupled. These are shown in Figure 4.4. In this figure, all the power flows could be bidirectional to satisfy vehicle-to-grid (V2G), vehicle-to-home (V2H), and vehicle-to-vehicle (V2V) applications in the future smart grids [152]. To deliver the power to or from an EV, bidirectional power electronic converters are used which are comprehensively reported in [153]. An example of AC-coupled DC ultra-fast charging station is in the Mountain View, California, with six superchargers and a 400 kWh integrated energy storage for the load shaving within peak hours. AC-coupled DC ultra-fast charging station has some advantages such as appropriate converter technology, switchgear, protection devices, and well-established standards. The only disadvantages of AC-coupled stations is the huge amount of used power converters in order to integrate with the DC systems which lead to more complex and less efficient systems. In addition, some control challenges appear in the island mode of operation such as reactive power control, inverter synchronization, and voltage/frequency control. The DC-coupled configuration, Figure 4.4b, has less conversion stages, higher efficiency, simpler control structure while complex protection scheme and non-standardized metering [154]. Moreover, the integration of renewable energies and energy storage is more simpler. In addition, the proposed structure of a DC ultra-fast charging station with bipolar DC bus in [155] can solve the grounding issue of DC network [156], [157]. In the hybrid-coupled charging station, Figure 4.4c, which is a combination of DC-fast charger, single-phase and three-phase AC chargers, the system suffers from load nonlinearity problems due to the use of power electronic converters as well as unbalance issues due to the connection to single-phase chargers or different fast charging pilots power requirement.

As was reported previously in Table 4.3, the supercharger maximum power existing in the EV market is 250 kW. Consider this value as the maximum peak charging power; therefore, the maximum peak power required in the 8-slot DC-coupled DC ultra-fast charging station (Figure 4.4b) would be 2 MW whenever all the pilots are simultaneously charging the EVs with the lowest SOC. This is the worst case scenario which could happen in the charging station. It should be considered that due to the differences in the SOC of EV's batteries, the charging power delivered to each battery could be different (see Figure 4.2).

As shown in Figure 4.4, DC ultra-fast charging station has three power stages which are below. The power stages and utilized power electronic converters inside the EVs can be found in [158].

4.4.1 Power Stage 1

The first power stage is the voltage level changes. The huge amount of power required in the DC ultra-fast charging station should directly be provided from the MV distribution line. Since the battery chargers work at less than 1000 V; a transformer is required to step-down the voltage level. Different types of transformers are used in the literature to step-down the voltage level in power systems including, LFT, SST, and HT [159]. These are shown in Figure 4.5 [96].

The LFTs are bulky in size, weighty and suffer from high installation cost. There is no control freedom in the input/output voltage/current of the LFTs. Although with mechanical tap changers, the voltages can be controlled to a limited extent but it is not sufficient in the fast voltage fluctuations of modern power systems in which the penetration of intermittent renewable energies, EVs and DC ultra-fast charging stations is high. An

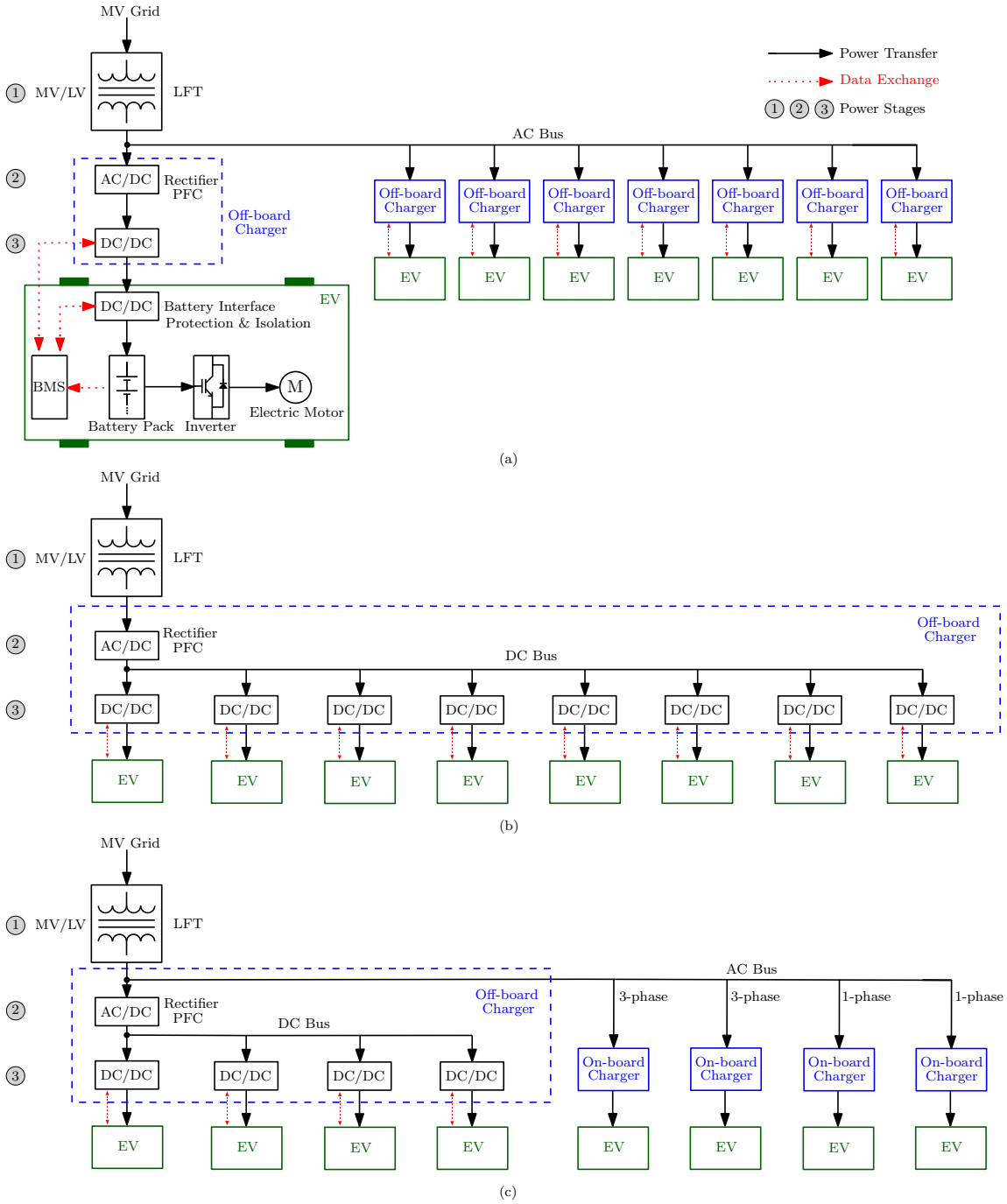

Figure 4.4: The LFT-based ultra-fast charging station configurations: (**a**) AC-coupled; (**b**) DC-coupled; **c**) hybrid-coupled.

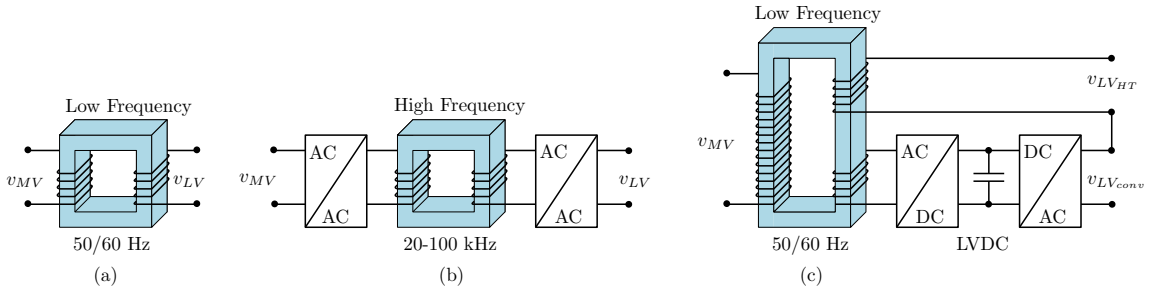

Figure 4.5: Different types of transformers: (**a**) LFT; (**b**) SST; (**c**) HT.

alternative solution is to use HT which is the combination of a power electronic converter in the input/output of the LFTs (Figure 4.4c). Thanks to the power converter installation, integration of energy storage in the HT DC link is possible. The converter power rating is usually between 5%-20% which gives controllability to some extent. However, HT is also bulky and weighty. Another alternative solution is to utilize SST which can provide full control freedom in the input/output voltage/current such as reactive power control, voltage regulation, and harmonic control. Furthermore, the integration of energy storage and renewable energies is hugely simple. The SST has advantages including reduced overall cost and compact size which are explained in detail in the next section. However, due to the switching and conduction losses in SSTs, their efficiency is lower than the LFTs [160]. The research is still open to improve the SST efficiency specifically in high-power applications.

4.4.2 Power Stage 2

The second power stage in the DC ultra-fast charging station is AC to DC conversion which is responsible for the PFC [161]. In this power stage, the converter rectifies the three-phase input AC voltage to a fixed output voltage in the DC link provided that the

power quality is desirable on the grid side. Different kinds of power converters are used for this power stage. The AFE rectifier which is also called as an active pulse width modulated (PWM) rectifier is one of the most used three-phase power converter for this power stage thanks to its high reliability and simplicity. It is used in boost [162], buck [163], and buck–boost [164] mode of operation. Other used simple topologies that can keep the system modularity are half bridge (HB), full bridge (FB), and four-switch buck-boost converter [165] separately used in each phase. Other proposed topologies are multilevel [166] such as cascaded H-bridge (CHB) converter, modular multilevel converter (MMC), three-level boost (TLB) converter, three-level T-type (TLT) rectifier, multi-cell boost (MCB) converter, neutral point clamped (NPC) converter [140], multi-pulse AC–DC converter [167], and Vienna rectifier (VR) [168], [169]. A comprehensive state-of-the-art of AC-DC converters can be found in [170]. The L, LC, and LCL input filters are normally added to the converter input side to desirably satisfy the grid-code requirements as well as to reduce electromagnetic interference (EMI). In both modes of bidirectional AC-DC converter operation, PFC and IEEE-519 grid requirement should be satisfied.

4.4.3 Power Stage 3

The last power stage in the DC ultra-fast charging station is the DC-DC conversion with multi-functional application such as stepping-down the input voltage to the battery voltage level, galvanic isolation to separate the EV from the grid, and cooperation with BMS to satisfy battery optimal charging [171]. Similar to the power stage 2, the used converters in this stage can be unidirectional and bidirectional. From another point of view, they can be galvanically isolated or nonisolated DC-DC converters. On the one hand, the EV's battery is not grounded; therefore, its direct connection with the isolated DC-DC converter

secondary side will isolate it from the grid [154]. As a result, its protection scheme can work separately from the grid. On the other hand, if the isolation is performed by LFT, nonisolated DC-DC converters could be a promising solution which have less complexity to operate in bidirectional power flow mode. Examples of unidirectional isolated DC-DC converters are phase-shifted full-bridge (PSFB) converter [172], interleaved PSFB converter [173], LLC resonant converter [174], and buck–boost three-level semi-dual-bridge [175]. Examples of bidirectional isolated DC-DC converters are dual active bridge (DAB) [176], dual half bridge (DHB) [177], [178], LLC series-resonant converter (LLC-SRC) [179], quad active bridge (QAB) [180], DAB-based active NPC (DAB-ANPC) [181], and CLLC converter [182]. A comprehensive review of isolated DC-DC converters is reported in [183]. Since the battery voltage level is normally lower than the DC link voltage of AC-DC converters, nonisolated DC-DC converters can be categorized as buck converter [184], interleaved buck converter [185], unidirectional TLB converter [186], bidirectional TLB converter [187], and three-level flying capacitor (FC) converter [188], [189].

4.4.4 DC Ultra-fast Charging Station Challenges and Research Gaps

In the vast adaptation of DC ultra-fast charging stations in the power grid, the important challenges are the increase in the daily peak load and shift which may cause transformers and feeders overload, the power system devices aging deterioration, and the increase in power losses [190]. Therefore, investigating the impact of high-power DC ultra-fast charging station load profile in the power grid stability and proposing novel optimal charging strategies for the EV batteries are necessary. Moreover, from the power system operation point of view, the DC ultra-fast charging stations should be a controllable and predictable load. For that, different solutions have been proposed [191]. One is integrating energy

storage and renewable energies illustrated in the schematic shown in Figure 4.4 with either AC-coupled or DC-coupled proposed in [154]. Indeed, such DC ultra-fast charging stations can be considered as AC/DC/Hybrid MGs with all their challenges [52], [192], [193]. In order to increase the charging station third-party interests, the optimal sizing of the energy storage system is performed in [194] through the station energy and storage cost reduction.

Due to the extensive use of power electronic converters, the main grid hugely suffers from power quality problems. Satisfying grid-code requirements could be another challenge in the high-power application for both flows of power. Proposing new converter topologies for the AC-DC and DC-DC power conversion stages with advanced control methods could solve this problem. In addition, it could add some advantages to the DC ultra-fast charging station, including modularity, bidirectional power flow capability, and higher efficiency in high-power applications. The optimum design of input filter to reduce the size of system and EMI effect is another important challenge. It should be noted that the different power converters topologies with various control methods could have different small-signal behaviours; therefore, transient performance analysis of DC ultra-fast charging stations could be another open research area and needs more attraction.

In terms of DC-coupled ultra-fast charging stations, the safety issues needs new definitions and structures [195]. Furthermore, in the range of high-power transfer, the power loss during EV charging and discharging would increase due to the increase in the current value. Therefore, the measurement of power losses needs more attention [196]. The challenges in the DC ultra-fast charging station are summarized in Figure 4.6.

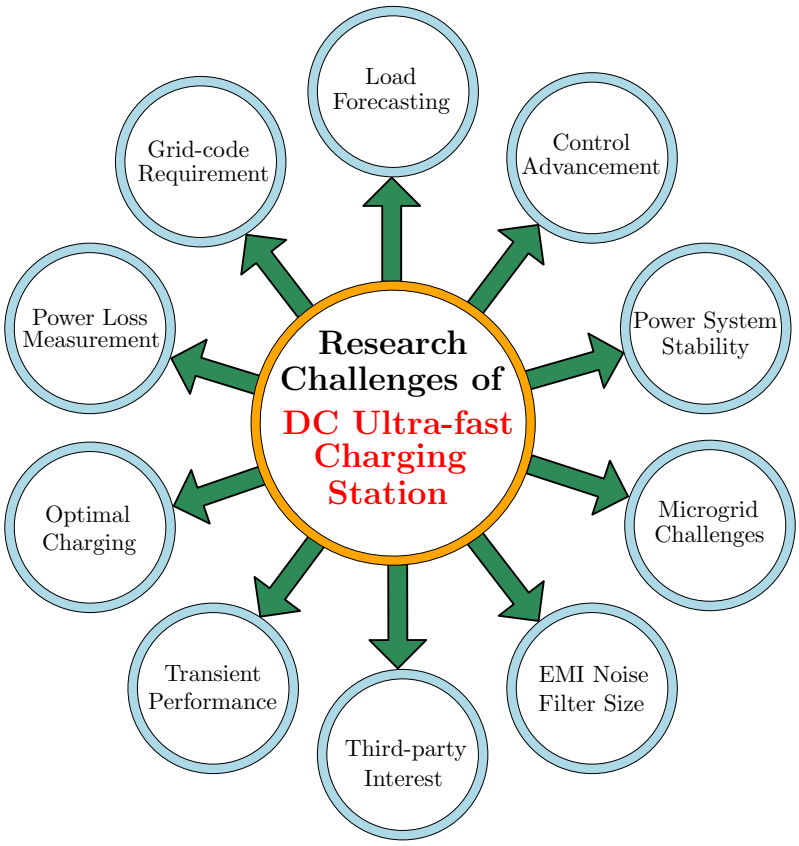

Figure 4.6: Research challenges in the DC ultra-fast charging stations.

4.5 SST

Traditional LFTs have been extensively used in power systems to step-down or step-up the voltage level. However, due to the low operation frequency, their weight and size are huge [197]. Therefore, their installation cost and insulation techniques are expensive. Moreover, the control freedom in the input/output voltage/current is limited and it can only be done by mechanical tap changers [198]. These barriers force the researchers to think about an alternative solution for the voltage level changes in power systems [199]. Thanks to the advancement in power electronic switches based on wide-bandgap materials such as SiC and GaN for high-power high-voltage applications, the SST which is also known as power electronic transformer firstly introduced in [200], solves all the issues of LFTs [201]. In the SST, voltage-level changes is performed by means of a medium-to-high frequency transformer which significantly reduces its size and weight. This is the reason why they are vastly adapted in railway applications for power electronic traction transformers [202] as well as in shipboard power systems [203]. In addition, thanks to power electronic switches in the input/output of SST, capabilities of power flow control, voltage sag/swell compensation [204], fault current limitation, and satisfactory grid-code requirement are added to the system [205]. Also, the distribution feeders have less power losses in SST-based power systems [10]. However, these options add complexity to the SST in terms of control, reliability, and protection which needs more careful design than LFT to guarantee their smooth and stable operation in the power systems. Moreover, the standard efficiency of distribution transformers should be higher than 97% according to the U.S. Department of Energy [206] which is relatively high for the converter-based SSTs [199].

4.5.1 SSTs Classification

SST topologies can be classified from different points of view [207]. The first one is based on the power conversion stages. Since SSTs work at medium-to-high frequency, a power conversion stage is needed to increase the SST input voltage frequency. Therefore, the simplest configuration of an SST consists of an isolated AC-AC conversion stage, stepping-down from HVAC to LVAC, with high-frequency transformer as shown in Figure 4.7a [208]. This SST topology is called single-stage or type A. The advantages of this configuration are high-efficiency, simple control, high power density, and high reliability. However, the lack of a DC-link and huge size of the input/output passive filters to reduce the switching ripple are some of its disadvantages. Different types of AC-AC power converters have been used in single-stage SST such as DAB converter [209], FB converter [108], flyback converter [210], matrix converter [211], and Dyna-C [212]. However, this suffers from lacking of PFC and active filtering in the input side. In order to have a bidirectional power flow in AC-AC DAB converter, four-quadrant switch cells is used with phase-shift modulation technique [213]. The second possible topology for the SST is shown in Figure 4.7b and is called two-stage or type B. In the secondary side of the high frequency transformer (HFT), an AC–DC conversion stage is used to provide the low-voltage DC (LVDC). The AC-DC isolated boost and the AC-DC DAB are examples of power converters used in type B. The disadvantages are the different control methods in each direction of power flow as well as non-existence of HVDC link which can yield larger second-order frequency ripple in the LVDC link [214]. Similar to the this topology, the two-stage or type C configuration illustrated in Figure 4.7c provides a high-voltage DC (HVDC) in the primary side of the HFT. The AC-DC conversion could be performed through a DAB converter for a wide range of load change. The integration of large renewable energy power plants is available in the HVDC link. The last possible

topology is a three-stage conversion or type D with high-frequency isolation illustrated in Figure 4.7d. In this topology, both LVDC link and HVDC link exist which provides more control freedom than in other topologies [215]. The integration of small and large sources of renewable energies in both DC links is easier. This is the reason why this topology has got more attraction in the industry. It is proposed in several papers that the type D topology with DAB converter has the best performance and controllability [216]. A comprehensive review of high-frequency DC–DC converters in high-voltage applications can be found in [217] and [218]. They can be used in the DC-DC section of type D SST topology. The disadvantage of type D topology is its lower efficiency than in other configurations due to the use of more power conversion stages. A detailed classification of SST topologies can be found in [219]. From another point of view, SST topologies can be classified based on the connection of power electronic converters in the input/output. The maximum blocking voltage of power electronic switches in previous generations was 6.5 kV. In order to connect the aforementioned possible SST topologies to the MV grids, series or parallel connections in the input/output are proposed for high-voltage and high-power applications. Four possible solutions are input series output parallel (ISOP), input parallel output series (IPOS), input parallel output parallel (IPOP), and input series output series (ISOS) in which all possible topologies from power conversion stages point of view could be used. Furthermore, these kinds of topologies add modularity feature to the SST, leading to higher reliability but also to control complexity. Meanwhile, thermal and insulation design in the MV side is a challenging task [220]; therefore, simple configuration with high-voltage high-power devices is more preferable like a two-level bridge. However, due to the poor harmonic performance, a huge passive filter is needed. As a result, the use of multi-level converters have more advantages in the MV side such as modularity, smaller passive filter, higher reliability, and fault tolerant capability. Examples of multi-level converters used in the MV side of SST are NPC [221], FC [222], CHB [223], and

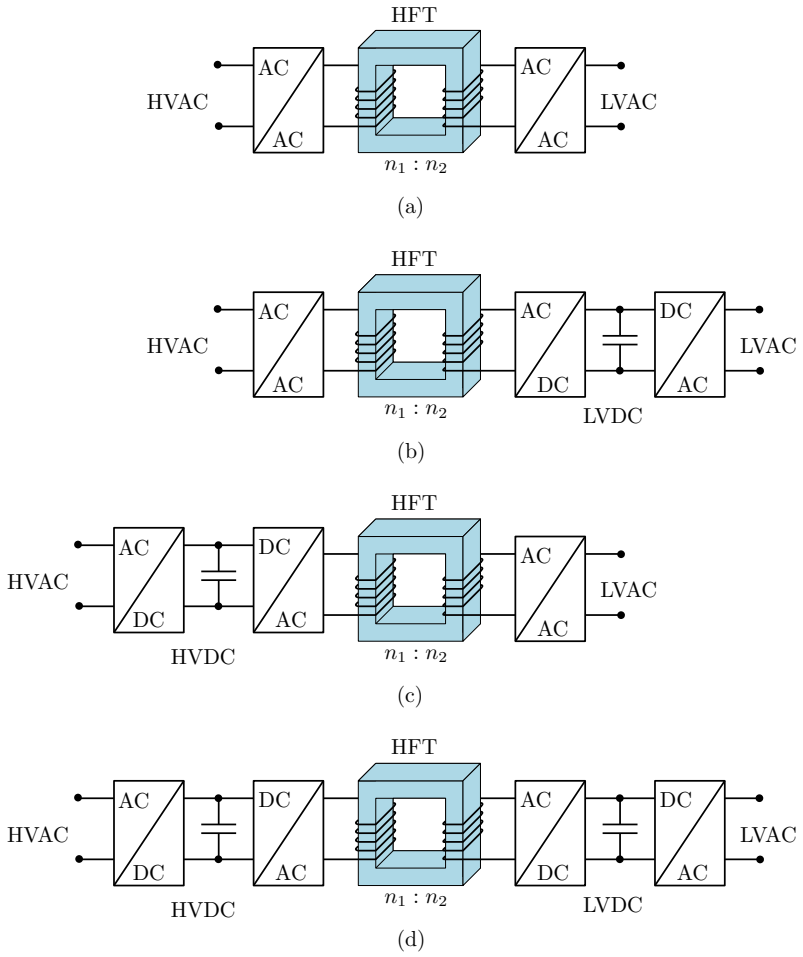

Figure 4.7: Different topologies of SST from power conversion stages point of view: (**a**) single-stage (type A); (**b**) two-stage with LVDC link (type B); (**c**) two-stage with HVDC link (type C); (**d**) three-stage with LVDC and HVDC link (type D). [208]

MMC [224], [225]. Figure 4.8 shows the different possible topologies of SST according to the input/output connection of power electronic converters. According to the aforementioned SST classifications and existence of different types of power electronic converters, a wide variety of SST topologies with various power converters can be achieved. SST can

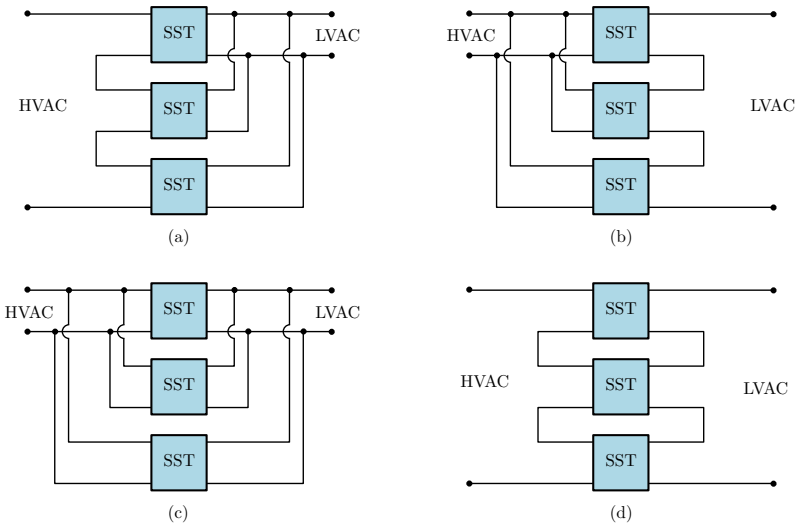

Figure 4.8: Different topologies of SST from the input/output connection of power electronic converters point of view: (**a**) ISOP; (**b**) IPOS; (**c**) IPOP; (**d**) ISOS.

also be classified based on their windings configuration. The SST windings can be the same as single-phase [226], three-phase [227], single-phase multi-winding [228], three-phase multi-winding [229], split winding [219], and Scott-T transformers [230]. In [231], the HF transformers is replaced with loosely coupled inductive power transfer (IPT) coils leading to simple high-voltage insulation, low parasitic capacitance, reduction in the number of output power electronics converter, easy packaging, and scalability although lower efficiency. There are still other classification of SSTs based on voltage level, control of isolation stage, and modularity structure which are reported in [20].

4.5.2 SSTs Power Devices

Power devices in SSTs can be classified as high-voltage switches in the primary side, high-frequency transformer (magnetic and winding structure), and low-voltage switches in the secondary side. The selection of these devices is related to the used power converter topology, voltage and power levels [232]. Furthermore, the switching and transformer losses which are directly related to the switching frequency play important roles in the efficiency, power density, lifetime, and junction temperature [233], [234]. Therefore, it is important to optimally select the SST power devices in each specific application leading to the more efficient SST with reduced size and cost.

There are three types of power losses in semiconductor devices including conduction losses, switching losses, and blocking losses [235]. Among them, the blocking losses can be neglected [236]. Since the semiconductor switches are not ideal, there is a power loss during switches conduction period which is called conduction losses. Therefore, semiconductor switches practically have on-state resistance or along voltage drop [237]. The conduction v-i characteristics of switches and anti-parallel free-wheeling diode can normally be found on the switches datasheets which is dependent to the operating temperature. Therefore, the different thermal model and thermal insulation for the switches lead to the various power losses which could be exclusive in each application. The voltage and current in the semiconductor switches can not immediately change from zero to maximum or vice versa. Therefore, during turn-on and turn-off switching events, the voltage and current intersect each other yielding switching power losses [238]. In order to reduce switching power losses, the most usable method is to manipulate voltage and current waveform during turn-on/turn-off transition through gate driver circuit and the external circuit. An alternative solution is to use soft switching techniques in which some passive components

such as extra capacitor, inductor, and diode are added to the circuit. Zero voltage switching (ZVS) and zero current switching (ZCS) are examples of soft switching techniques [239]. It is shown in [240] that the modulation method of a PWM converter has a great impact on its conduction and switching losses. Therefore, proposing different modulation methods can yield reduction in conduction and switching losses. Device manufacturers are still optimizing switches to reduce the switching losses.

4.5.2.1 High-voltage Side Switches

In the high-voltage high-power application, the most usable semiconductor device is Si IGBT, for instance the 6.5 kV-25 A Si IGBT. However, the MOSFET has better switching characteristic in comparison with the IGBT [241]. Parallel connection of IGBT and MOSFET is proposed in [242] which shows higher efficiency and more desirable switching characteristic. The new generation of wide-bandgap semiconductor devices such as SiC MOSFET and SiC IGBT has emerged recently. They have higher blocking voltage, less switching losses, high thermal conductivity, and high operation frequency [243]. Therefore, the SiC-based power electronic converters could be more efficient and could work in high operation temperatures [21]. The disadvantages of these switches are their high cost and non-commercializing. In addition, there is an oscillatory behavior in the SiC-based semiconductor devices during turn-off switching period which can be damped through a parallel connection of Si IGBT and SiC MOSFET [244].

In the high-voltage high-power application, another problem of power electronic switches is their high output voltage slopes (dv/dt) due to the fast switching [245]. This phenomenon can cause voltage amplifications which may shorten the transformer winding lifetime [246]. Furthermore, the gate-driver EMI is an aftermath of high dv/dt [247],

[248]. In the high-voltage side, maybe a series connection of switches should be used which can worsen dv/dt issue [249]. Different solutions have been proposed to solve the dv/dt issue. The most known one is to use a passive filter in the input/output [250]. The optimal selection of CHB cells in the MV side is another alternative solution to make a trade-off among efficiency, power density, and dv/dt issue [251], [252]. Another interesting solution is proposed in [253], where a new topology (S4T) was suggested for the soft-switching of three-phase SST which has higher efficiency, lower dv/dt rate, higher power density, longer lifetime, and less EMI.

Since the primary side of an SST is connected to the MV grid, the power electronic switches should be high-voltage low-current. The new wide-bandgap semiconductor devices such as the 10 kV-10 A SiC MOSFET, 15 kV-10 A SiC MOSFET [254], and 15 kV-20 A SiC IGBTs could be promising solutions in the SST primary side since simpler structure can be used in the MV grid [255]. The blocking voltage of the switches is increasing, as an example, a 4H-SiC n-IGBTs with the ratings of 27 kV-20 A is built in [256]. However, in simple structure like two-level converters, the dv/dt issue and switches stress are worse than in multi-level converters reaching up to 100 kV/μs. Therefore, a careful design of modules, gate drivers, busbars, and passive filters for switches is necessary in such stress level [257].

4.5.2.2 High-frequency Transformer

The second power device of the SST is the HFT which should satisfy the requirements of high-voltage, high-power, and high-frequency operation. The HFT consists of magnet core, primary winding, and secondary winding. A comprehensive explanation of HFT design is presented in [258]. The magnetic material and its geometry has a direct impact

on the transformer power density and losses [259]. Different kinds of magnetic material such as powdered iron, silicon steel, ferrite, amorphous, and noncrystalline have been used in the transformers, the last three being the best ones for HFT [260]. They can be compared with each other in terms of core losses, saturation flux density, operating temperature, and relative permeability [261]. In terms of core geometry, different kinds, such as core type, shell type, matrix type, and co-axial winding type have been used in the past [262]. These parameters are conflicting objectives; therefore, the optimal design of HFT magnetic material, geometry, and frequency needs a trade-off among all of them and it would be a multi-objective optimization problem [263], [264].

At the high frequencies, the efficiency of HFTs also depends on the material and configuration of the primary and the secondary winding because of skin and proximity effects [265]. Copper and aluminum are the common LFT winding materials. The transformer short circuit current has an impact on melting points which plays a critical role in the selection of winding material [266]. In addition, due to the skin and proximity effects, the circular shaped conductors are not a good choice for the HFT. Therefore, Litz wire, foil conductors, and primary and secondary interleaving have been used for the HFT [267] in which factors such as window dimensions, window utilization, window fill factor, and transformer turn ratio should be optimally designed [268].

In the HFT, the cooling material can not be the oil like LFTs. Moreover, the insulation material should tolerate partial discharges to provide a good insulation. The examples of insulation materials are Nomex paper and Mica. Therefore, thermal and electrical insulation design is a challenging task in high-voltage high-power application in the compact SST due to the excess of power losses [269].

4.5.2.3 Low-voltage Side Switches

The last power device of an SST is the secondary side low-voltage switch. Different types of these switches are commercially available and they are analysed comprehensively in a wide range of applications.

4.5.3 SSTs Applications

SST has been used in different kinds of applications [270] such as wind energy [271], [272], locomotives and traction systems [273], [274], interfacing asynchronous grids and loads [275], distribution network [199], smart grid development [230], [276], house power systems [277], and EV charging stations [278]. Details of some of implemented SSTs are shown in Table 4.4. Moreover, different converters, input/output configurations, and topologies have been used for each power stage of type D SST such as AC-DC and DC-DC power stages. As an example, by considering 31 kinds of three-phase AC-DC converters in [140] and 8 types of isolated DC-DC converters in [218], a total number of 248 SST type D topologies could be implemented. It should be noted that, each converter type and configuration could have different number of switches with different blocking voltage levels, diodes, and passive elements which have a direct impact on the cost, size, and reliability of the SST. Therefore, topology, switches, and passive elements selections could be an optimization problem in the SST design procedure. It can be perceivable from the Table 4.4 that in the high-voltage high-power application, there is still a gap between LFT efficiency (higher than 99.5%) and SST efficiency (96.5%) which needs more attention.

4.5.4 SSTs Transient Performance

In the future renewable electric energy and management (FREEDM) distribution network, the SST will play a critical role as an energy management unit or energy router. In this network, the renewable energy sources and energy storage integration is possible with plug-and-play functionality. Control freedom, intelligence and possible communication features of SST in the future smart grids can facilitate high penetration of intermittent renewable energies leading to improvement in the system reliability. Therefore, a small-signal analysis is required to check the operation of SSTs during sudden load/generation changes. In order to do a small-signal analysis, the state-space model of the system is needed. Since the SST topology could be different by the use of various types of power converters, there exists a wide variety of SST state-space model. The simplified state-space average model of an SST type D is presented in [279] in which the AC-DC and DC-DC stages are performed through CHB and DAB converters respectively. The time-scales of SST different modes are within 10^{-3} ms and 0.1 s [280]. Moreover, a comprehensive mathematical model of an SST including power stages and closed loop controllers are reported in [281]. These models can also be used for the general power system studies and implementation in real-time digital simulators [282]. A 70th-order simplified state-space average model of a FREEDM network including single SST, energy storage, DC loads and sources, and AC loads and sources is derived in [280]. Therefore, in the distribution networks in which the LFTs are replaced by SSTs, interactive dynamics may appear among SSTs. As an example, second order harmonic oscillation can appear in the AC side of the AC-DC power stage leading to DC-link voltage variation, harmonic resonance among SSTs, and the system instability [283]. Therefore, an optimal design of SST controllers based on eigenvalue analysis can improve transient performance of the whole network.

Table 4.4: Experimentally implemented SSTs in the literature for different applications.

Application	**SST type**	**Power rating (KVA)**	**MV (kV)**	**AC-DC rectifier**	**DC-DC converter**	**SST efficiency**	**DC-link (HVDC LVDC)**	**High-voltage switches**
Distribution network [284]	D	1.67	1.15	FB (75 kHz)	Switched-capacitor LLC-SRC (75 kHz)	93%-97%	1.7 kV 600 V	3 kV-12 A IGBT / 1.2 kV-20 A SiC MOS-FET
Fast Charging [285]	D	4	0.22	CHB (1.05 kHz)	QAB (10 kHz)	N/A	0.36 kV 220, 120, 48 V	N/A
Smart grid [286]	D	10	3.6	CHB (1.2 kHz)	DAB (3.6 kHz)	84%-92%	5.7 kV 200 V	6.5 kV-25 A Si IGBT
Distribution network [287]	D	10	3.6	FB (6 kHz)	DHB (15 kHz)	N/A	6.1 kV 400 V	13 kV-10 A SiC MOS-FET/JBS diode
Distribution network [288]	D	10	13.2	3-level PFC (20 kHz)	LLC (40 kHz)	N/A	25 kV 500 V	1.7 kV-5 A SiC MOS-FET
Fast Charging [289]	D	16	3.8	TLB (20 kHz)	HB-LLC (98 kHz)	98%	6.2 kV 400 V	1.2 kV-31 A SiC MOS-FET
Wind energy [290]	D	20	7.2	CHB (1.08 kHz)	DAB (3 kHz)	88%-95%	11.4 kV 400 V	6.5 kV-25 A IGBT
Utility network [291]	D	25	7.2/8	TLB (93 kHz)	HB-LLC (93 kHz)	97.5%	14 kV 400 V	1.2 kV-36 A SiC MOS-FET
Data Centers [292]	D	25	3.8	FB (48 kHz)	LLC-SRC (48 kHz)	98%-99.6%	7 kV 400 V	10 kV-10 A SiC MOS-FET
Fast Charging [293]	D	25	2.4	TLB (25 kHz)	NPC+diode rectifier (50 kHz)	96.6%	4.8 kV 400 V	1.2 kV-55 A SiC MOS-FET
Mobile utility support [294]	D	100	4.16	AFE (20 kHz)	DAB (10 kHz)	N/A	7.2 kV 800 V	10 kV-90 A Gen3 SiC MOS-FET
Fast Charging [295]	D	400	13.2/4.8	NPC (5 kHz)	LLC-SRC (100 kHz)	96.5%	6.4 kV 1000 V	1.2 kV-50 A SiC MOS-FET

The state-space average model of SST can also be used in the protection studies to anticipate the SST performance under fault conditions. Through the state-space model of SST, over-voltage and over-current protection schemes and voltage ride through capabilities can be proposed [296].

4.5.5 SSTs Challenges and Research Gaps

There exists a great deal of challenges in the application of SSTs. The first one is the design of SST high frequency core and windings in which material advancement is still ongoing. A proper thermal design of SST core and windings can improve its efficiency which is currently lower than the one of LFT in high-power applications.

In the vast adaptation of SSTs in power distribution network, feasible and dynamic stability analysis, power system analysis, and reliability concern due to the existence of power electronic switches are significantly important factors. In SST-based power distribution networks, the requirement of extra communication and control layer looks necessary. Moreover, it should be noted that since the conventional mechanical MV circuit breakers are too slow, a fast-acting protection scheme is needed for the protection of MV power electronics switches during fault conditions. Therefore, implementation of fast circuit breakers with solid-state materials could be another interesting research area in this field.

Another challenge is the unbalance problem which can appear in the modular configuration of SST between the phases. Short-circuit faults and uneven distribution of loads can cause unbalanced operation in the power system. Furthermore, the three-phase grid voltages are not always balanced. In unbalanced operation mode, negative sequence current will be drawn or injected from or to the grid. These may cause double-frequency ripples,

and unbalanced voltages in the SST DC-links of each phase which can damage power electronic components due to the increase in the semiconductor devices stress, over-voltage and over-current [297]. Therefore, SSTs should properly work in unbalanced three-phase grid voltages and have the compensation capability of the three-phase grid currents in a cost-effective and reliable manner [298]. Unbalanced operation of SSTs is investigated in [297] and [299]. The most widely used unbalance compensation technique in the literature is zero sequence voltage injection [300] which leads to the choice of power devices with higher rating and power losses [301]. The challenges in the application of SSTs still under research are illustrated in Figure 4.9.

Figure 4.9: Research challenges of SST.

4.6 DC Ultra-fast Charging Station with SST

An interesting solution for the power stage 1, voltage level changes, in the DC ultra-fast charging station shown in Figure 4.4 is to utilize SST instead of LFT which can perform rectification, voltage step-down, and isolation function altogether. Thanks to the high frequency operation of SSTs, their size and weight would be much lower than conventional service transformers [302]. Therefore, the DC ultra-fast charging station installation cost and footprint would hugely decrease [99]. Furthermore, the employed power electronics switches in the input and output of SSTs gives the full controllability of the input/output voltage/current which can provide reactive power control, satisfactory grid-code requirement, grid ancillary services, and higher efficiency than the conventional charging stations [303]. Moreover, the presence of DC-links in the three-stage SST architecture could facilitate integration of renewable energy sources and energy storage as well as could decrease power conversion stages increasing the efficiency [304]. This integration possibility in the DC-links could maximise interest for the owners of DC ultra-fast charging stations and could provide ancillary services for the grid [305]. Another advantage of the DC SST-based ultra-fast charging station is its capability for bidirectional power flow which could provide ancillary services for the grid, shave the grid peak load, and facilitate the V2G, V2H, and V2V applications [306]. Furthermore, thanks to the modularity of SSTs in the input side, any increase in the DC SST-based ultra-fast charging station power capacity could be easily performed while replacement of LFT is necessary in the DC LFT-based ultra-fast charging station. In order to implement a DC SST-based ultra-fast charging station, different aspects should be investigated as explained below.

4.6.1 Topology Configuration

As mentioned previously, there are four types of SST configurations which can be used in the DC ultra-fast charging stations. Among them, type D (Figure 4.7d) is the suitable choice thanks to its higher control freedom. The choice of power converters for the AC-DC and DC-DC power stages could play a vital role in the performance of DC SST-based ultra-fast charging station. The single-phase and three-phase AC-DC power converters can be used in the first power stage such as HB, FB, AFE, three-level PFC, NPC, TLB, TLT, MCB, VR, CHB, MMC, four-wire bidirectional boost converter, four-legged bidirectional boost converter, matrix-converter bidirectional buck–boost, and so on. In isolated DC-DC power stage, power converters such as DAB, series-resonant DAB, PSFB, LLC-SRC Full-bridge, hybrid switched-capacitor LLC-SRC, DHB, QAB, NPC, DAB-ANPC, FC, CLLC, and any other novel topology can be utilized. Some of the possible power electronic converters which could be used in a DC SST-based ultra-fast charging station are shown in Figure 4.10.

Furthermore, the SST can be used in ISOP, ISOS, IPOP, and IPOS (Figure 4.8) configurations which adds modularity to the whole circuit [307], facilitating its use in high-voltage high-power application and reducing the size of input passive filters. From a topological point of view, SSTs in the DC ultra-fast charging stations could be categorized as single-phase single-port (SPSP) [308], single-phase multi-port (SPMP), three-phase single-port with single-phase converters (TPSP-SPC) identically connected in delta or wye [309], three-phase multi-port with single-phase converters (TPMP-SPC) identically connected in delta or wye [285], [310], and three-phase single-port with three-phase converter (TPSP-TPC) or three-phase multi-port with three-phase converter (TPMP-TPC) either connected

in delta or wye configurations. Therefore, an optimal selection of DC SST-based ultra-fast charging station configuration needs more attention. The aforementioned topology architectures are illustrated in Figure 4.11.

4.6.2 Transient Performance

A DC ultra-fast charging station could be similar to a FREEDM network with single SST. Therefore, the state-space average model of the DC ultra-fast charging station is a high order. This model should be considered for the dynamic stability and small-signal analysis in order to guarantee a stable and feasible operation in the charging station. It should be noted that different configurations and topologies yield a wide variety of state-space average model. Since the ultra-fast charging stations could have more than one charge ports for the EVs, immediate disturbances or load changes can take place specifically during the fast-charging mode of operation for the EV batteries. Therefore, the transient performance of the charging station should be deeply investigated. Methods should be proposed for the improvement of the transient performance through passive (adding passive elements to the circuit) or active (manipulating control loops or using different control strategies) techniques [311]. The dynamic stability issue could be worsen for the distribution network with the dense penetration of DC ultra-fast charging stations [312]. Smart and dynamic charging techniques could solve this problem. In addition, the smart charging techniques could have advantages such as optimization of the EV charging price in variable grid prices, grid load peak shaving, grid ancillary services, and lower reserve generation capacity [313].

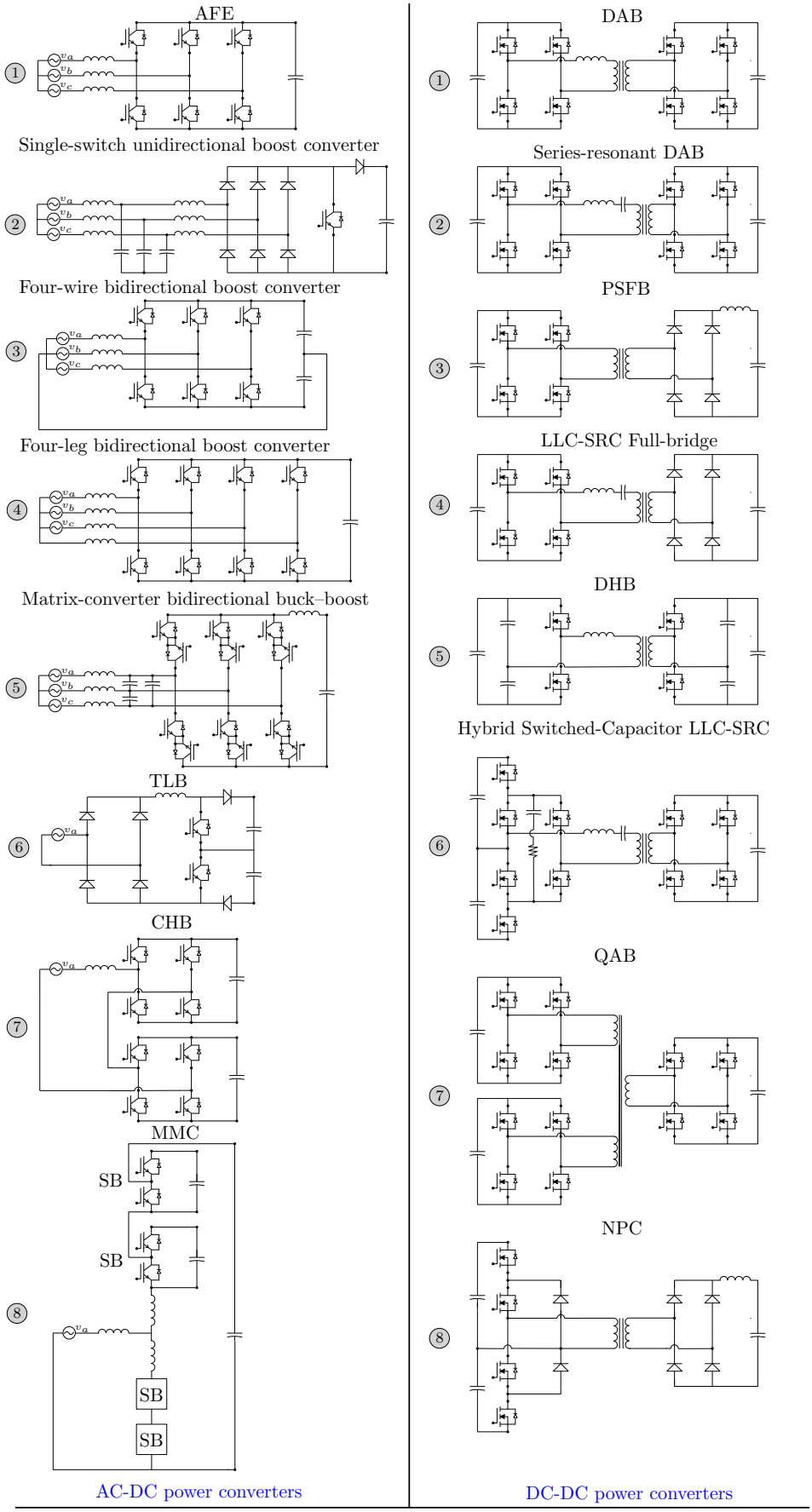

Figure 4.10: Some of possible power electronic converters that can be used in a DC SST-based ultra-fast charging station.

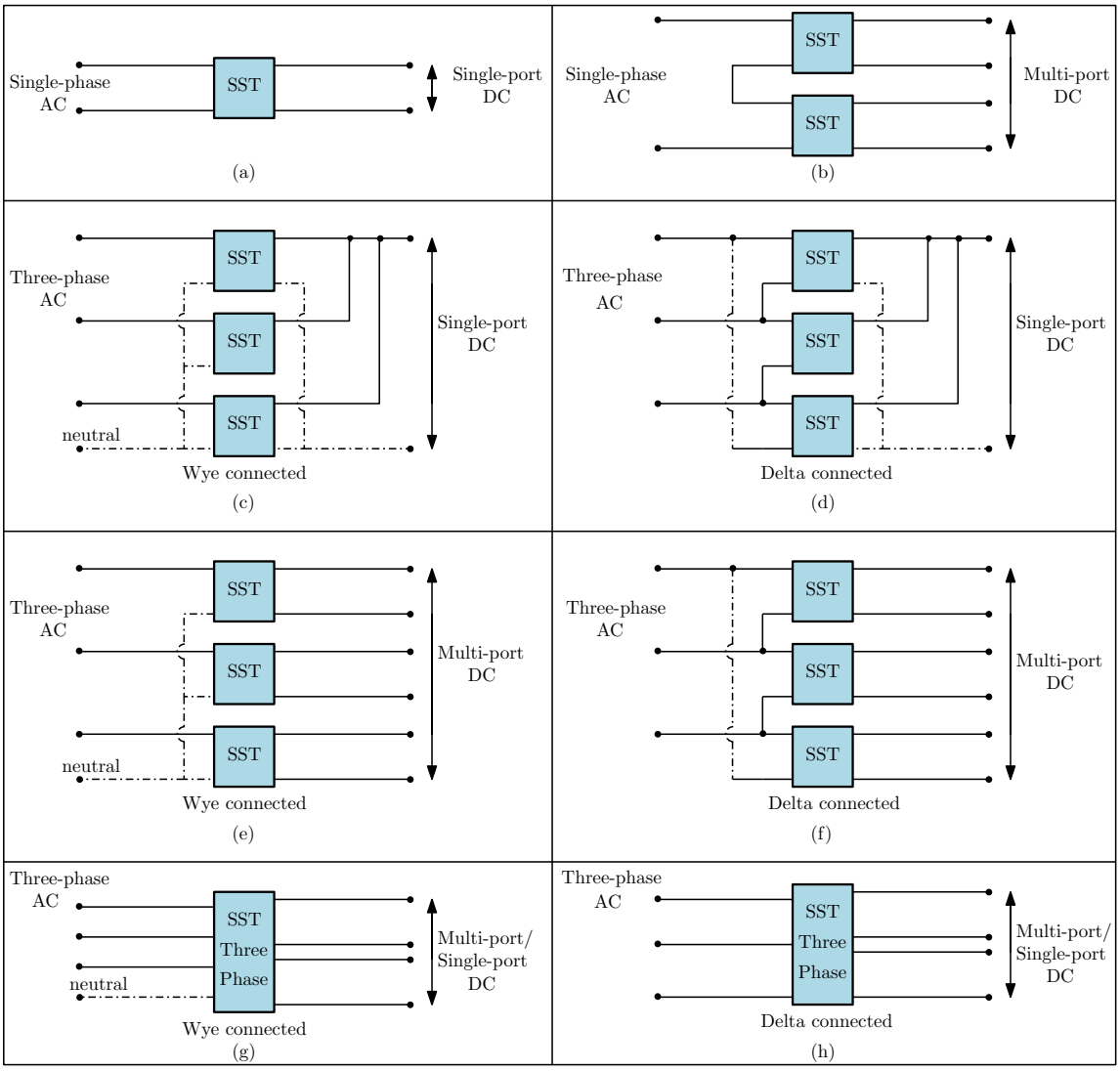

Figure 4.11: Topology configuration based on input type and output ports: (**a**) SPSP; (**b**) SPMP; (**c**) TPSP-SPC wye connected; (**d**) TPSP-SPC delta connected; (**e**) TPMP-SPC wye connected; (**f**) TPMP-SPC delta connected; (**g**) TPSP-TPC/TPMP-TPC wye connected; (**h**) TPSP-TPC/TPMP-TPC delta connected.

4.6.3 Energy Management and Optimal Sizing

The size of DC ultra-fast charging station is related to the urban traffic flow based on the factors such as road system, location, direction, intersections and length [314]. In the DC SST-based ultra-fast charging station equipped with distribution generations and energy storage, intelligent energy management system (IEMS) is required to increase the interest of charging station's owner. The IEMS can decide between charging/discharging schedule of energy storage [315], [316] and participation in grid ancillary services [303]. In addition, the required charging power of DC ultra-fast charging station is uncertain due to different reasons such as arrival time and SOC of the EVs [317], [318]. Therefore, the load profile of DC ultra-fast charging station is not a constant power load from distribution network point of view. In order to predict the charging stations load profile, curve fitting through standard exponential load model [319], conventional optimization [320], and machine learning techniques have been used in the literature [321]. By means of these methods, the optimal sizing of the resources in DC ultra-fast charging stations is achievable [106]; thereby leading to maximising third-party interest [322].

4.6.4 Power Imbalance Problems

In order to keep the modularity of DC SST-based ultra-fast charging stations with three-phase AC grid voltage, power converters can be separately used in each phase connected in delta or wye. In these kinds of charging stations, each phase can have different power consumption according to the EV demand. In addition, there exists parameter mismatches in the real implementation of HFT (isolation stage) in each modules [323]. Therefore,

a power imbalance can occur in the station leading to DC-link voltage deviation, drawing unbalanced currents from the main grid, and increasing the total harmonic distortion (THD) of the grid current. To solve this issue, the zero-sequence current is added to the reference currents of each phase [324]. However, this increases the magnitude of total current [325]. Therefore, semiconductor devices with higher rating current should be used. To mitigate this problem, in the DC-DC power stage of type D SST, power balance windings are added to the HFT and connected in parallel for all phases to reduce zero-sequence required current [285].

4.6.5 Control Methods

In a DC ultra-fast charging station with type D SST, different control objectives can spread among AC-DC and DC-DC power converters. The objectives of the AC-DC power converter are to keep the HVDC link voltage fixed to a reference value, to keep the grid synchronisation like by a PLL, to keep the injected grid current sinusoidal with a THD lower than 5% [326], to keep the injected three-phase grid current balanced, to keep robustness against grid voltage harmonics, to compensate grid voltage sag/swell, to limit the fault current or start-up current [327], to make a bidirectional power flow, and to keep unitary power factor in the grid-side or other power factors for injecting/consuming reactive power to/from the grid, providing ancillary services [328]. In multi-level structure at the input side of SST, the voltage balance among all the capacitors would be another control objective. In modular structure of SST implemented separately in each phase with three-phase input, power balancing is another important objective in order to improve the system performance. In this structure, if energy storage systems integrated with DC-links, making a balance in their SOC rates could be an interesting performance criteria.

The objectives of the DC-DC power converter are to keep the LVDC link voltage fixed to a reference value, to achieve ZVS/ZCS leading to lower stress on switches, to guarantee lower EMI and higher system efficiency, to provide galvanic isolation against high-voltage side, and to give a bidirectional power flow through leading/lagging of phase angle between primary and secondary bridge. Table 4.5 shows the desired performances that the control approach has to cope with them in DC SST-based ultra-fast charging stations.

Table 4.5: The desired performance of a SST-based DC ultra-fast charging station.

Power stage	Performance criteria
AC-DC power stage	• HVDC link voltage control • LVDC link voltage control • Grid current THD improvement • Grid synchronisation • PFC • ZVS/ZCS • Unidirectional power flow • Bidirectional power flow • Power balancing control • Voltage balancing control • SOC balancing control • Grid ancillary services • Fault tolerant and limitation
DC-DC power stage	• LVDC link voltage control • ZVS/ZCS • Galvanic isolation • Unidirectional power flow • Bidirectional power flow • Power balancing control

4.6.5.1 AC-DC Power Converter Control Approaches

In order to control the single-phase and three-phase AC-DC power converter, different control strategies have been used in the literature. The first popular one in three-phase converters is the voltage oriented control (VOC) which performs indirect control of active and reactive power through the current vector orientation [329]. The second popular control approach is the direct power control (DPC) which performs instantaneous active and reactive power control. Another popular control approach is the virtual flux (VF) technique [330] which mimics the control of electric motor drive systems. The proportional integral (PI) controller, proportional integral derivative (PID) controller, PR controller, sliding-mode controller (SMC), hysteresis controller, fuzzy logic controller (FLC), model predictive controller (MPC), adaptive controller, and neural-network-based controller are employed to satisfy the desired performance [140], [170].

4.6.5.2 DC-DC Power Converter Control Approaches

Various isolated bidirectional DC-DC power converters have been proposed such as resonant converters, dual flyback, dual-Cuk, dual push–pull, and DAB [160]. Among them, the DAB converter is the most usable one in the DC-DC power stage of DC SST-based ultra-fast charging station. The advantages of DAB converter can be listed as bidirectional power flow capability and fast power flow mode changing, wide voltage conversion range to interface different voltage levels, and ZVS capability to increase the efficiency. The feedback control, linearization control (PI/PID), feedforward plus feedback, disturbance-observer-based control, feedforward current control, MPC, SMC, and moving discretized control set MPC have been employed in the DAB converter to follow the

control objectives. Different modulation schemes have been used for the DAB converter such as single-phase-shift (SPS), dual-phase-shift (DPS), triple-phase-shift (TPS) [331], and extended-phase-shift (EPS) [332]. The DAB converter transfer power P with SPS modulation scheme is defined as follows [333]

$$P = \frac{N v_p v_s}{f_s L} \phi (1 - 2|\phi|) \tag{4.1}$$

where N, v_p, v_s, ϕ, f_s, and L are the DAB turn ration, DC input voltage, DC output voltage, phase shift, switching frequency, and inductance respectively. The DAB reduced-order model is a first-order transfer function and can be obtained by neglecting inductor current dynamics. This transfer function $G(\mathrm{s})$ from ϕ to v_s can be expressed as follows

$$G(\mathrm{s}) = \frac{\hat{v_s}}{\hat{\phi}} = \frac{N V_p (1 - 4\Phi)}{f_s L} \frac{R_L}{R_L C_2 \mathrm{s} + 1} \tag{4.2}$$

where V_p and Φ are the DC values of v_p and ϕ. R_L and C_2 are the resistance of output load and output capacitance respectively.

4.6.5.3 Analysis of Existing Control Approaches

Table 4.6 shows the existing control approaches of DC SST-based ultra-fast charging stations. For the control of the DAB converter, combining the LVDC-link voltage control with AC-DC rectifier control is a simple way which reduces the number of control loops but the DAB output voltage would be sensitive to the load variation. Another method is to control the DAB converter independently through PI control of LVDC and phase shift magnitude between primary and secondary windings. Grid voltage harmonics can cause ripples in the DC-links and can have adverse effects in conventional VOC for three-phase

AC-DC rectifiers.

4.6.6 DC SST-based Ultra-fast Charging Station Social Repercussions

The DC SST-based ultra-fast charging station has different impacts on the community. One of the most positive impacts is that it will decrease the anxiety of the EV drivers since they can refuel their EVs in short time comparable to the one needed for refueling FFVs. Therefore, the drivers concerns about continuing their route on interurban roads would significantly decrease [341]. Moreover, bidirectional power flow capability and V2G application of DC SST-based ultra-fast charging station could increase people's participation in electrical network planning. Therefore, both the society and the government can benefit from this participation, leading to an increase in social welfare [342]. Another impact of the DC SST-based ultra-fast charging station on the community is that the needs of carrying fuel with big tankers which is a dangerous and time-consuming task would be removed.

To summarize, the vast adaption of DC ultra-fast charging stations could hugely facilitate reaching a sustainable life in the coming future. As a result, the environmental activists and the whole society would be more satisfied [95].

4.6.7 DC SST-based Ultra-fast Charging Station Challenges and Research Gaps

In addition to the previously mentioned challenges, there are still other gaps in the application of DC SST-based ultra-fast charging stations. One of them is cybersecurity and

Table 4.6: Literature control approaches of DC SST-based ultra-fast charging station.

References	AC-DC power converter	AC-DC control approach	DC-DC power converter	DC-DC control approach
[285]	CHB	Cascaded PI control: • PFC • Grid synchronisation • Power balancing control • Voltage balancing control • HVDC link voltage control	QAB	PI control: • DPS bidirectional power flow • Galvanic isolation • Power balancing control • LVDC link voltage control
[289]	TLB	Digital PI control: • PFC • Grid synchronisation • Voltage balancing control • HVDC link voltage control • Grid current THD improvement	HB-LLC	Digital open-loop control: • Unidirectional power flow • Galvanic isolation • LVDC link voltage control • ZVS
[310]	CHB	Cascaded PI control: • PFC • Grid synchronisation • Power balancing control • Voltage balancing control • SOC balancing control • HVDC link voltage control	DHB	Digital PI+PR control: • Bidirectional power flow • Galvanic isolation • LVDC link voltage control • ZVS
[334]	CHB	PI control: • Grid ancillary services • HVDC link voltage control	DAB	PI control: • Bidirectional power flow • Galvanic isolation • LVDC link voltage control • ZVS
[335]	CHB	PI control: • PFC • Grid synchronisation • Power balancing control • HVDC link voltage control	DAB	Cascaded PI control: • DPS bidirectional power flow • Galvanic isolation • LVDC link voltage control
[336]	VR	Multi-loop PI and hysteresis current control: • PFC • Grid synchronisation • Voltage balancing control • HVDC link voltage control	DAB	Cascaded PI control: • SPS bidirectional power flow • Galvanic isolation • LVDC link voltage control
[337]	TLB	Multi-loop PI and predictive current control: • PFC • Grid synchronisation • Voltage balancing control • HVDC link voltage control	DAB-ANPC	PR control: • TPS bidirectional power flow • Galvanic isolation • LVDC link voltage control • ZVS
[338]	TLT	Digital multi-loop PI control: • PFC • Grid synchronisation • Voltage balancing control • HVDC link voltage control	N/A	N/A
[339]	CHB	Multi-loop PI and predictive power control: • Fault tolerant and limitation • Voltage balancing control • LVDC link voltage control	DAB	PI control: • SPS bidirectional power flow • Galvanic isolation • ZVS
[340]	MCB	PI control: • Voltage balancing control • HVDC link voltage control	NPC	PI control: • Power flow • Galvanic isolation • LVDC link voltage control

data protection schemes which should be addressed in the online control schematic for the future smart grids. Another challenge is the requirement of advanced protection schemes against short circuits, over-voltages, and overloading fault conditions with fast solid-state circuit breakers (current interruption in several hundred microseconds) [343]. The advanced protection scheme can guarantee the safety of EV owners and the personnel of DC SST-based ultra-fast charging stations. Reliability concerns of replacing the passive transformer with a power electronic equivalent could be another research challenge in this field. Furthermore, in the direct connection of DC ultra-fast charging station to the MV grid, safety, protection, standardization and certification of the EV charging equipment are necessary. To summarize this section, the research challenges in the DC SST-based ultra-fast charging station is presented in Figure 4.12.

4.7 Conclusions

The electrical architecture of an ultra-fast charging station offers numerous open aspects to investigate. In that context, the low-frequency service transformer could be substituted by an SST with the aim of increasing the control capability and reducing the size and weight. The SST is considered any conversion structure implemented with switching power converters that is capable to transform AC MV into DC in the range between 200 V and 500 V.

The main features of existing SSTs in renewable energy applications have been reviewed in this chapter underlying the rated power, the MV magnitude, the topology of both AC-DC and DC-DC stages, the voltage level in the DC link, the voltage stress supported by the high-voltage switches, and the resulting efficiency.

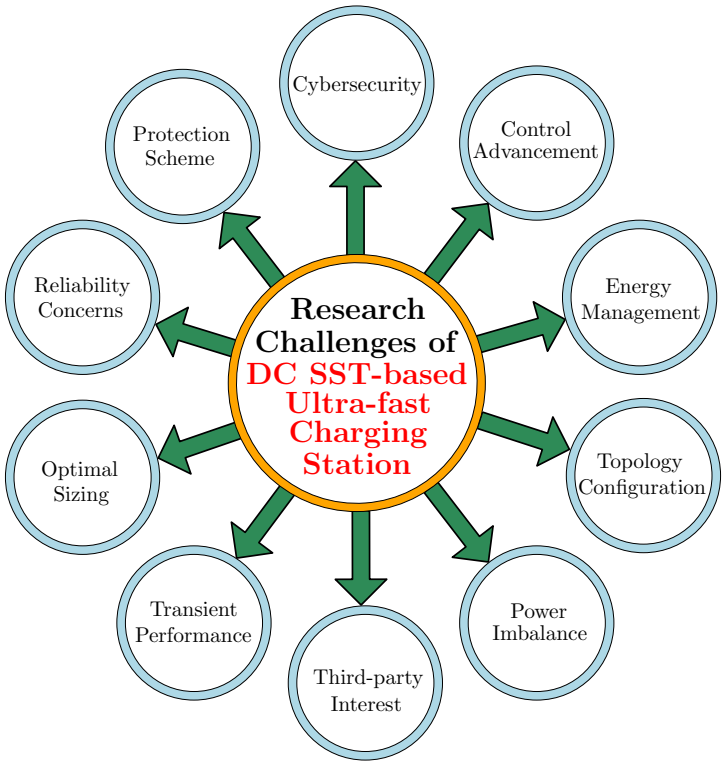

Figure 4.12: Research challenges in the DC SST-based ultra-fast charging station.

The penetration of SSTs in ultra-fast charging stations is an incipient stage but there are already important antecedents in fast charging. A classification of SST-based electrical architectures for charging stations have been presented in this work considering the type of input, number of output ports, and converter configuration. Four SST configurations have been identified with potential use in ultra-fast charging, being the type D the most appropriate one. Other aspects to be considered in the design of the SST are the stability of the interconnection with the rest of the blocks in the ultra-fast charging station, and the energy management in a hierarchical supervision system that should also handle the control of the different converters solving power imbalance problems.

Chapter 5

Conclusions and Future Work

5.1 Conclusion

This thesis encompasses a comprehensive investigation into various challenges encountered in MGs and presents novel approaches to address them. The focus areas include control strategies, stability analysis, power sharing, power converter design, grid connection, and renewable energy integration. The research findings provide valuable insights into the design and optimization of MG systems, enabling improved performance and reliability.

The first aspect explored in this thesis is the control of PV-fed multifunctional grid-connected inverters. A shunt APF control strategy was developed to compensate for nonlinear and unbalanced loads. By utilizing a quasi-PR controller with harmonic compensators and employing optimization algorithms, the system achieved maximum power extraction, harmonic compensation, and reactive power control. The proposed approach exhibited superior performance and adaptability under varying operating conditions.

The second area of focus involved the optimization of controller parameters in islanded MGs. By formulating an optimization problem based on a state-space model, the impact of operating point and output impedance variations on system stability was analyzed. Through the application of PSO, GA, and a combined PSO-GA approach, controller parameters were tuned to ensure stability and enhance performance. This methodology provided a simplified yet effective design approach for achieving stable operation in islanded MGs.

Lastly, the thesis investigated the electrical architecture of ultra-fast charging stations in MGs, with an emphasis on replacing low-frequency service transformers with SSTs. The potential benefits of SSTs, such as increased control capability and reduced size and weight, were explored. A classification of SST-based electrical architectures for charging stations was proposed, considering input types, number of output ports, and converter configurations. The findings highlighted the advantages of SSTs in ultra-fast charging, paving the way for more efficient and compact MG electrical architectures.

By integrating these research outcomes, this thesis contributes to a holistic understanding of MG challenges and solutions. The investigations into control strategies, optimization algorithms, and advanced electrical architectures provide valuable insights for the design and operation of reliable and efficient MG systems. The findings of this thesis contribute to the advancement of renewable energy integration, grid stability, and the development of sustainable and resilient energy systems.

5.2 Future Work

The conclusion of this thesis opens up several potential avenues for future research work in the field of MGs and their control. Building upon the findings and contributions of the current research, the following are some potential directions for future investigations:

- Advanced control strategies: while the current research explored control strategies for PV-fed multifunctional grid-connected inverters and islanded MGs, there is still room for developing and refining more advanced control algorithms. Future research could explore the use of advanced control techniques such as model predictive control, adaptive control, or machine learning-based control to enhance the performance, stability, and adaptability of MG systems under diverse operating conditions.

- Hybrid energy storage integration: the integration of energy storage systems in MGs plays a crucial role in enhancing grid stability, managing fluctuating renewable energy sources, and improving overall system performance. Future research could focus on the optimization of hybrid energy storage systems configurations, combining different storage technologies (e.g., batteries, supercapacitors) and exploring novel control strategies to achieve optimal energy management and grid support.

- Resilience and reliability: MGs are expected to operate in various environments and face uncertainties due to weather conditions, equipment failures, and cyber-attacks. Future research could delve into the resilience and reliability aspects of MGs, developing strategies to improve fault tolerance, self-healing capabilities, and seamless transition between grid-connected and islanded modes during emergencies.

- Power electronics and solid-state transformers: the use of SSTs in ultra-fast charging stations has shown promising results. Future research could further explore the design optimization, efficiency improvement, and cost reduction of SSTs for various applications in MGs, including voltage regulation, power quality enhancement, grid integration, and ultra-fast charging.

- Multi-MG interactions: as MGs become more widespread, the interactions between multiple interconnected MGs become important. Future research could investigate the coordination and control strategies for multi-MG systems to optimize power flow, enable seamless islanding and reconnection, and manage energy exchange between different MGs.

- Cybersecurity and communication: with the increasing integration of digital technologies and communication systems in MGs, ensuring cybersecurity becomes critical. Future research could focus on developing robust and secure communication protocols, encryption techniques, and intrusion detection systems to safeguard MGs against cyber threats and attacks.

- Real-world implementations and case studies: to validate the theoretical findings and control strategies, future research should involve real-world implementations of MG systems and conduct comprehensive case studies. Field trials and practical deployments can help identify practical challenges and optimize control strategies for real-world scenarios.

- Policy and economic analysis: integrating MGs into existing power systems often requires regulatory support and economic incentives. Future research could explore policy frameworks, market mechanisms, and economic models to promote the

widespread adoption of MG technologies and assess the economic benefits of MG implementation for various stakeholders.

To summarize, future research in the domain of MG should aim to further enhance their performance, reliability, and integration with renewable energy sources. By addressing the identified challenges and exploring innovative solutions, the field of MGs can play a pivotal role in achieving a sustainable and resilient energy future.

References

[1] S Chowdhury and P Crossley, *Microgrids and active distribution networks* (IET renewable energy series). Stevenage: The Institution of Engineering and Technology, 2009.

[2] M. Mahmoud, *Microgrid: Advanced Control Methods and Renewable Energy System Integration*, English. United States: Elsevier Inc., 2016, ISBN: 9780081017531.

[3] S. K. Sahoo, A. K. Sinha, and N. K. Kishore, "Control techniques in AC, DC, and hybrid AC–DC microgrid: A review," *IEEE Journal of Emerging and Selected Topics in Power Electronics*, vol. 6, no. 2, pp. 738–759, 2018. DOI: 10.1109/JESTPE.2017.2786588.

[4] T. Strasser, F. Andrén, J. Kathan, *et al.*, "A review of architectures and concepts for intelligence in future electric energy systems," *IEEE Transactions on Industrial Electronics*, vol. 62, no. 4, pp. 2424–2438, 2015. DOI: 10.1109/TIE.2014.2361486.

[5] D. Kumar, F. Zare, and A. Ghosh, "DC microgrid technology: System architectures, AC grid interfaces, grounding schemes, power quality, communication networks, applications, and standardizations aspects," *IEEE Access*, vol. 5, pp. 12 230–12 256, 2017. DOI: 10.1109/ACCESS.2017.2705914.

[6] J. M. Guerrero, P. C. Loh, T.-L. Lee, and M. Chandorkar, "Advanced control architectures for intelligent microgrids—part II: Power quality, energy storage, and AC/DC microgrids," *IEEE Transactions on Industrial Electronics*, vol. 60, no. 4, pp. 1263–1270, 2013. DOI: 10.1109/TIE.2012.2196889.

[7] M. Roslan, M. Hannan, P. J. Ker, M. Mannan, K. Muttaqi, and T. I. Mahlia, "Microgrid control methods toward achieving sustainable energy management: A bibliometric analysis for future directions," *Journal of Cleaner Production*, vol. 348, p. 131 340, 2022, ISSN: 0959-6526. DOI: https://doi.org/10.1016/j.jclepro.2022.131340. [Online]. Available: https://www.sciencedirect.com/science/article/pii/S0959652622009660.

[8] S. Devassy and B. Singh, "Design and performance analysis of three-phase solar PV integrated UPQC," *IEEE Transactions on Industry Applications*, vol. 54, no. 1, pp. 73–81, 2018. DOI: 10.1109/TIA.2017.2754983.

[9] J. M. Guerrero, J. C. Vasquez, J. Matas, L. G. de Vicuna, and M. Castilla, "Hierarchical control of droop-controlled AC and DC microgrids—a general approach toward standardization," *IEEE Transactions on Industrial Electronics*, vol. 58, no. 1, pp. 158–172, 2011. DOI: 10.1109/TIE.2010.2066534.

[10] A. Q. Huang, "Medium-voltage solid-state transformer: Technology for a smarter and resilient grid," *IEEE Industrial Electronics Magazine*, vol. 10, no. 3, pp. 29–42, 2016. DOI: 10.1109/MIE.2016.2589061.

[11] D. Li, T. Wang, W. Pan, X. Ding, and J. Gong, "A comprehensive review of improving power quality using active power filters," *Electric Power Systems Research*, vol. 199, p. 107 389, 2021, ISSN: 0378-7796. DOI: 10.1016/j.epsr.2021.107389.

[12] T. Dao and B. T. Phung, "Effects of voltage harmonic on losses and temperature rise in distribution transformers," English, *IET Generation, Transmission & Distribution*, vol. 12, no. 2, 347–354(7), 2018, ISSN: 1751-8687. DOI: 10.1049/iet-gtd.2017.0498.

[13] H. Akagi, E. Hirokazu Watanabe, and M. Aredes, *Instantaneous power theory and applications to power conditioning; 2nd ed.* Hoboken, NJ: Wiley-IEEE Press, 2017. [Online]. Available: https://cds.cern.ch/record/2259083.

[14] J. A. P. Lopes, C. L. Moreira, and A. G. Madureira, "Defining control strategies for microgrids islanded operation," *IEEE Transactions on Power Systems*, vol. 21, no. 2, pp. 916–924, 2006. DOI: 10.1109/TPWRS.2006.873018.

[15] J. M. Guerrero, M. Chandorkar, T.-L. Lee, and P. C. Loh, "Advanced control architectures for intelligent microgrids—part I: Decentralized and hierarchical control," *IEEE Transactions on Industrial Electronics*, vol. 60, no. 4, pp. 1254–1262, 2013. DOI: 10.1109/TIE.2012.2194969.

[16] E. Coelho, P. Cortizo, and P. Garcia, "Small-signal stability for parallel-connected inverters in stand-alone ac supply systems," *IEEE Transactions on Industry Applications*, vol. 38, no. 2, pp. 533–542, 2002. DOI: 10.1109/28.993176.

[17] Y. Wang, G. Yang, Y. Dong, Y. Cheng, and P. Shang, "The scale, structure and influencing factors of total carbon emissions from households in 30 provinces of china—based on the extended stirpat model," *Energies*, vol. 11, no. 5, 2018, ISSN: 1996-1073. DOI: 10.3390/en11051125. [Online]. Available: https://www.mdpi.com/1996-1073/11/5/1125.

[18] J. A. Sanguesa, V. Torres-Sanz, P. Garrido, F. J. Martinez, and J. M. Marquez-Barja, "A review on electric vehicles: Technologies and challenges," *Smart*

Cities, vol. 4, no. 1, pp. 372–404, 2021, ISSN: 2624-6511. DOI: 10.3390/smartcities4010022. [Online]. Available: https://www.mdpi.com/2624-6511/4/1/22.

[19] D. Divan and J. Sastry, "Controllable network transformers," in *2008 IEEE Power Electronics Specialists Conference*, 2008, pp. 2340–2345. DOI: 10.1109/PESC.2008.4592291.

[20] M. A. Shamshuddin, F. Rojas, R. Cardenas, J. Pereda, M. Diaz, and R. Kennel, "Solid state transformers: Concepts, classification, and control," *Energies*, vol. 13, no. 9, 2020, ISSN: 1996-1073. DOI: 10.3390/en13092319. [Online]. Available: https://www.mdpi.com/1996-1073/13/9/2319.

[21] C. Langpoklakpam, A.-C. Liu, K.-H. Chu, *et al.*, "Review of silicon carbide processing for power mosfet," *Crystals*, vol. 12, no. 2, 2022, ISSN: 2073-4352. DOI: 10.3390/cryst12020245. [Online]. Available: https://www.mdpi.com/2073-4352/12/2/245.

[22] S. Valedsaravi, A. El Aroudi, and L. Martínez-Salamero, "Review of solid-state transformer applications on electric vehicle DC ultra-fast charging station," *Energies*, vol. 15, no. 15, 2022. DOI: 10.3390/en15155602.

[23] IEEE, "IEEE recommended practice and requirements for harmonic control in electric power systems," *IEEE Std 519-2014 (Revision of IEEE Std 519-1992)*, pp. 1–29, 2014. DOI: 10.1109/IEEESTD.2014.6826459.

[24] Y. Wang, H. Liu, K. Yin, and Y. Yuan, "A Full-Tuned Filtering Method for Dynamic Tuning Passive Filter Power Electronics," *Journal of Control, Automation and Electrical Systems*, vol. 32, no. 6, pp. 1771–1781, Dec. 2021, ISSN: 2195-3899. DOI: 10.1007/s40313-021-00742-9.

[25] S. Valedsaravi, A. El Aroudi, and L. Martínez-Salamero, "Control of a PV-fed cascaded half-bridge multilevel inverter with shunt active power filter capabilities," *IFAC-PapersOnLine*, vol. 55, no. 12, pp. 37–42, 2022, 14th IFAC Workshop on Adaptive and Learning Control Systems ALCOS 2022. DOI: 10.1016/j.ifacol.2022.07.285.

[26] L. Czarnecki, "Instantaneous reactive power p-q theory and power properties of three-phase systems," *IEEE Transactions on Power Delivery*, vol. 21, no. 1, pp. 362–367, 2006. DOI: 10.1109/TPWRD.2005.852348.

[27] M. Aredes, L. Monteiro, and J. Mourente, "Control strategies for series and shunt active filters," in *2003 IEEE Bologna Power Tech Conference Proceedings,*, vol. 2, 2003, 6 pp. Vol.2–. DOI: 10.1109/PTC.2003.1304675.

[28] L. Czarnecki, "On some misinterpretations of the instantaneous reactive power p-q theory," *IEEE Transactions on Power Electronics*, vol. 19, no. 3, pp. 828–836, 2004. DOI: 10.1109/TPEL.2004.826500.

[29] A. Bitoleanu and M. Popescu, "Shunt active power filter overview on the reference current methods calculation and their implementation," in *2013 4th International Symposium on Electrical and Electronics Engineering (ISEEE)*, 2013, pp. 1–12. DOI: 10.1109/ISEEE.2013.6674384.

[30] M. Liserre, R. Teodorescu, and F. Blaabjerg, "Stability of photovoltaic and wind turbine grid-connected inverters for a large set of grid impedance values," *IEEE Transactions on Power Electronics*, vol. 21, no. 1, pp. 263–272, 2006. DOI: 10.1109/TPEL.2005.861185.

[31] M. Schiesser, S. Wasterlain, M. Marchesoni, and M. Carpita, "A simplified design strategy for multi-resonant current control of a grid-connected voltage source inverter with an LCL filter," *Energies*, vol. 11, no. 3, 2018, ISSN: 1996-1073. DOI: 10.3390/en11030609.

[32] M. Castilla, J. Miret, J. Matas, L. Garcia de Vicuna, and J. M. Guerrero, "Control design guidelines for single-phase grid-connected photovoltaic inverters with damped resonant harmonic compensators," *IEEE Transactions on Industrial Electronics*, vol. 56, no. 11, pp. 4492–4501, 2009. DOI: 10.1109/TIE.2009.2017820.

[33] P. Chittora, A. Singh, and K. Singh, "Design, analysis, and implementation of proportional-resonant filters for shunt compensation," *International Transactions on Electrical Energy Systems*, vol. 27, no. 10, e2388, 2017. DOI: 10.1002/etep.2388.

[34] S. Valedsaravi, A. E. Aroudi, J. A. Barrado-Rodrigo, M. Hamzeh, and L. Martínez-Salamero, "Multi-resonant Controller Design for a PV-Fed Multifunctional Grid-Connected Inverter in Presence of Unbalanced and Nonlinear Load," *Journal of Control, Automation and Electrical Systems*, vol. 34, no. 4, pp. 766–781, Aug. 2023, ISSN: 2195-3899. DOI: 10.1007/s40313-023-01007-3. [Online]. Available: https://doi.org/10.1007/s40313-023-01007-3.

[35] T. Wu, M. Misra, L. Lin, and C. Hsu, "An improved resonant frequency based systematic LCL filter design method for grid-connected inverter," *IEEE Transactions on Industrial Electronics*, vol. 64, no. 8, pp. 6412–6421, 2017. DOI: 10.1109/TIE.2017.2682004.

[36] F. Liu, S. Duan, F. Liu, B. Liu, and Y. Kang, "A variable step size inc mppt method for PV systems," *IEEE Transactions on Industrial Electronics*, vol. 55, no. 7, pp. 2622–2628, 2008. DOI: 10.1109/TIE.2008.920550.

[37] Y. Hoon, M. A. Mohd Radzi, M. A. A. Mohd Zainuri, and M. A. M. Zawawi, "Shunt active power filter: A review on phase synchronization control techniques," *Electronics*, vol. 8, no. 7, 2019. DOI: 10.3390/electronics8070791.

[38] L. Asiminoael, F. Blaabjerg, and S. Hansen, "Detection is key - harmonic detection methods for active power filter applications," *IEEE Industry Applications Magazine*, vol. 13, no. 4, pp. 22–33, 2007. DOI: 10.1109/MIA.2007.4283506.

[39] D. Zmood and D. Holmes, "Stationary frame current regulation of pwm inverters with zero steady-state error," *IEEE Transactions on Power Electronics*, vol. 18, no. 3, pp. 814–822, 2003. DOI: 10.1109/TPEL.2003.810852.

[40] L. A. Maccari Jr., D. M. Lima, G. G. Koch, and V. F. Montagner, "Robust Model Predictive Controller Applied to Three-Phase Grid-Connected LCL Filters," *Journal of Control, Automation and Electrical Systems*, vol. 31, no. 2, pp. 447–460, Apr. 2020, ISSN: 2195-3899. DOI: 10.1007/s40313-019-00546-y.

[41] G. V. Hollweg, P. J. D. de Oliveira Evald, E. Mattos, R. V. Tambara, and H. A. Gründling, "Feasibility Assessment of Adaptive Sliding Mode Controllers for Grid-Tied Inverters with LCL Filter," *Journal of Control, Automation and Electrical Systems*, Oct. 2021, ISSN: 2195-3899. DOI: 10.1007/s40313-021-00835-5.

[42] E. Twining and D. Holmes, "Grid current regulation of a three-phase voltage source inverter with an LCL input filter," *IEEE Transactions on Power Electronics*, vol. 18, no. 3, pp. 888–895, 2003. DOI: 10.1109/TPEL.2003.810838.

[43] A. Timbus, M. Liserre, R. Teodorescu, P. Rodriguez, and F. Blaabjerg, "Evaluation of current controllers for distributed power generation systems," *IEEE Transactions on Power Electronics*, vol. 24, no. 3, pp. 654–664, 2009. DOI: 10.1109/TPEL.2009.2012527.

[44] R. Bojoi, G. Griva, V. Bostan, M. Guerriero, F. Farina, and F. Profumo, "Current control strategy for power conditioners using sinusoidal signal integrators in synchronous reference frame," *IEEE Transactions on Power Electronics*, vol. 20, no. 6, pp. 1402–1412, 2005. DOI: 10.1109/TPEL.2005.857558.

[45] J. Dannehl, F. W. Fuchs, S. Hansen, and P. B. Thøgersen, "Investigation of active damping approaches for PI-based current control of grid-connected pulse width modulation converters with LCL filters," *IEEE Transactions on Industry Applications*, vol. 46, no. 4, pp. 1509–1517, 2010. DOI: 10.1109/TIA.2010.2049974.

[46] B. Henz Mossmann, L. F. Alves Pereira, and J. M. Gomes da Silva, "Tuning of Proportional-Resonant Controllers Combined with Phase-Lead Compensators Based on the Frequency Response," *Journal of Control, Automation and Electrical Systems*, vol. 32, no. 4, pp. 910–926, Aug. 2021, ISSN: 2195-3899. DOI: 10.1007/s40313-021-00728-7.

[47] T. Ye, N. Dai, C. Lam, M. Wong, and J. M. Guerrero, "Analysis, design, and implementation of a quasi-proportional-resonant controller for a multifunctional capacitive-coupling grid-connected inverter," *IEEE Transactions on Industry Applications*, vol. 52, no. 5, pp. 4269–4280, 2016. DOI: 10.1109/TIA.2016.2581152.

[48] A. Abazari, M. Ghazavi Dozein, H. Monsef, and B. Wu, "Wind turbine participation in micro-grid frequency control through self-tuning, adaptive fuzzy droop

in de-loaded area," *IET Smart Grid*, vol. 2, no. 2, pp. 301–308, 2019. DOI: 10.1049/iet-stg.2018.0095.

[49] A. Abazari, H. Monsef, and B. Wu, "Load frequency control by de-loaded wind farm using the optimal fuzzy-based pid droop controller," *IET Renewable Power Generation*, vol. 13, no. 1, pp. 180–190, 2019. DOI: 10.1049/iet-rpg.2018.5392.

[50] Y. Shi and R. Eberhart, "A modified particle swarm optimizer," in *1998 IEEE International Conference on Evolutionary Computation Proceedings. IEEE World Congress on Computational Intelligence (Cat. No.98TH8360)*, 1998, pp. 69–73. DOI: 10.1109/ICEC.1998.699146.

[51] D. Bratton and J. Kennedy, "Defining a standard for particle swarm optimization," in *2007 IEEE Swarm Intelligence Symposium*, 2007, pp. 120–127. DOI: 10.1109/SIS.2007.368035.

[52] S. Valedsaravi, A. El Aroudi, J. A. Barrado-Rodrigo, W. Issa, and L. Martínez-Salamero, "Control design and parameter tuning for islanded microgrids by combining different optimization algorithms," *Energies*, vol. 15, no. 10, 2022. DOI: 10.3390/en15103756.

[53] W. Bolton, *Instrumentation and Control Systems*. Elsevier Science, 2004, ISBN: 9780080470399. [Online]. Available: https://books.google.es/books?id=X-gADDWI-NIC.

[54] W. R. Issa, M. A. Abusara, and S. M. Sharkh, "Control of transient power during unintentional islanding of microgrids," *IEEE Transactions on Power Electronics*, vol. 30, no. 8, pp. 4573–4584, 2015. DOI: 10.1109/TPEL.2014.2359792.

[55] W. R. Issa, A. H. E. Khateb, M. A. Abusara, and T. K. Mallick, "Control strategy for uninterrupted microgrid mode transfer during unintentional islanding scenarios," *IEEE Transactions on Industrial Electronics*, vol. 65, no. 6, pp. 4831–4839, 2018. DOI: 10.1109/TIE.2017.2772199.

[56] R. Al Badwawi, W. R. Issa, T. K. Mallick, and M. Abusara, "Supervisory control for power management of an islanded ac microgrid using a frequency signalling-based fuzzy logic controller," *IEEE Transactions on Sustainable Energy*, vol. 10, no. 1, pp. 94–104, 2019. DOI: 10.1109/TSTE.2018.2825655.

[57] W. R. Issa, M. A. Abusara, and S. M. Sharkh, "Impedance interaction between islanded parallel voltage source inverters and the distribution network," in *7th IET International Conference on Power Electronics, Machines and Drives (PEMD 2014)*, 2014, pp. 1–6. DOI: 10.1049/cp.2014.0315.

[58] H. Han, X. Hou, J. Yang, J. Wu, M. Su, and J. M. Guerrero, "Review of power sharing control strategies for islanding operation of ac microgrids," *IEEE Transactions on Smart Grid*, vol. 7, no. 1, pp. 200–215, 2016. DOI: 10.1109/TSG.2015.2434849.

[59] W. Huang, Z. Shuai, X. Shen, Y. Li, and Z. J. Shen, "Dynamical reconfigurable master–slave control architecture (drmsca) for voltage regulation in islanded microgrids," *IEEE Transactions on Power Electronics*, vol. 37, no. 1, pp. 249–263, 2022. DOI: 10.1109/TPEL.2021.3099482.

[60] X. Sun, Y.-S. Lee, and D. Xu, "Modeling, analysis, and implementation of parallel multi-inverter systems with instantaneous average-current-sharing scheme," *IEEE Transactions on Power Electronics*, vol. 18, no. 3, pp. 844–856, 2003. DOI: 10.1109/TPEL.2003.810867.

[61] M. A. Hossain, H. R. Pota, W. Issa, and M. J. Hossain, "Overview of ac microgrid controls with inverter-interfaced generations," *Energies*, vol. 10, no. 9, 2017, ISSN: 1996-1073. DOI: 10.3390/en10091300.

[62] J. Rocabert, A. Luna, F. Blaabjerg, and P. Rodríguez, "Control of power converters in ac microgrids," *IEEE Transactions on Power Electronics*, vol. 27, no. 11, pp. 4734–4749, 2012. DOI: 10.1109/TPEL.2012.2199334.

[63] T. Dragičević, X. Lu, J. C. Vasquez, and J. M. Guerrero, "Dc microgrids—part i: A review of control strategies and stabilization techniques," *IEEE Transactions on Power Electronics*, vol. 31, no. 7, pp. 4876–4891, 2016. DOI: 10.1109/TPEL.2015.2478859.

[64] M. Zolfaghari, G. B. Gharehpetian, M. Shafie-khah, and J. P. Catalão, "Comprehensive review on the strategies for controlling the interconnection of ac and dc microgrids," *International Journal of Electrical Power & Energy Systems*, vol. 136, p. 107 742, 2022, ISSN: 0142-0615. DOI: 10.1016/j.ijepes.2021.107742.

[65] R.-F. Yuan, Q. Ai, and X. He, "Research on dynamic load modelling based on power quality monitoring system," *IET Generation, Transmission & Distribution*, vol. 7, no. 1, pp. 46–51, 2013. DOI: 10.1049/iet-gtd.2012.0365. eprint: https://ietresearch.onlinelibrary.wiley.com/doi/pdf/10.1049/iet-gtd.2012.0365.

[66] W. Issa, F. Al-naemi, G. Konstantopoulos, S. Sharkh, and M. Abusara, "Stability analysis and control of a microgrid against circulating power between parallel inverters," *Energy Procedia*, vol. 157, pp. 1061–1070, 2019, Technologies and Materials for Renewable Energy, Environment and Sustainability (TMREES), ISSN: 1876-6102. DOI: 10.1016/j.egypro.2018.11.273.

[67] N. Pogaku, M. Prodanovic, and T. C. Green, "Modeling, analysis and testing of autonomous operation of an inverter-based microgrid," *IEEE Transactions on Power Electronics*, vol. 22, no. 2, pp. 613–625, 2007. DOI: 10.1109/TPEL.2006.890003.

[68] W. Issa, S. Sharkh, and M. Abusara, "Hybrid generators-based ac microgrid performance assessment in island mode," *IET Power Electronics*, vol. 12, no. 8, pp. 1973–1980, 2019. DOI: 10.1049/iet-pel.2018.5295. eprint: https://ietresearch.onlinelibrary.wiley.com/doi/pdf/10.1049/iet-pel.2018.5295.

[69] C. K. Sao and P. W. Lehn, "Control and power management of converter fed microgrids," *IEEE Transactions on Power Systems*, vol. 23, no. 3, pp. 1088–1098, 2008. DOI: 10.1109/TPWRS.2008.922232.

[70] Q.-C. Zhong and T. Hornik, "Cascaded current–voltage control to improve the power quality for a grid-connected inverter with a local load," *IEEE Transactions on Industrial Electronics*, vol. 60, no. 4, pp. 1344–1355, 2013. DOI: 10.1109/TIE.2012.2187415.

[71] W. Bolton, *Instrumentation and Control Systems*, third. Elsevier Ltd, 2021.

[72] S. Eberlein and K. Rudion, "Small-signal stability modelling, sensitivity analysis and optimization of droop controlled inverters in lv microgrids," *International Journal of Electrical Power & Energy Systems*, vol. 125, p. 106 404, 2021, ISSN: 0142-0615. DOI: 10.1016/j.ijepes.2020.106404.

[73] A. Eisenmann, T. Streubel, and K. Rudion, "Power quality mitigation via smart demand-side management based on a genetic algorithm," *Energies*, vol. 15, no. 4,

2022, ISSN: 1996-1073. DOI: 10.3390/en15041492. [Online]. Available: https://www.mdpi.com/1996-1073/15/4/1492.

[74] M. A. S. Hassan, U. Assad, U. Farooq, *et al.*, "Dynamic price-based demand response through linear regression for microgrids with renewable energy resources," *Energies*, vol. 15, no. 4, 2022, ISSN: 1996-1073. DOI: 10.3390/en15041385. [Online]. Available: https://www.mdpi.com/1996-1073/15/4/1385.

[75] M. A. Hassan and M. A. Abido, "Optimal design of microgrids in autonomous and grid-connected modes using particle swarm optimization," *IEEE Transactions on Power Electronics*, vol. 26, no. 3, pp. 755–769, 2011. DOI: 10.1109/TPEL.2010.2100101.

[76] I. Chung, W. Liu, D. A. Cartes, E. G. Collins, and S. Moon, "Control methods of inverter-interfaced distributed generators in a microgrid system," *IEEE Transactions on Industry Applications*, vol. 46, no. 3, pp. 1078–1088, 2010. DOI: 10.1109/TIA.2010.2044970.

[77] A. Rosini, A. Labella, A. Bonfiglio, R. Procopio, and J. M. Guerrero, "A review of reactive power sharing control techniques for islanded microgrids," *Renewable and Sustainable Energy Reviews*, vol. 141, p. 110 745, 2021, ISSN: 1364-0321. DOI: https://doi.org/10.1016/j.rser.2021.110745. [Online]. Available: https://www.sciencedirect.com/science/article/pii/S1364032121000411.

[78] H. Bevrani, F. Habibi, P. Babahajyani, M. Watanabe, and Y. Mitani, "Intelligent frequency control in an ac microgrid: Online pso-based fuzzy tuning approach," *IEEE Transactions on Smart Grid*, vol. 3, no. 4, pp. 1935–1944, 2012. DOI: 10.1109/TSG.2012.2196806.

[79] T. A. Jumani, M. W. Mustafa, M. Md Rasid, N. H. Mirjat, Z. H. Leghari, and M. S. Saeed, "Optimal voltage and frequency control of an islanded microgrid using grasshopper optimization algorithm," *Energies*, vol. 11, no. 11, 2018, ISSN: 1996-1073. DOI: 10.3390/en11113191.

[80] N. K. Vemula and S. K. Parida, "Enhancement of small signal stability in inverter-dominated microgrid with optimal internal model controller," *International Transactions on Electrical Energy Systems*, vol. 30, no. 8, e12471, 2020. DOI: 10.1002/2050-7038.12471. eprint: https://onlinelibrary.wiley.com/doi/pdf/10.1002/2050-7038.12471.

[81] O. M. Salim, A. Aboraya, and S. I. Arafa, "Cascaded controller for a standalone microgrid-connected inverter based on triple-action controller and particle swarm optimisation," *IET Generation, Transmission & Distribution*, vol. 14, no. 17, pp. 3389–3399, 2020. DOI: 10.1049/iet-gtd.2019.1641. eprint: https://ietresearch.onlinelibrary.wiley.com/doi/pdf/10.1049/iet-gtd.2019.1641.

[82] S. Shokoohi, S. Golshannavaz, R. Khezri, and H. Bevrani, "Intelligent secondary control in smart microgrids: An on-line approach for islanded operations," *Optimization and Engineering*, vol. 19, no. 4, pp. 917–936, 2018, ISSN: 1573-2924. DOI: 10.1007/s11081-018-9382-9.

[83] H. Wang, G. Zeng, Y. Dai, D. Bi, J. Sun, and X. Xie, "Design of a fractional order frequency pid controller for an islanded microgrid: A multi-objective extremal optimization method," *Energies*, vol. 10, no. 10, 2017, ISSN: 1996-1073. DOI: 10.3390/en10101502.

[84] A. Abraham and S. Das, *Computational Intelligence in Power Engineering* (Studies in Computational Intelligence). Springer Berlin Heidelberg, 2012, ISBN: 978-3-642-26509-9.

[85] A. Yazdani and R. Iravani, "Space phasors and two-dimensional frames," in *Voltage-Sourced Converters in Power Systems: Modeling, Control, and Applications*. 2010, pp. 69–114. DOI: 10.1002/9780470551578.ch4.

[86] Y. Han, H. Li, P. Shen, E. A. A. Coelho, and J. M. Guerrero, "Review of active and reactive power sharing strategies in hierarchical controlled microgrids," *IEEE Transactions on Power Electronics*, vol. 32, no. 3, pp. 2427–2451, 2017. DOI: 10.1109/TPEL.2016.2569597.

[87] U. Borup, F. Blaabjerg, and P. Enjeti, "Sharing of nonlinear load in parallel-connected three-phase converters," *IEEE Transactions on Industry Applications*, vol. 37, no. 6, pp. 1817–1823, 2001. DOI: 10.1109/28.968196.

[88] S. Leitner, M. Yazdanian, A. Mehrizi-Sani, and A. Muetze, "Small-signal stability analysis of an inverter-based microgrid with internal model-based controllers," *IEEE Transactions on Smart Grid*, vol. 9, no. 5, pp. 5393–5402, 2018. DOI: 10.1109/TSG.2017.2688481.

[89] K. Ogata, *Modern Control Engineering* (Instrumentation and controls series). Prentice Hall, 2010, ISBN: 9780136156734. [Online]. Available: https://books.google.es/books?id=Wu5GpNAelzkC.

[90] J. He, X. Wu, X. Wu, Y. Xu, and J. M. Guerrero, "Small-signal stability analysis and optimal parameters design of microgrid clusters," *IEEE Access*, vol. 7, pp. 36 896–36 909, 2019. DOI: 10.1109/ACCESS.2019.2900728.

[91] S. G. M. Monfared and J. Guerrero, "A new synchronous reference frame-based method for single-phase shunt active power filters," *Journal of Power Electronics*, vol. 13, no. 4, pp. 692–700, 2013. DOI: doi.org/10.6113/JPE.2013.13.4.692.

[92] E. Koessler and A. Almomani, "Hybrid particle swarm optimization and pattern search algorithm," *Optimization and Engineering*, vol. 22, no. 3, pp. 1539–1555, 2021, ISSN: 1573-2924. DOI: 10.1007/s11081-020-09534-7.

[93] I. A. Latiff and M. Tokhi, "Improving particle swarm optimization convergence with spread and momentum factors," 2011.

[94] M. Sakawa, *Genetic algorithms and fuzzy multiobjective optimization*. Springer, 2002, vol. 14.

[95] N. Deb, R. Singh, R. R. Brooks, and K. Bai, "A review of extremely fast charging stations for electric vehicles," *Energies*, vol. 14, no. 22, 2021, ISSN: 1996-1073. DOI: 10.3390/en14227566. [Online]. Available: https://www.mdpi.com/1996-1073/14/22/7566.

[96] L. Zheng, A. Marellapudi, V. R. Chowdhury, *et al.*, "Solid-state transformer and hybrid transformer with integrated energy storage in active distribution grids: Technical and economic comparison, dispatch, and control," *IEEE Journal of Emerging and Selected Topics in Power Electronics*, pp. 1–1, 2022. DOI: 10.1109/JESTPE.2022.3144361.

[97] C. Suthaputchakun, Z. Sun, and M. Dianati, "Applications of vehicular communications for reducing fuel consumption and co2 emission: The state of the art and research challenges," *IEEE Communications Magazine*, vol. 50, no. 12, pp. 108–115, 2012. DOI: 10.1109/MCOM.2012.6384459.

[98] C. C. Chan, "The state of the art of electric, hybrid, and fuel cell vehicles," *Proceedings of the IEEE*, vol. 95, no. 4, pp. 704–718, 2007. DOI: 10.1109/JPROC.2007.892489.

[99] S. Srdic and S. Lukic, "Toward extreme fast charging: Challenges and opportunities in directly connecting to medium-voltage line," *IEEE Electrification Magazine*, vol. 7, no. 1, pp. 22–31, 2019. DOI: 10.1109/MELE.2018.2889547.

[100] R. Collin, Y. Miao, A. Yokochi, P. Enjeti, and A. von Jouanne, "Advanced electric vehicle fast-charging technologies," *Energies*, vol. 12, no. 10, 2019, ISSN: 1996-1073. DOI: 10.3390/en12101839. [Online]. Available: https://www.mdpi.com/1996-1073/12/10/1839.

[101] J. Feng, W. Q. Chu, Z. Zhang, and Z. Q. Zhu, "Power electronic transformer-based railway traction systems: Challenges and opportunities," *IEEE Journal of Emerging and Selected Topics in Power Electronics*, vol. 5, no. 3, pp. 1237–1253, 2017. DOI: 10.1109/JESTPE.2017.2685464.

[102] D. Ronanki and S. S. Williamson, "Modular multilevel converters for transportation electrification: Challenges and opportunities," *IEEE Transactions on Transportation Electrification*, vol. 4, no. 2, pp. 399–407, 2018. DOI: 10.1109/TTE.2018.2792330.

[103] A. Khaligh and M. D'Antonio, "Global trends in high-power on-board chargers for electric vehicles," *IEEE Transactions on Vehicular Technology*, vol. 68, no. 4, pp. 3306–3324, 2019. DOI: 10.1109/TVT.2019.2897050.

[104] M. Keyser, A. Pesaran, Q. Li, *et al.*, "Enabling fast charging – battery thermal considerations," *Journal of Power Sources*, vol. 367, pp. 228–236, 2017, ISSN: 0378-7753. DOI: 10.1016/j.jpowsour.2017.07.009.

[105] T. Waldmann, B.-I. Hogg, and M. Wohlfahrt-Mehrens, "Li plating as unwanted side reaction in commercial li-ion cells – a review," *Journal of Power Sources*, vol. 384, pp. 107–124, 2018, ISSN: 0378-7753. DOI: 10.1016/j.jpowsour.2018.02.063. [Online]. Available: https://www.sciencedirect.com/science/article/pii/S0378775318301848.

[106] X. Ding, W. Zhang, S. Wei, and Z. Wang, "Optimization of an energy storage system for electric bus fast-charging station," *Energies*, vol. 14, no. 14, 2021, ISSN: 1996-1073. DOI: 10.3390/en14144143. [Online]. Available: https://www.mdpi.com/1996-1073/14/14/4143.

[107] A. Meintz, J. Zhang, R. Vijayagopal, *et al.*, "Enabling fast charging – vehicle considerations," *Journal of Power Sources*, vol. 367, pp. 216–227, 2017, ISSN: 0378-7753. DOI: 10.1016/j.jpowsour.2017.07.093.

[108] M. Kang, P. Enjeti, and I. Pitel, "Analysis and design of electronic transformers for electric power distribution system," *IEEE Transactions on Power Electronics*, vol. 14, no. 6, pp. 1133–1141, 1999. DOI: 10.1109/63.803407.

[109] D. Das, D. M. Divan, and R. G. Harley, "Power flow control in networks using controllable network transformers," *IEEE Transactions on Power Electronics*, vol. 25, no. 7, pp. 1753–1760, 2010. DOI: 10.1109/TPEL.2010.2042076.

[110] "Ieee standard glossary of stationary battery terminology," *IEEE Std 1881-2016*, pp. 1–42, 2016. DOI: 10.1109/IEEESTD.2016.7552407.

[111] M. Li, M. Feng, D. Luo, and Z. Chen, "Fast charging li-ion batteries for a new era of electric vehicles," *Cell Reports Physical Science*, vol. 1, no. 10, p. 100 212, 2020, ISSN: 2666-3864. DOI: 10.1016/j.xcrp.2020.100212. [Online].

Available: https://www.sciencedirect.com/science/article/pii/S2666386420302277.

[112] R. Chandrasekaran, "Quantification of bottlenecks to fast charging of lithium-ion-insertion cells for electric vehicles," *Journal of Power Sources*, vol. 271, pp. 622–632, 2014, ISSN: 0378-7753. DOI: 10.1016/j.jpowsour.2014.07.106. [Online]. Available: https://www.sciencedirect.com/science/article/pii/S0378775314011604.

[113] Y. Parvini, A. Vahidi, and S. A. Fayazi, "Heuristic versus optimal charging of supercapacitors, lithium-ion, and lead-acid batteries: An efficiency point of view," *IEEE Transactions on Control Systems Technology*, vol. 26, no. 1, pp. 167–180, 2018. DOI: 10.1109/TCST.2017.2665540.

[114] M. Hannan, M. Lipu, A. Hussain, and A. Mohamed, "A review of lithium-ion battery state of charge estimation and management system in electric vehicle applications: Challenges and recommendations," *Renewable and Sustainable Energy Reviews*, vol. 78, pp. 834–854, 2017, ISSN: 1364-0321. DOI: 10.1016/j.rser.2017.05.001. [Online]. Available: https://www.sciencedirect.com/science/article/pii/S1364032117306275.

[115] Z. Wang, G. Feng, D. Zhen, F. Gu, and A. Ball, "A review on online state of charge and state of health estimation for lithium-ion batteries in electric vehicles," *Energy Reports*, vol. 7, pp. 5141–5161, 2021, ISSN: 2352-4847. DOI: 10.1016/j.egyr.2021.08.113. [Online]. Available: https://www.sciencedirect.com/science/article/pii/S2352484721007150.

[116] Y. Gao, X. Zhang, Q. Cheng, B. Guo, and J. Yang, "Classification and review of the charging strategies for commercial lithium-ion batteries," *IEEE Access*, vol. 7, pp. 43 511–43 524, 2019. DOI: 10.1109/ACCESS.2019.2906117.

[117] B. Arabsalmanabadi, N. Tashakor, A. Javadi, and K. Al-Haddad, "Charging techniques in lithium-ion battery charger: Review and new solution," in *IECON 2018 - 44th Annual Conference of the IEEE Industrial Electronics Society*, 2018, pp. 5731–5738. DOI: 10.1109/IECON.2018.8591173.

[118] A. Al-Haj Hussein and I. Batarseh, "A review of charging algorithms for nickel and lithium battery chargers," *IEEE Transactions on Vehicular Technology*, vol. 60, no. 3, pp. 830–838, 2011. DOI: 10.1109/TVT.2011.2106527.

[119] X. Qu, H. Han, S.-C. Wong, C. K. Tse, and W. Chen, "Hybrid ipt topologies with constant current or constant voltage output for battery charging applications," *IEEE Transactions on Power Electronics*, vol. 30, no. 11, pp. 6329–6337, 2015. DOI: 10.1109/TPEL.2015.2396471.

[120] V.-B. Vu, D.-H. Tran, and W. Choi, "Implementation of the constant current and constant voltage charge of inductive power transfer systems with the double-sided <italic>lcc</italic> compensation topology for electric vehicle battery charge applications," *IEEE Transactions on Power Electronics*, vol. 33, no. 9, pp. 7398–7410, 2018. DOI: 10.1109/TPEL.2017.2766605.

[121] J. M. Amanor-Boadu, A. Guiseppi-Elie, and E. Sánchez-Sinencio, "The impact of pulse charging parameters on the life cycle of lithium-ion polymer batteries," *Energies*, vol. 11, no. 8, 2018, ISSN: 1996-1073. DOI: 10.3390/en11082162. [Online]. Available: https://www.mdpi.com/1996-1073/11/8/2162.

[122] M. Etezadi-Amoli, K. Choma, and J. Stefani, "Rapid-charge electric-vehicle stations," *IEEE Transactions on Power Delivery*, vol. 25, no. 3, pp. 1883–1887, 2010. DOI: 10.1109/TPWRD.2010.2047874.

[123] A. Jokar, B. Rajabloo, M. Désilets, and M. Lacroix, "Review of simplified pseudo-two-dimensional models of lithium-ion batteries," *Journal of Power Sources*, vol. 327, pp. 44–55, 2016, ISSN: 0378-7753. DOI: 10.1016/j.jpowsour.2016.07.036. [Online]. Available: https://www.sciencedirect.com/science/article/pii/S0378775316308916.

[124] L. Lam, P. Bauer, and E. Kelder, "A practical circuit-based model for li-ion battery cells in electric vehicle applications," in *2011 IEEE 33rd International Telecommunications Energy Conference (INTELEC)*, 2011, pp. 1–9. DOI: 10.1109/INTLEC.2011.6099803.

[125] L. Kang, X. Zhao, and J. Ma, "A new neural network model for the state-of-charge estimation in the battery degradation process," *Applied Energy*, vol. 121, pp. 20–27, 2014, ISSN: 0306-2619. DOI: 10.1016/j.apenergy.2014.01.066. [Online]. Available: https://www.sciencedirect.com/science/article/pii/S0306261914000956.

[126] Z. Geng, S. Wang, M. J. Lacey, D. Brandell, and T. Thiringer, "Bridging physics-based and equivalent circuit models for lithium-ion batteries," *Electrochimica Acta*, vol. 372, p. 137 829, 2021, ISSN: 0013-4686. DOI: 10.1016/j.electacta.2021.137829. [Online]. Available: https://www.sciencedirect.com/science/article/pii/S0013468621001183.

[127] M. Doyle, T. F. Fuller, and J. Newman, "Modeling of galvanostatic charge and discharge of the lithium/polymer/insertion cell," *Journal of The Electrochemical*

Society, vol. 140, no. 6, pp. 1526–1533, 1993. DOI: 10.1149/1.2221597. [Online]. Available: https://doi.org/10.1149/1.2221597.

[128] J. Li, K. Adewuyi, N. Lotfi, R. Landers, and J. Park, "A single particle model with chemical/mechanical degradation physics for lithium ion battery state of health (soh) estimation," *Applied Energy*, vol. 212, pp. 1178–1190, 2018, ISSN: 0306-2619. DOI: 10.1016/j.apenergy.2018.01.011.

[129] R. Xiong, J. Cao, Q. Yu, H. He, and F. Sun, "Critical review on the battery state of charge estimation methods for electric vehicles," *IEEE Access*, vol. 6, pp. 1832–1843, 2018. DOI: 10.1109/ACCESS.2017.2780258.

[130] V. Sangwan, A. Sharma, R. Kumar, and A. K. Rathore, "Equivalent circuit model parameters estimation of li-ion battery: C-rate, soc and temperature effects," in *2016 IEEE International Conference on Power Electronics, Drives and Energy Systems (PEDES)*, 2016, pp. 1–6. DOI: 10.1109/PEDES.2016.7914369.

[131] I. Husain, *Electric and hybrid vehicles: design fundamentals*, 2nd. CRC press, 2011.

[132] H. A. Gabbar, A. M. Othman, and M. R. Abdussami, "Review of battery management systems (bms) development and industrial standards," *Technologies*, vol. 9, no. 2, 2021, ISSN: 2227-7080. DOI: 10.3390/technologies9020028. [Online]. Available: https://www.mdpi.com/2227-7080/9/2/28.

[133] M. Nassary, M. Orabi, M. Ghoneima, and M. K. El-Nemr, "Single-phase isolated bidirectional ac-dc battery charger for electric vehicle – review," in *2019 International Conference on Innovative Trends in Computer Engineering (ITCE)*, 2019, pp. 581–586. DOI: 10.1109/ITCE.2019.8646528.

[134] B. Lunz and D. Sauer, "17 - electric road vehicle battery charging systems and infrastructure," in *Advances in Battery Technologies for Electric Vehicles*, ser. Woodhead Publishing Series in Energy, B. Scrosati, J. Garche, and W. Tillmetz, Eds., Woodhead Publishing, 2015, pp. 445–467, ISBN: 978-1-78242-377-5. DOI: 10.1016/B978-1-78242-377-5.00017-0.

[135] IEC, *Plugs, socket-outlets, vehicle connectors and vehicle inlets - conductive charging of electric vehicles*. International Electrotechnical Commission, 2014.

[136] IEC, *Plugs, socket-outlets, vehicle connectors and vehicle inlets - conductive charging of electric vehicles*. International Electrotechnical Commission, 2016.

[137] IEC, *Plugs, socket-outlets, vehicle connectors and vehicle inlets - conductive charging of electric vehicles - Part 1: General requirements*. International Electrotechnical Commission, 2022.

[138] M. Nassary, M. Orabi, and M. Ghoneima, "Discussion of single-stage isolated unidirectional ac-dc on-board battery charger for electric vehicle," in *2018 IEEE 4th Southern Power Electronics Conference (SPEC)*, 2018, pp. 1–7. DOI: 10.1109/SPEC.2018.8635919.

[139] S. Rivera, S. Kouro, S. Vazquez, S. M. Goetz, R. Lizana, and E. Romero-Cadaval, "Electric vehicle charging infrastructure: From grid to battery," *IEEE Industrial Electronics Magazine*, vol. 15, no. 2, pp. 37–51, 2021. DOI: 10.1109/MIE.2020.3039039.

[140] B. Singh, B. Singh, A. Chandra, K. Al-Haddad, A. Pandey, and D. Kothari, "A review of three-phase improved power quality ac-dc converters," *IEEE Transactions on Industrial Electronics*, vol. 51, no. 3, pp. 641–660, 2004. DOI: 10.1109/TIE.2004.825341.

[141] F. Musavi, M. Edington, W. Eberle, and W. G. Dunford, "Evaluation and efficiency comparison of front end ac-dc plug-in hybrid charger topologies," *IEEE Transactions on Smart Grid*, vol. 3, no. 1, pp. 413–421, 2012. DOI: 10.1109/TSG.2011.2166413.

[142] F. Musavi, W. Eberle, and W. G. Dunford, "A high-performance single-phase bridgeless interleaved pfc converter for plug-in hybrid electric vehicle battery chargers," *IEEE Transactions on Industry Applications*, vol. 47, no. 4, pp. 1833–1843, 2011. DOI: 10.1109/TIA.2011.2156753.

[143] M. Yilmaz and P. T. Krein, "Review of battery charger topologies, charging power levels, and infrastructure for plug-in electric and hybrid vehicles," *IEEE Transactions on Power Electronics*, vol. 28, no. 5, pp. 2151–2169, 2013. DOI: 10.1109/TPEL.2012.2212917.

[144] M. A. Hannan, M. M. Hoque, A. Hussain, Y. Yusof, and P. J. Ker, "State-of-the-art and energy management system of lithium-ion batteries in electric vehicle applications: Issues and recommendations," *IEEE Access*, vol. 6, pp. 19 362–19 378, 2018. DOI: 10.1109/ACCESS.2018.2817655.

[145] S. Manzetti and F. Mariasiu, "Electric vehicle battery technologies: From present state to future systems," *Renewable and Sustainable Energy Reviews*, vol. 51, pp. 1004–1012, 2015, ISSN: 1364-0321. DOI: 10.1016/j.rser.2015.07.010. [Online]. Available: https://www.sciencedirect.com/science/article/pii/S1364032115006577.

[146] A. Mahmoudzadeh Andwari, A. Pesiridis, S. Rajoo, R. Martinez-Botas, and V. Esfahanian, "A review of battery electric vehicle technology and readiness levels," *Renewable and Sustainable Energy Reviews*, vol. 78, pp. 414–430, 2017, ISSN: 1364-0321. DOI: 10.1016/j.rser.2017.03.138.

[147] "Vehicle manufacturer, tesla, inc.," (accessed on 22/02/2022). eprint: Availableonline:https://www.tesla.com/.

[148] "Vehicle manufacturer, volkswagen group," (accessed on 22/02/2022). eprint: Availableonline:https://www.volkswagen.es/es.html.

[149] "Vehicle manufacturer, groupe renault," (accessed on 22/02/2022). eprint: Availableonline:https://www.renault.es/.

[150] M. Weiss, R. Ruess, J. Kasnatscheew, *et al.*, "Fast charging of lithium-ion batteries: A review of materials aspects," *Advanced Energy Materials*, vol. 11, no. 33, p. 2 101 126, 2021. DOI: 10.1002/aenm.202101126.

[151] D. Aggeler, F. Canales, H Zelaya-De La Parra, A. Coccia, N. Butcher, and O. Apeldoorn, "Ultra-fast dc-charge infrastructures for ev-mobility and future smart grids," in *2010 IEEE PES Innovative Smart Grid Technologies Conference Europe (ISGT Europe)*, 2010, pp. 1–8. DOI: 10.1109/ISGTEUROPE.2010.5638899.

[152] S. Vadi, R. Bayindir, A. M. Colak, and E. Hossain, "A review on communication standards and charging topologies of v2g and v2h operation strategies," *Energies*, vol. 12, no. 19, 2019, ISSN: 1996-1073. DOI: 10.3390/en12193748. [Online]. Available: https://www.mdpi.com/1996-1073/12/19/3748.

[153] A. Sharma and S. Sharma, "Review of power electronics in vehicle-to-grid systems," *Journal of Energy Storage*, vol. 21, pp. 337–361, 2019, ISSN: 2352-152X. DOI: 10.1016/j.est.2018.11.022. [Online]. Available: https://www.sciencedirect.com/science/article/pii/S2352152X1830481X.

[154] H. Tu, H. Feng, S. Srdic, and S. Lukic, "Extreme fast charging of electric vehicles: A technology overview," *IEEE Transactions on Transportation Electrification*, vol. 5, no. 4, pp. 861–878, 2019. DOI: 10.1109/TTE.2019.2958709.

[155] S. Rivera, B. Wu, S. Kouro, V. Yaramasu, and J. Wang, "Electric vehicle charging station using a neutral point clamped converter with bipolar dc bus," *IEEE Transactions on Industrial Electronics*, vol. 62, no. 4, pp. 1999–2009, 2015. DOI: 10.1109/TIE.2014.2348937.

[156] C. Srivastava and M. Tripathy, "Dc microgrid protection issues and schemes: A critical review," *Renewable and Sustainable Energy Reviews*, vol. 151, p. 111 546, 2021, ISSN: 1364-0321. DOI: 10.1016/j.rser.2021.111546. [Online]. Available: https://www.sciencedirect.com/science/article/pii/S1364032121008248.

[157] D. Jayamaha, N. Lidula, and A. Rajapakse, "Protection and grounding methods in dc microgrids: Comprehensive review and analysis," *Renewable and Sustainable Energy Reviews*, vol. 120, p. 109 631, 2020, ISSN: 1364-0321. DOI: 10.1016/j.rser.2019.109631. [Online]. Available: https://www.sciencedirect.com/science/article/pii/S136403211930838X.

[158] P. K. Maroti, S. Padmanaban, M. S. Bhaskar, V. K. Ramachandaramurthy, and F. Blaabjerg, "The state-of-the-art of power electronics converters configurations in electric vehicle technologies," *Power Electronic Devices and Components*, vol. 1, p. 100 001, 2022, ISSN: 2772-3704. DOI: 10.1016/j.pedc.2021.100001. [Online]. Available: https://www.sciencedirect.com/science/article/pii/S2772370421000018.

[159] J. E. Huber and J. W. Kolar, "Applicability of solid-state transformers in today's and future distribution grids," *IEEE Transactions on Smart Grid*, vol. 10, no. 1, pp. 317–326, 2019. DOI: 10.1109/TSG.2017.2738610.

[160] C. Zhao, D. Dujic, A. Mester, *et al.*, "Power electronic traction transformer—medium voltage prototype," *IEEE Transactions on Industrial Electronics*, vol. 61, no. 7, pp. 3257–3268, 2014. DOI: 10.1109/TIE.2013.2278960.

[161] M. Nassary, M. Orabi, and A. El Aroudi, "Single-loop control scheme for electrolytic capacitor-less ac–dc rectifiers with pfc in continuous conduction mode," *Electronics Letters*, vol. 56, no. 10, pp. 506–508, 2020. DOI: 10.1049/el.2020.0023. [Online]. Available: https://ietresearch.onlinelibrary.wiley.com/doi/abs/10.1049/el.2020.0023.

[162] W.-C. Lee, T.-K. Lee, and D.-S. Hyun, "Comparison of single-sensor current control in the dc link for three-phase voltage-source pwm converters," *IEEE Transactions on Industrial Electronics*, vol. 48, no. 3, pp. 491–505, 2001. DOI: 10.1109/41.925576.

[163] D. Graovac and V. Katic, "Online control of current-source-type active rectifier using transfer function approach," *IEEE Transactions on Industrial Electronics*, vol. 48, no. 3, pp. 526–535, 2001. DOI: 10.1109/41.925579.

[164] M. Singh, V. Khadkikar, A. Chandra, and R. K. Varma, "Grid interconnection of renewable energy sources at the distribution level with power-quality improvement features," *IEEE Transactions on Power Delivery*, vol. 26, no. 1, pp. 307–315, 2011. DOI: 10.1109/TPWRD.2010.2081384.

[165] M. Nassary, E. Vidal-Idiarte, and J. Calvente, "Analysis of non-minimum phase system for ac/dc battery charger power factor correction converter," *Applied Sciences*, vol. 12, no. 2, 2022, ISSN: 2076-3417. DOI: 10.3390/app12020868. [Online]. Available: https://www.mdpi.com/2076-3417/12/2/868.

[166] M. Carpita, M. Marchesoni, M. Pellerin, and D. Moser, "Multilevel converter for traction applications: Small-scale prototype tests results," *IEEE Transactions on Industrial Electronics*, vol. 55, no. 5, pp. 2203–2212, 2008. DOI: 10.1109/TIE.2008.918645.

[167] B. Singh, S. Gairola, B. N. Singh, A. Chandra, and K. Al-Haddad, "Multipulse ac–dc converters for improving power quality: A review," *IEEE Transactions on Power Electronics*, vol. 23, no. 1, pp. 260–281, 2008. DOI: 10.1109/TPEL.2007.911880.

[168] S. Chen, W. Yu, and D. Meyer, "Design and implementation of forced air-cooled, 140khz, 20kw sic mosfet based vienna pfc," in *2019 IEEE Applied Power Electronics Conference and Exposition (APEC)*, 2019, pp. 1196–1203. DOI: 10.1109/APEC.2019.8721979.

[169] T. Friedli, M. Hartmann, and J. W. Kolar, "The essence of three-phase pfc rectifier systems—part ii," *IEEE Transactions on Power Electronics*, vol. 29, no. 2, pp. 543–560, 2014. DOI: 10.1109/TPEL.2013.2258472.

[170] B. Singh, B. Singh, A. Chandra, K. Al-Haddad, A. Pandey, and D. Kothari, "A review of single-phase improved power quality ac-dc converters," *IEEE Transactions on Industrial Electronics*, vol. 50, no. 5, pp. 962–981, 2003. DOI: 10.1109/TIE.2003.817609.

[171] G. Town, S. Taghizadeh, and S. Deilami, "Review of fast charging for electrified transport: Demand, technology, systems, and planning," *Energies*, vol. 15, no. 4, 2022, ISSN: 1996-1073. DOI: 10.3390/en15041276. [Online]. Available: https://www.mdpi.com/1996-1073/15/4/1276.

[172] C.-Y. Lim, Y. Jeong, and G.-W. Moon, "Phase-shifted full-bridge dc–dc converter with high efficiency and high power density using center-tapped clamp circuit for battery charging in electric vehicles," *IEEE Transactions on Power Electronics*, vol. 34, no. 11, pp. 10 945–10 959, 2019. DOI: 10.1109/TPEL.2019.2899960.

[173] J.-Y. Lee, J.-H. Chen, and K.-Y. Lo, "An interleaved phase-shift full-bridge converter with dynamic dead time control for server power applications," *Energies*, vol. 14, no. 4, 2021, ISSN: 1996-1073. DOI: 10.3390/en14040853. [Online]. Available: https://www.mdpi.com/1996-1073/14/4/853.

[174] H.-P. Park, M. Kim, and J.-H. Jung, "A comprehensive overview in control algorithms for high switching-frequency llc resonant converter," *Energies*, vol. 13, no. 17, 2020, ISSN: 1996-1073. DOI: 10.3390/en13174455. [Online]. Available: https://www.mdpi.com/1996-1073/13/17/4455.

[175] F. Wu, Z. Wang, and S. Luo, "Buck–boost three-level semi-dual-bridge resonant isolated dc–dc converter," *IEEE Journal of Emerging and Selected Topics in Power Electronics*, vol. 9, no. 5, pp. 5986–5995, 2021. DOI: 10.1109/JESTPE.2020.3041094.

[176] M. Gierczynski, L. M. Grzesiak, and A. Kaszewski, "Cascaded voltage and current control for a dual active bridge converter with current filters," *Energies*, vol. 14, no. 19, 2021, ISSN: 1996-1073. DOI: 10.3390/en14196214. [Online]. Available: https://www.mdpi.com/1996-1073/14/19/6214.

[177] H. Li, F. Z. Peng, and J. Lawler, "A natural zvs medium-power bidirectional dc-dc converter with minimum number of devices," *IEEE Transactions on Industry Applications*, vol. 39, no. 2, pp. 525–535, 2003. DOI: 10.1109/TIA.2003.808965.

[178] H. Fan and H. Li, "High-frequency transformer isolated bidirectional dc–dc converter modules with high efficiency over wide load range for 20 kva solid-state transformer," *IEEE Transactions on Power Electronics*, vol. 26, no. 12, pp. 3599–3608, 2011. DOI: 10.1109/TPEL.2011.2160652.

[179] Y. Gu, Z. Lu, L. Hang, Z. Qian, and G. Huang, "Three-level llc series resonant dc/dc converter," *IEEE Transactions on Power Electronics*, vol. 20, no. 4, pp. 781–789, 2005. DOI: 10.1109/TPEL.2005.850921.

[180] S. Falcones, R. Ayyanar, and X. Mao, "A dc–dc multiport-converter-based solid-state transformer integrating distributed generation and storage," *IEEE Transactions on Power Electronics*, vol. 28, no. 5, pp. 2192–2203, 2013. DOI: 10.1109/TPEL.2012.2215965.

[181] M. Moonem and H. Krishnaswami, "Analysis and control of multi-level dual active bridge dc-dc converter," in *2012 IEEE Energy Conversion Congress and Exposition (ECCE)*, 2012, pp. 1556–1561. DOI: 10.1109/ECCE.2012.6342628.

[182] W. Chen, P. Rong, and Z. Lu, "Snubberless bidirectional dc–dc converter with new cllc resonant tank featuring minimized switching loss," *IEEE Transactions on Industrial Electronics*, vol. 57, no. 9, pp. 3075–3086, 2010. DOI: 10.1109/TIE.2009.2037099.

[183] Y. Du, S. Lukic, B. Jacobson, and A. Huang, "Review of high power isolated bi-directional dc-dc converters for phev/ev dc charging infrastructure," in *2011*

IEEE Energy Conversion Congress and Exposition, 2011, pp. 553–560. DOI: 10.1109/ECCE.2011.6063818.

[184] M. Frivaldsky, S. Kascak, J. Morgos, and M. Prazenica, "From non-modular to modular concept of bidirectional buck/boost converter for microgrid applications," *Energies*, vol. 13, no. 12, 2020, ISSN: 1996-1073. DOI: 10.3390/en13123287. [Online]. Available: https://www.mdpi.com/1996-1073/13/12/3287.

[185] O. Garcia, P. Zumel, A. de Castro, and A. Cobos, "Automotive dc-dc bidirectional converter made with many interleaved buck stages," *IEEE Transactions on Power Electronics*, vol. 21, no. 3, pp. 578–586, 2006. DOI: 10.1109/TPEL.2006.872379.

[186] M. Zhang, Y. Jiang, F. Lee, and M. Jovanovic, "Single-phase three-level boost power factor correction converter," in *Proceedings of 1995 IEEE Applied Power Electronics Conference and Exposition - APEC'95*, vol. 1, 1995, 434–439 vol.1. DOI: 10.1109/APEC.1995.468984.

[187] P. J. Grbović, P. Delarue, P. Le Moigne, and P. Bartholomeus, "A bidirectional three-level dc–dc converter for the ultracapacitor applications," *IEEE Transactions on Industrial Electronics*, vol. 57, no. 10, pp. 3415–3430, 2010. DOI: 10.1109/TIE.2009.2038338.

[188] W. Qi, S. Li, H. Yuan, S.-C. Tan, and S.-Y. Hui, "High-power-density single-phase three-level flying-capacitor buck pfc rectifier," *IEEE Transactions on Power Electronics*, vol. 34, no. 11, pp. 10 833–10 844, 2019. DOI: 10.1109/TPEL.2019.2896585.

[189] L. Shi, B. P. Baddipadiga, M. Ferdowsi, and M. L. Crow, "Improving the dynamic response of a flying-capacitor three-level buck converter," *IEEE Transactions on Power Electronics*, vol. 28, no. 5, pp. 2356–2365, 2013. DOI: 10.1109/TPEL.2012.2216291.

[190] K. Clement-Nyns, E. Haesen, and J. Driesen, "The impact of charging plug-in hybrid electric vehicles on a residential distribution grid," *IEEE Transactions on Power Systems*, vol. 25, no. 1, pp. 371–380, 2010. DOI: 10.1109/TPWRS.2009.2036481.

[191] H. Höimoja, M. Vasiladiotis, and A. Rufer, "Power interfaces and storage selection for an ultrafast ev charging station," in *6th IET International Conference on Power Electronics, Machines and Drives (PEMD 2012)*, 2012, pp. 1–6. DOI: 10.1049/cp.2012.0309.

[192] B. Aluisio, S. Bruno, L. De Bellis, M. Dicorato, G. Forte, and M. Trovato, "Dc-microgrid operation planning for an electric vehicle supply infrastructure," *Applied Sciences*, vol. 9, no. 13, 2019, ISSN: 2076-3417. DOI: 10.3390/app9132687. [Online]. Available: https://www.mdpi.com/2076-3417/9/13/2687.

[193] S. Kaur, T. Kaur, R. Khanna, and P. Singh, "A state of the art of dc microgrids for electric vehicle charging," in *2017 4th International Conference on Signal Processing, Computing and Control (ISPCC)*, 2017, pp. 381–386. DOI: 10.1109/ISPCC.2017.8269708.

[194] S. Negarestani, M. Fotuhi-Firuzabad, M. Rastegar, and A. Rajabi-Ghahnavieh, "Optimal sizing of storage system in a fast charging station for plug-in hybrid electric vehicles," *IEEE Transactions on Transportation Electrification*, vol. 2, no. 4, pp. 443–453, 2016. DOI: 10.1109/TTE.2016.2559165.

[195] J. Mohammadi, F. Badrkhani Ajaei, and G. Stevens, "Grounding the dc microgrid," *IEEE Transactions on Industry Applications*, vol. 55, no. 5, pp. 4490–4499, 2019. DOI: 10.1109/TIA.2019.2928278.

[196] E. Apostolaki-Iosifidou, P. Codani, and W. Kempton, "Measurement of power loss during electric vehicle charging and discharging," *Energy*, vol. 127, pp. 730–742, 2017, ISSN: 0360-5442. DOI: 10.1016/j.energy.2017.03.015. [Online]. Available: https://www.sciencedirect.com/science/article/pii/S0360544217303730.

[197] M. Wang, A. Vandermaar, and K. Srivastava, "Review of condition assessment of power transformers in service," *IEEE Electrical Insulation Magazine*, vol. 18, no. 6, pp. 12–25, 2002. DOI: 10.1109/MEI.2002.1161455.

[198] R. Kabiri, D. G. Holmes, B. P. McGrath, and L. G. Meegahapola, "Lv grid voltage regulation using transformer electronic tap changing, with pv inverter reactive power injection," *IEEE Journal of Emerging and Selected Topics in Power Electronics*, vol. 3, no. 4, pp. 1182–1192, 2015. DOI: 10.1109/JESTPE.2015.2443839.

[199] X. She, A. Q. Huang, and R. Burgos, "Review of solid-state transformer technologies and their application in power distribution systems," *IEEE Journal of Emerging and Selected Topics in Power Electronics*, vol. 1, no. 3, pp. 186–198, 2013. DOI: 10.1109/JESTPE.2013.2277917.

[200] W. Mcmurray, "Power converter circuits having a high-frequency link," 1970, U.S. Patent US3517300A.

[201] D. Divan, R. Moghe, and A. Prasai, "Power electronics at the grid edge : The key to unlocking value from the smart grid," *IEEE Power Electronics Magazine*, vol. 1, no. 4, pp. 16–22, 2014. DOI: 10.1109/MPEL.2014.2360811.

[202] D. Dujic, C. Zhao, A. Mester, *et al.*, "Power electronic traction transformer-low voltage prototype," *IEEE Transactions on Power Electronics*, vol. 28, no. 12, pp. 5522–5534, 2013. DOI: 10.1109/TPEL.2013.2248756.

[203] F. Wang, Z. Zhang, T. Ericsen, R. Raju, R. Burgos, and D. Boroyevich, "Advances in power conversion and drives for shipboard systems," *Proceedings of the IEEE*, vol. 103, no. 12, pp. 2285–2311, 2015. DOI: 10.1109/JPROC.2015.2495331.

[204] A. Q. Huang, M. L. Crow, G. T. Heydt, J. P. Zheng, and S. J. Dale, "The future renewable electric energy delivery and management (freedm) system: The energy internet," *Proceedings of the IEEE*, vol. 99, no. 1, pp. 133–148, 2011. DOI: 10.1109/JPROC.2010.2081330.

[205] L. Ferreira Costa, G. De Carne, G. Buticchi, and M. Liserre, "The smart transformer: A solid-state transformer tailored to provide ancillary services to the distribution grid," *IEEE Power Electronics Magazine*, vol. 4, no. 2, pp. 56–67, 2017. DOI: 10.1109/MPEL.2017.2692381.

[206] "Energy conversation program for commercial equipment, distribution transformers energy conversation standards," 2007, CFR Standard 431.

[207] H. Shadfar, M. Ghorbani Pashakolaei, and A. Akbari Foroud, "Solid-state transformers: An overview of the concept, topology, and its applications in the smart grid," *International Transactions on Electrical Energy Systems*, vol. 31, no. 9, e12996, 2021. DOI: https://doi.org/10.1002/2050-7038.12996.

[Online]. Available: https://onlinelibrary.wiley.com/doi/abs/10.1002/2050-7038.12996.

[208] M. E. Adabi Firouzjaee, "Advanced modeling of solid state transformer," Ph.D. dissertation, 2018.

[209] H. Qin and J. W. Kimball, "Solid-state transformer architecture using ac–ac dual-active-bridge converter," *IEEE Transactions on Industrial Electronics*, vol. 60, no. 9, pp. 3720–3730, 2013. DOI: 10.1109/TIE.2012.2204710.

[210] A. Rodriguez, M. R. Rogina, M. Saeed, *et al.*, "Auxiliary power supply based on a modular isop flyback configuration with very high input voltage," in *2016 IEEE Energy Conversion Congress and Exposition (ECCE)*, 2016, pp. 1–7. DOI: 10.1109/ECCE.2016.7854894.

[211] P. Drabek, Z. Peroutka, M. Pittermann, and M. Cedl, "New configuration of traction converter with medium-frequency transformer using matrix converters," *IEEE Transactions on Industrial Electronics*, vol. 58, no. 11, pp. 5041–5048, 2011. DOI: 10.1109/TIE.2011.2138114.

[212] H. Chen, A. Prasai, and D. Divan, "Dyna-c: A minimal topology for bidirectional solid-state transformers," *IEEE Transactions on Power Electronics*, vol. 32, no. 2, pp. 995–1005, 2017. DOI: 10.1109/TPEL.2016.2547983.

[213] H. Qin and J. W. Kimball, "Ac-ac dual active bridge converter for solid state transformer," in *2009 IEEE Energy Conversion Congress and Exposition*, 2009, pp. 3039–3044. DOI: 10.1109/ECCE.2009.5316507.

[214] M. A. Hannan, P. J. Ker, M. S. H. Lipu, *et al.*, "State of the art of solid-state transformers: Advanced topologies, implementation issues, recent progress and

improvements," *IEEE Access*, vol. 8, pp. 19 113–19 132, 2020. DOI: 10.1109/ACCESS.2020.2967345.

[215] D. K. Mishra, M. J. Ghadi, L. Li, *et al.*, "A review on solid-state transformer: A breakthrough technology for future smart distribution grids," *International Journal of Electrical Power & Energy Systems*, vol. 133, p. 107 255, 2021, ISSN: 0142-0615. DOI: https://doi.org/10.1016/j.ijepes.2021.107255. [Online]. Available: https://www.sciencedirect.com/science/article/pii/S0142061521004944.

[216] J. W. Kolar and J. E. Huber, *Solid-state transformers - key design challenges, applicability, and future concepts*, en, 17th International Conference on Power Electronics and Motion Control (PEMC 2016); Conference Location: Varna, Bulgaria; Conference Date: September 25-30, 2016, 2016.

[217] Y. Guan, C. Cecati, J. M. Alonso, and Z. Zhang, "Review of high-frequency high-voltage-conversion-ratio dc–dc converters," *IEEE Journal of Emerging and Selected Topics in Industrial Electronics*, vol. 2, no. 4, pp. 374–389, 2021. DOI: 10.1109/JESTIE.2021.3051554.

[218] I. Alhurayyis, A. Elkhateb, and J. Morrow, "Isolated and nonisolated dc-to-dc converters for medium-voltage dc networks: A review," *IEEE Journal of Emerging and Selected Topics in Power Electronics*, vol. 9, no. 6, pp. 7486–7500, 2021. DOI: 10.1109/JESTPE.2020.3028057.

[219] S. Falcones, X. Mao, and R. Ayyanar, "Topology comparison for solid state transformer implementation," in *IEEE PES General Meeting*, 2010, pp. 1–8. DOI: 10.1109/PES.2010.5590086.

[220] L. Heinemann and G. Mauthe, "The universal power electronics based distribution transformer, an unified approach," in *2001 IEEE 32nd Annual Power Electronics Specialists Conference (IEEE Cat. No.01CH37230)*, vol. 2, 2001, 504–509 vol.2. DOI: 10.1109/PESC.2001.954164.

[221] C. Lu, W. Hu, and F. C. Lee, "Neutral-point voltage balancing methods of series-half-bridge llc converter for solid state transformer," *IEEE Transactions on Power Electronics*, vol. 36, no. 6, pp. 7060–7073, 2021. DOI: 10.1109/TPEL.2020.3035150.

[222] S.-H. Kim, R.-Y. Kim, and S.-I. Kim, "Generalized model predictive control method for single-phase *N*-level flying capacitor multilevel rectifiers for solid state transformer," *IEEE Transactions on Industry Applications*, vol. 55, no. 6, pp. 7505–7514, 2019. DOI: 10.1109/TIA.2019.2917869.

[223] S. Stynski, M. Grzegorczyk, C. Sobol, and R. Kot, "Current control strategies for a star connected cascaded h-bridge converter operating as mv-ac to mv-dc stage of a solid state transformer," *Energies*, vol. 14, no. 15, 2021, ISSN: 1996-1073. DOI: 10.3390/en14154607. [Online]. Available: https://www.mdpi.com/1996-1073/14/15/4607.

[224] M. E. Adabi, J. A. Martinez-Velasco, and S. Alepuz, "Modeling and simulation of a MMC-based solid-state transformer," *Electrical Engineering*, vol. 100, no. 2, pp. 375–387, Jun. 2018, ISSN: 1432-0487. DOI: 10.1007/s00202-017-0510-x. [Online]. Available: https://doi.org/10.1007/s00202-017-0510-x.

[225] L. A. M. Barros, A. P. Martins, and J. G. Pinto, "A comprehensive review on modular multilevel converters, submodule topologies, and modulation techniques," *Energies*, vol. 15, no. 3, 2022, ISSN: 1996-1073. DOI: 10.3390/en15031078. [Online]. Available: https://www.mdpi.com/1996-1073/15/3/1078.

[226] L. Zheng, X. Han, R. P. Kandula, K. Kandasamy, M. Saeedifard, and D. Divan, "7.2 kv three-port single-phase single-stage modular soft-switching solid-state transformer with active power decoupling and reduced dc-link," in *2020 IEEE Applied Power Electronics Conference and Exposition (APEC)*, 2020, pp. 1575–1581. DOI: 10.1109/APEC39645.2020.9124244.

[227] M. T. Iqbal, A. I. Maswood, K. Yeo, and M. Tariq, "Dynamic model and analysis of three phase yd transformer based dual active bridge using optimised harmonic number for solid state transformer in distributed system," in *2018 IEEE Innovative Smart Grid Technologies - Asia (ISGT Asia)*, 2018, pp. 523–527. DOI: 10.1109/ISGT-Asia.2018.8467858.

[228] K. Mainali, A. Tripathi, S. Madhusoodhanan, *et al.*, "A transformerless intelligent power substation: A three-phase sst enabled by a 15-kv sic igbt," *IEEE Power Electronics Magazine*, vol. 2, no. 3, pp. 31–43, 2015. DOI: 10.1109/MPEL.2015.2449271.

[229] S. Madhusoodhanan, A. Tripathi, A. Kadavelugu, *et al.*, "Experimental validation of the steady state and transient behavior of a transformerless intelligent power substation," in *2014 IEEE Applied Power Electronics Conference and Exposition - APEC 2014*, 2014, pp. 3477–3484. DOI: 10.1109/APEC.2014.6803809.

[230] J. E. Huber, D. Rothmund, and J. W. Kolar, "Comparative evaluation of isolated front end and isolated back end multi-cell ssts," in *2016 IEEE 8th International*

Power Electronics and Motion Control Conference (IPEMC-ECCE Asia), 2016, pp. 3536–3545. DOI: 10.1109/IPEMC.2016.7512863.

[231] J. Lee, J. Roh, M. Y. Kim, S.-H. Baek, S. Kim, and S.-H. Lee, "A novel solid-state transformer with loosely coupled resonant dual-active-bridge converters," *IEEE Transactions on Industry Applications*, vol. 58, no. 1, pp. 709–719, 2022. DOI: 10.1109/TIA.2021.3119535.

[232] A. Q. Huang, "Power semiconductor devices for smart grid and renewable energy systems," *Proceedings of the IEEE*, vol. 105, no. 11, pp. 2019–2047, 2017. DOI: 10.1109/JPROC.2017.2687701.

[233] M. Andresen, K. Ma, G. Buticchi, J. Falck, F. Blaabjerg, and M. Liserre, "Junction temperature control for more reliable power electronics," *IEEE Transactions on Power Electronics*, vol. 33, no. 1, pp. 765–776, 2018. DOI: 10.1109/TPEL.2017.2665697.

[234] L. R. GopiReddy, L. M. Tolbert, and B. Ozpineci, "Power cycle testing of power switches: A literature survey," *IEEE Transactions on Power Electronics*, vol. 30, no. 5, pp. 2465–2473, 2015. DOI: 10.1109/TPEL.2014.2359015.

[235] M. Bierhoff and F. Fuchs, "Semiconductor losses in voltage source and current source igbt converters based on analytical derivation," in *2004 IEEE 35th Annual Power Electronics Specialists Conference (IEEE Cat. No.04CH37551)*, vol. 4, 2004, 2836–2842 Vol.4. DOI: 10.1109/PESC.2004.1355283.

[236] D Graovac and M. Pürschel, "Igbt power losses calculation using the data-sheet parameters," *Infineon Technologies Application*, vol. 1, pp. 1–12, 2009, Neubiberg, Germany.

[237] H. Hafezi and R. Faranda, "A new approach for power losses evaluation of igbt/-diode module," *Electronics*, vol. 10, no. 3, 2021, ISSN: 2079-9292. DOI: 10.3390/electronics10030280. [Online]. Available: https://www.mdpi.com/2079-9292/10/3/280.

[238] L. Ma, H. Xu, A. Q. Huang, J. Zou, and K. Li, "Igbt dynamic loss reduction through device level soft switching," *Energies*, vol. 11, no. 5, 2018. DOI: 10.3390/en11051182.

[239] I. Batarseh and A. Harb, "Soft-switching dc-dc converters," in *Power Electronics: Circuit Analysis and Design*. Cham: Springer International Publishing, 2018, pp. 347–460, ISBN: 978-3-319-68366-9. DOI: 10.1007/978-3-319-68366-9_6. [Online]. Available: https://doi.org/10.1007/978-3-319-68366-9_6.

[240] J. Kolar, H. Ertl, and F. Zach, "Influence of the modulation method on the conduction and switching losses of a pwm converter system," *IEEE Transactions on Industry Applications*, vol. 27, no. 6, pp. 1063–1075, 1991. DOI: 10.1109/28.108456.

[241] J. Millán, P. Godignon, X. Perpiñà, A. Pérez-Tomás, and J. Rebollo, "A survey of wide bandgap power semiconductor devices," *IEEE Transactions on Power Electronics*, vol. 29, no. 5, pp. 2155–2163, 2014. DOI: 10.1109/TPEL.2013.2268900.

[242] J.-S. Lai, W. Yu, P. Sun, *et al.*, "A hybrid-switch-based soft-switching inverter for ultrahigh-efficiency traction motor drives," *IEEE Transactions on Industry Applications*, vol. 50, no. 3, pp. 1966–1973, 2014. DOI: 10.1109/TIA.2013.2284296.

[243] J. Ballestín-Fuertes, J. Muñoz-Cruzado-Alba, J. F. Sanz-Osorio, and E. Laporta-Puyal, "Role of wide bandgap materials in power electronics for smart grids applications," *Electronics*, vol. 10, no. 6, 2021, ISSN: 2079-9292. DOI: 10.3390/electronics10060677. [Online]. Available: https://www.mdpi.com/2079-9292/10/6/677.

[244] R. A. Minamisawa, U. Vemulapati, A. Mihaila, C. Papadopoulos, and M. Rahimo, "Current sharing behavior in si igbt and sic mosfet cross-switch hybrid," *IEEE Electron Device Letters*, vol. 37, no. 9, pp. 1178–1180, 2016. DOI: 10.1109/LED.2016.2596302.

[245] J. Wheeler, "Effects of converter pulses on the electrical insulation in low and medium voltage motors," *IEEE Electrical Insulation Magazine*, vol. 21, no. 2, pp. 22–29, 2005. DOI: 10.1109/MEI.2005.1412216.

[246] E. Velander, L. Kruse, T. Wiik, A. Wiberg, J. Colmenares, and H.-P. Nee, "An igbt turn-on concept offering low losses under motor drive dv/dt constraints based on diode current adaption," *IEEE Transactions on Power Electronics*, vol. 33, no. 2, pp. 1143–1153, 2018. DOI: 10.1109/TPEL.2017.2688474.

[247] H. Riazmontazer and S. K. Mazumder, "Optically switched-drive-based unified independent <italic>dv/dt</italic> and <italic>di/dt</italic> control for turn-off transition of power mosfets," *IEEE Transactions on Power Electronics*, vol. 30, no. 4, pp. 2338–2349, 2015. DOI: 10.1109/TPEL.2014.2327014.

[248] N. Oswald, P. Anthony, N. McNeill, and B. H. Stark, "An experimental investigation of the tradeoff between switching losses and emi generation with hard-switched all-si, si-sic, and all-sic device combinations," *IEEE Transactions on Power Electronics*, vol. 29, no. 5, pp. 2393–2407, 2014. DOI: 10.1109/TPEL.2013.2278919.

[249] K. Vechalapu, A. K. Kadavelugu, and S. Bhattacharya, "High voltage dual active bridge with series connected high voltage silicon carbide (sic) devices," in *2014 IEEE Energy Conversion Congress and Exposition (ECCE)*, 2014, pp. 2057–2064. DOI: 10.1109/ECCE.2014.6953674.

[250] K. K.-F. Yuen and H. S.-H. Chung, "A low-loss "rl-plus-c" filter for overvoltage suppression in inverter-fed drive system with long motor cable," *IEEE Transactions on Power Electronics*, vol. 30, no. 4, pp. 2167–2181, 2015. DOI: 10.1109/TPEL.2014.2325824.

[251] J. E. Huber and J. W. Kolar, "Optimum number of cascaded cells for high-power medium-voltage ac–dc converters," *IEEE Journal of Emerging and Selected Topics in Power Electronics*, vol. 5, no. 1, pp. 213–232, 2017. DOI: 10.1109/JESTPE.2016.2605702.

[252] V. M. Iyer, S. Sharma, and S. Bhattacharya, "A methodology to select the number of cascaded cells for a medium voltage multilevel ac-dc solid state transformer," in *2020 IEEE Transportation Electrification Conference Expo (ITEC)*, 2020, pp. 55–61. DOI: 10.1109/ITEC48692.2020.9161462.

[253] H. Chen and D. Divan, "Soft-switching solid-state transformer (s4t)," *IEEE Transactions on Power Electronics*, vol. 33, no. 4, pp. 2933–2947, 2018. DOI: 10.1109/TPEL.2017.2707581.

[254] A. Q. Huang, Q. Zhu, L. Wang, and L. Zhang, "15 kv sic mosfet: An enabling technology for medium voltage solid state transformers," *CPSS Transactions on Power Electronics and Applications*, vol. 2, no. 2, pp. 118–130, 2017. DOI: 10.24295/CPSSTPEA.2017.00012.

[255] D. Grider, M. Das, A. Agarwal, *et al.*, "10 kv/120 a sic dmosfet half h-bridge power modules for 1 mva solid state power substation," in *2011 IEEE Electric Ship Technologies Symposium*, 2011, pp. 131–134. DOI: 10.1109/ESTS.2011.5770855.

[256] E. van Brunt, L. Cheng, M. J. O'Loughlin, *et al.*, "27 kv, 20 a 4h-sic n-igbts," in *Silicon Carbide and Related Materials 2014*, ser. Materials Science Forum, vol. 821, Trans Tech Publications Ltd, Jul. 2015, pp. 847–850. DOI: 10.4028/www.scientific.net/MSF.821-823.847.

[257] A. Anurag, S. Acharya, N. Kolli, S. Bhattacharya, T. R. Weatherford, and A. A. Parker, "A three-phase active-front-end converter system enabled by 10-kv sic mosfets aimed at a solid-state transformer application," *IEEE Transactions on Power Electronics*, vol. 37, no. 5, pp. 5606–5624, 2022. DOI: 10.1109/TPEL.2021.3131262.

[258] S. Zhao, Q. Li, F. C. Lee, and B. Li, "High-frequency transformer design for modular power conversion from medium-voltage ac to 400 vdc," *IEEE Transactions on Power Electronics*, vol. 33, no. 9, pp. 7545–7557, 2018. DOI: 10.1109/TPEL.2017.2774440.

[259] R. Petkov, "Optimum design of a high-power, high-frequency transformer," *IEEE Transactions on Power Electronics*, vol. 11, no. 1, pp. 33–42, 1996. DOI: 10.1109/63.484414.

[260] X. She, R. Burgos, G. Wang, F. Wang, and A. Q. Huang, "Review of solid state transformer in the distribution system: From components to field application," in *2012 IEEE Energy Conversion Congress and Exposition (ECCE)*, 2012, pp. 4077–4084. DOI: 10.1109/ECCE.2012.6342269.

[261] G. Ortiz, M. Leibl, J. W. Kolar, and O. Apeldoorn, "Medium frequency transformers for solid-state-transformer applications — design and experimental verification," in *2013 IEEE 10th International Conference on Power Electronics and Drive Systems (PEDS)*, 2013, pp. 1285–1290. DOI: 10.1109/PEDS.2013.6527217.

[262] E. Agheb and H. K. Høidalen, "Medium frequency high power transformers, state of art and challenges," in *2012 International Conference on Renewable Energy Research and Applications (ICRERA)*, 2012, pp. 1–6. DOI: 10.1109/ICRERA.2012.6477318.

[263] Y. Guo, C. Lu, L. Hua, and X. Zhang, "Optimal design of high-power medium-frequency transformer using hollow conductors with consideration of multi-objective parameters," *Energies*, vol. 13, no. 14, 2020, ISSN: 1996-1073. DOI: 10.3390/en13143654. [Online]. Available: https://www.mdpi.com/1996-1073/13/14/3654.

[264] E. Hussain, M. Abusara, and S. Sharkh, "Design optimisation of a current-fed solid-state transformer for mv grid-connected applications," *Energies*, vol. 14, no. 11, 2021, ISSN: 1996-1073. DOI: 10.3390/en14113283. [Online]. Available: https://www.mdpi.com/1996-1073/14/11/3283.

[265] M. A. Bahmani, T. Thiringer, and H. Ortega, "An accurate pseudoempirical model of winding loss calculation in hf foil and round conductors in switchmode magnetics," *IEEE Transactions on Power Electronics*, vol. 29, no. 8, pp. 4231–4246, 2014. DOI: 10.1109/TPEL.2013.2292593.

[266] R. Escarela-Pérez, "Selection of copper against aluminium windings for distribution transformers," English, *IET Electric Power Applications*, vol. 4, 474–485(11), 6 2010, ISSN: 1751-8660. [Online]. Available: https://digital-

library.theiet.org/content/journals/10.1049/iet-epa.2009.0297.

[267] M. Kheraluwala, D. Novotny, and D. Divan, "Design considerations for high power high frequency transformers," in *21st Annual IEEE Conference on Power Electronics Specialists*, 1990, pp. 734–742. DOI: 10.1109/PESC.1990.131262.

[268] E. L. Barrios, A. Urtasun, A. Ursúa, L. Marroyo, and P. Sanchis, "High-frequency power transformers with foil windings: Maximum interleaving and optimal design," *IEEE Transactions on Power Electronics*, vol. 30, no. 10, pp. 5712–5723, 2015. DOI: 10.1109/TPEL.2014.2368832.

[269] M. Leibl, G. Ortiz, and J. W. Kolar, "Design and experimental analysis of a medium-frequency transformer for solid-state transformer applications," *IEEE Journal of Emerging and Selected Topics in Power Electronics*, vol. 5, no. 1, pp. 110–123, 2017. DOI: 10.1109/JESTPE.2016.2623679.

[270] F. Bignucolo, M. Bertoluzzo, and C. Fontana, "Applications of the solid state transformer concept in the electrical power system," in *2015 AEIT International Annual Conference (AEIT)*, 2015, pp. 1–6. DOI: 10.1109/AEIT.2015.7415235.

[271] I. Syed and V. Khadkikar, "Replacing the grid interface transformer in wind energy conversion system with solid-state transformer," *IEEE Transactions on Power Systems*, vol. 32, no. 3, pp. 2152–2160, 2017. DOI: 10.1109/TPWRS.2016.2614692.

[272] X. She, A. Q. Huang, F. Wang, and R. Burgos, "Wind energy system with integrated functions of active power transfer, reactive power compensation, and voltage conversion," *IEEE Transactions on Industrial Electronics*, vol. 60, no. 10, pp. 4512–4524, 2013. DOI: 10.1109/TIE.2012.2216245.

[273] J. Feng, J. Shang, Z. Zhang, H. Liu, and Z. Huang, "Solid-state transformer-based new traction drive system and control," *Frontiers of Mechanical Engineering*, vol. 13, no. 3, pp. 411–426, Sep. 2018, ISSN: 2095-0241. DOI: 10.1007/s11465-018-0467-0. [Online]. Available: https://doi.org/10.1007/s11465-018-0467-0.

[274] S. Farnesi, M. Marchesoni, M. Passalacqua, and L. Vaccaro, "Solid-state transformers in locomotives fed through ac lines: A review and future developments," *Energies*, vol. 12, no. 24, 2019, ISSN: 1996-1073. DOI: 10.3390/en12244711. [Online]. Available: https://www.mdpi.com/1996-1073/12/24/4711.

[275] Y. Liu, Y. Liu, H. Abu-Rub, and B. Ge, "Model predictive control of matrix converter based solid state transformer," in *2016 IEEE International Conference on Industrial Technology (ICIT)*, 2016, pp. 1248–1253. DOI: 10.1109/ICIT.2016.7474933.

[276] X. She, A. Q. Huang, S. Lukic, and M. E. Baran, "On integration of solid-state transformer with zonal dc microgrid," *IEEE Transactions on Smart Grid*, vol. 3, no. 2, pp. 975–985, 2012. DOI: 10.1109/TSG.2012.2187317.

[277] F. Bignucolo and M. Bertoluzzo, "Application of solid-state transformers in a novel architecture of hybrid ac/dc house power systems," *Energies*, vol. 13, no. 13, 2020, ISSN: 1996-1073. DOI: 10.3390/en13133432. [Online]. Available: https://www.mdpi.com/1996-1073/13/13/3432.

[278] E. I. Pool-Mazun, J. J. Sandoval, P. N. Enjeti, and I. J. Pitel, "An integrated solid-state transformer with high-frequency isolation for ev fast-charging applications," *IEEE Journal of Emerging and Selected Topics in Industrial Electronics*, vol. 1, no. 1, pp. 46–56, 2020. DOI: 10.1109/JESTIE.2020.3003355.

[279] T. Zhao, J. Zeng, S. Bhattacharya, M. E. Baran, and A. Q. Huang, "An average model of solid state transformer for dynamic system simulation," in *2009 IEEE Power Energy Society General Meeting*, 2009, pp. 1–8. DOI: 10.1109/PES.2009.5275542.

[280] M. T. A. Khan, A. A. Milani, A. Chakrabortty, and I. Husain, "Dynamic modeling and feasibility analysis of a solid-state transformer-based power distribution system," *IEEE Transactions on Industry Applications*, vol. 54, no. 1, pp. 551–562, 2018. DOI: 10.1109/TIA.2017.2757450.

[281] Z. Yu, R. Ayyanar, and I. Husain, "A detailed analytical model of a solid state transformer," in *2015 IEEE Energy Conversion Congress and Exposition (ECCE)*, 2015, pp. 723–729. DOI: 10.1109/ECCE.2015.7309761.

[282] Y. Jiang, L. Breazeale, R. Ayyanar, and X. Mao, "Simplified solid state transformer modeling for real time digital simulator (rtds)," in *2012 IEEE Energy Conversion Congress and Exposition (ECCE)*, 2012, pp. 1447–1452. DOI: 10.1109/ECCE.2012.6342644.

[283] D. G. Shah and M. L. Crow, "Stability design criteria for distribution systems with solid-state transformers," *IEEE Transactions on Power Delivery*, vol. 29, no. 6, pp. 0–0, 2014. DOI: 10.1109/TPWRD.2014.2311963.

[284] R. L. Da Silva, V. L. F. Borges, C. E. Possamai, and I. Barbi, "Solid-state transformer for power distribution grid based on a hybrid switched-capacitor

llc-src converter: Analysis, design, and experimentation," *IEEE Access*, vol. 8, pp. 141 182–141 207, 2020. DOI: 10.1109/ACCESS.2020.3013188.

[285] A. C. Nair and B. G. Fernandes, "Solid-state transformer based fast charging station for various categories of electric vehicles with batteries of vastly different ratings," *IEEE Transactions on Industrial Electronics*, vol. 68, no. 11, pp. 10 400–10 411, 2021. DOI: 10.1109/TIE.2020.3038091.

[286] X. She, X. Yu, F. Wang, and A. Q. Huang, "Design and demonstration of a 3.6kv–120v/10kva solid state transformer for smart grid application," in *2014 IEEE Applied Power Electronics Conference and Exposition - APEC 2014*, 2014, pp. 3429–3436. DOI: 10.1109/APEC.2014.6803801.

[287] F. Wang, G. Wang, A. Huang, W. Yu, and X. Ni, "Design and operation of a 3.6kv high performance solid state transformer based on 13kv sic mosfet and jbs diode," in *2014 IEEE Energy Conversion Congress and Exposition (ECCE)*, 2014, pp. 4553–4560. DOI: 10.1109/ECCE.2014.6954024.

[288] J.-W. Lim, Y. Cho, H.-S. Lee, and K.-Y. Cho, "Design and control of a 13.2 kv/10 kva single-phase solid-state-transformer with 1.7 kv sic devices," *Energies*, vol. 11, no. 1, 2018, ISSN: 1996-1073. DOI: 10.3390/en11010201. [Online]. Available: https://www.mdpi.com/1996-1073/11/1/201.

[289] M. Lee, C.-S. Yeh, O. Yu, J.-W. Kim, J.-M. Choe, and J.-S. Lai, "Modeling and control of three-level boost rectifier based medium-voltage solid-state transformer for dc fast charger application," *IEEE Transactions on Transportation Electrification*, vol. 5, no. 4, pp. 890–902, 2019. DOI: 10.1109/TTE.2019.2919200.

[290] G. Wang, S. Baek, J. Elliott, *et al.*, "Design and hardware implementation of gen-1 silicon based solid state transformer," in *2011 Twenty-Sixth Annual IEEE Applied*

Power Electronics Conference and Exposition (APEC), 2011, pp. 1344–1349. DOI: 10.1109/APEC.2011.5744766.

[291] J.-S. Lai, W.-H. Lai, S.-R. Moon, L. Zhang, and A. Maitra, "A 15-kv class intelligent universal transformer for utility applications," in *2016 IEEE Applied Power Electronics Conference and Exposition (APEC)*, 2016, pp. 1974–1981. DOI: 10.1109/APEC.2016.7468139.

[292] D. Rothmund, T. Guillod, D. Bortis, and J. W. Kolar, "99% efficient 10 kv sic-based 7 kv/400 v dc transformer for future data centers," *IEEE Journal of Emerging and Selected Topics in Power Electronics*, vol. 7, no. 2, pp. 753–767, 2019. DOI: 10.1109/JESTPE.2018.2886139.

[293] S. Srdic, X. Liang, C. Zhang, W. Yu, and S. Lukic, "A sic-based high-performance medium-voltage fast charger for plug-in electric vehicles," in *2016 IEEE Energy Conversion Congress and Exposition (ECCE)*, 2016, pp. 1–6. DOI: 10.1109/ECCE.2016.7854777.

[294] A. Anurag, S. Acharya, S. Bhattacharya, T. R. Weatherford, and A. Parker, "A gen-3 10 kv sic mosfets based medium voltage three-phase dual active bridge converter enabling a mobile utility support equipment solid state transformer (muse-sst)," *IEEE Journal of Emerging and Selected Topics in Power Electronics*, pp. 1–1, 2021. DOI: 10.1109/JESTPE.2021.3069810.

[295] C. Zhu, "High-efficiency, mediumvoltage-input, solid-statetransformer-based 400-kw/1000-v/400-a extreme fast charger for electric vehicles," (accessed on 05/04/2022). eprint: Availableonline:www.energy.gov/sites/prod/files/2019/06/f64/elt241_zhu_2019_o_4.24_9.31pm_jl.pdf.

[296] V. Ramachandran, A. Kuvar, U. Singh, S. Bhattacharya, and M. Baran, "A system level study employing improved solid state transformer average models with renewable energy integration," in *2014 IEEE PES General Meeting | Conference Exposition*, 2014, pp. 1–5. DOI: 10.1109/PESGM.2014.6939922.

[297] T. Zhao, G. Wang, S. Bhattacharya, and A. Q. Huang, "Voltage and power balance control for a cascaded h-bridge converter-based solid-state transformer," *IEEE Transactions on Power Electronics*, vol. 28, no. 4, pp. 1523–1532, 2013. DOI: 10.1109/TPEL.2012.2216549.

[298] Z. Qu, Y. Yao, Y. Wang, C. Zhang, Z. Chong, and A. Abu-Siada, "A novel unbalance compensation method for distribution solid-state transformer based on reduced order generalized integrator," *IEEE Access*, vol. 7, pp. 108 593–108 603, 2019. DOI: 10.1109/ACCESS.2019.2933414.

[299] J. Shi, W. Gou, H. Yuan, T. Zhao, and A. Q. Huang, "Research on voltage and power balance control for cascaded modular solid-state transformer," *IEEE Transactions on Power Electronics*, vol. 26, no. 4, pp. 1154–1166, 2011. DOI: 10.1109/TPEL.2011.2106803.

[300] Y. Yu, G. Konstantinou, B. Hredzak, and V. G. Agelidis, "Power balance of cascaded h-bridge multilevel converters for large-scale photovoltaic integration," *IEEE Transactions on Power Electronics*, vol. 31, no. 1, pp. 292–303, 2016. DOI: 10.1109/TPEL.2015.2406315.

[301] L. Wang, D. Zhang, Y. Wang, B. Wu, and H. S. Athab, "Power and voltage balance control of a novel three-phase solid-state transformer using multilevel cascaded h-bridge inverters for microgrid applications," *IEEE Transactions on Power Electronics*, vol. 31, no. 4, pp. 3289–3301, 2016. DOI: 10.1109/TPEL.2015.2450756.

[302] J. E. Huber and J. W. Kolar, "Volume/weight/cost comparison of a 1mva 10 kv/400 v solid-state against a conventional low-frequency distribution transformer," in *2014 IEEE Energy Conversion Congress and Exposition (ECCE)*, 2014, pp. 4545–4552. DOI: 10.1109/ECCE.2014.6954023.

[303] Q. Chen, N. Liu, C. Hu, L. Wang, and J. Zhang, "Autonomous energy management strategy for solid-state transformer to integrate pv-assisted ev charging station participating in ancillary service," *IEEE Transactions on Industrial Informatics*, vol. 13, no. 1, pp. 258–269, 2017. DOI: 10.1109/TII.2016.2626302.

[304] A. Abu-Siada, J. Budiri, and A. F. Abdou, "Solid state transformers topologies, controllers, and applications: State-of-the-art literature review," *Electronics*, vol. 7, no. 11, 2018, ISSN: 2079-9292. DOI: 10.3390/electronics7110298. [Online]. Available: https://www.mdpi.com/2079-9292/7/11/298.

[305] Y. Tahir, I. Khan, S. Rahman, *et al.*, "A state-of-the-art review on topologies and control techniques of solid-state transformers for electric vehicle extreme fast charging," *IET Power Electronics*, vol. 14, no. 9, pp. 1560–1576, 2021. DOI: https://doi.org/10.1049/pel2.12141.

[306] D. Ronanki, A. Kelkar, and S. S. Williamson, "Extreme fast charging technology—prospects to enhance sustainable electric transportation," *Energies*, vol. 12, no. 19, 2019, ISSN: 1996-1073. DOI: 10.3390/en12193721. [Online]. Available: https://www.mdpi.com/1996-1073/12/19/3721.

[307] S. Debnath, J. Qin, B. Bahrani, M. Saeedifard, and P. Barbosa, "Operation, control, and applications of the modular multilevel converter: A review," *IEEE Transactions on Power Electronics*, vol. 30, no. 1, pp. 37–53, 2015. DOI: 10.1109/TPEL.2014.2309937.

[308] D. Rothmund, T. Guillod, D. Bortis, and J. W. Kolar, "99.1% efficient 10 kv sic-based medium-voltage zvs bidirectional single-phase pfc ac/dc stage," *IEEE Journal of Emerging and Selected Topics in Power Electronics*, vol. 7, no. 2, pp. 779–797, 2019. DOI: 10.1109/JESTPE.2018.2886140.

[309] T. Isobe, R. A. Barrera-Cardenas, Z. He, Y. Zou, K. Terazono, and H. Tadano, "Control of three-phase solid-state transformer with phase-separated configuration for minimized energy storage capacitors," *IEEE Journal of Emerging and Selected Topics in Power Electronics*, vol. 8, no. 3, pp. 3014–3028, 2020. DOI: 10.1109/JESTPE.2019.2923785.

[310] M. Vasiladiotis and A. Rufer, "A modular multiport power electronic transformer with integrated split battery energy storage for versatile ultrafast ev charging stations," *IEEE Transactions on Industrial Electronics*, vol. 62, no. 5, pp. 3213–3222, 2015. DOI: 10.1109/TIE.2014.2367237.

[311] Z. Liu, S. Li, F. Xiao, *et al.*, "Adaptive control strategy of solid state transformer with fast dynamic response and enhanced balance performance," *IET Power Electronics*, vol. 15, no. 4, pp. 306–316, 2022. DOI: https://doi.org/10.1049/pel2.12231. eprint: https://ietresearch.onlinelibrary.wiley.com/doi/pdf/10.1049/pel2.12231.

[312] I. S. Bayram, G. Michailidis, and M. Devetsikiotis, "Unsplittable load balancing in a network of charging stations under qos guarantees," *IEEE Transactions on Smart Grid*, vol. 6, no. 3, pp. 1292–1302, 2015. DOI: 10.1109/TSG.2014.2362994.

[313] G. R. C. Mouli, J. Kaptein, P. Bauer, and M. Zeman, "Implementation of dynamic charging and v2g using chademo and ccs/combo dc charging standard," in *2016*

IEEE Transportation Electrification Conference and Expo (ITEC), 2016, pp. 1–6. DOI: 10.1109/ITEC.2016.7520271.

[314] M. Campaña, E. Inga, and J. Cárdenas, "Optimal sizing of electric vehicle charging stations considering urban traffic flow for smart cities," *Energies*, vol. 14, no. 16, 2021, ISSN: 1996-1073. DOI: 10.3390/en14164933. [Online]. Available: https://www.mdpi.com/1996-1073/14/16/4933.

[315] R.-C. Leou, "Optimal charging/discharging control for electric vehicles considering power system constraints and operation costs," *IEEE Transactions on Power Systems*, vol. 31, no. 3, pp. 1854–1860, 2016. DOI: 10.1109/TPWRS.2015.2448722.

[316] M. Jha, F. Blaabjerg, M. A. Khan, V. S. Bharath Kurukuru, and A. Haque, "Intelligent control of converter for electric vehicles charging station," *Energies*, vol. 12, no. 12, 2019, ISSN: 1996-1073. DOI: 10.3390/en12122334. [Online]. Available: https://www.mdpi.com/1996-1073/12/12/2334.

[317] S. Bai, D. Yu, and S. Lukic, "Optimum design of an ev/phev charging station with dc bus and storage system," in *2010 IEEE Energy Conversion Congress and Exposition*, 2010, pp. 1178–1184. DOI: 10.1109/ECCE.2010.5617834.

[318] M. Gjelaj, C. Træholt, S. Hashemi, and P. B. Andersen, "Optimal design of dc fast-charging stations for evs in low voltage grids," in *2017 IEEE Transportation Electrification Conference and Expo (ITEC)*, 2017, pp. 684–689. DOI: 10.1109/ITEC.2017.7993352.

[319] A. Shukla, K. Verma, and R. Kumar, "Voltage-dependent modelling of fast charging electric vehicle load considering battery characteristics," *IET Electrical Systems in Transportation*, vol. 8, no. 4, pp. 221–230, 2018. DOI: https://doi.

org/10.1049/iet-est.2017.0096. eprint: https://ietresearch.onlinelibrary.wiley.com/doi/pdf/10.1049/iet-est.2017.0096. [Online]. Available: https://ietresearch.onlinelibrary.wiley.com/doi/abs/10.1049/iet-est.2017.0096.

[320] M. O. Badawy and Y. Sozer, "Power flow management of a grid tied pv-battery system for electric vehicles charging," *IEEE Transactions on Industry Applications*, vol. 53, no. 2, pp. 1347–1357, 2017. DOI: 10.1109/TIA.2016.2633526.

[321] M. Shibl, L. Ismail, and A. Massoud, "Machine learning-based management of electric vehicles charging: Towards highly-dispersed fast chargers," *Energies*, vol. 13, no. 20, 2020, ISSN: 1996-1073. DOI: 10.3390/en13205429. [Online]. Available: https://www.mdpi.com/1996-1073/13/20/5429.

[322] C. Leone, M. Longo, L. M. Fernández-Ramírez, and P. García-Triviño, "Multi-objective optimization of pv and energy storage systems for ultra-fast charging stations," *IEEE Access*, vol. 10, pp. 14 208–14 224, 2022. DOI: 10.1109/ACCESS.2022.3147672.

[323] N. B. Y. Gorla, S. Kolluri, M. Chai, and S. K. Panda, "A comprehensive harmonic analysis and control strategy for improved input power quality in a cascaded modular solid state transformer," *IEEE Transactions on Power Electronics*, vol. 34, no. 7, pp. 6219–6232, 2019. DOI: 10.1109/TPEL.2018.2873201.

[324] P. Sochor and H. Akagi, "Theoretical comparison in energy-balancing capability between star- and delta-configured modular multilevel cascade inverters for utility-scale photovoltaic systems," *IEEE Transactions on Power Electronics*, vol. 31, no. 3, pp. 1980–1992, 2016. DOI: 10.1109/TPEL.2015.2442261.

[325] Y. Yu, G. Konstantinou, C. D. Townsend, R. P. Aguilera, and V. G. Agelidis, "Delta-connected cascaded h-bridge multilevel converters for large-scale photovoltaic grid integration," *IEEE Transactions on Industrial Electronics*, vol. 64, no. 11, pp. 8877–8886, 2017. DOI: 10.1109/TIE.2016.2645885.

[326] IEEE, "IEEE recommended practice and requirements for harmonic control in electric power systems," *IEEE Std 519-2014 (Revision of IEEE Std 519-1992)*, pp. 1–29, 2014. DOI: 10.1109/IEEESTD.2014.6826459.

[327] N. Tashakor, B. Arabsalmanabadi, T. Ghanbari, E. Farjah, and S. Götz, "Start-up circuit for an electric vehicle fast charger using ssicl technique and a slow estimator," *IET Generation, Transmission & Distribution*, vol. 14, no. 12, pp. 2247–2255, 2020. DOI: https://doi.org/10.1049/iet-gtd.2019.1477.

[328] M. Safayatullah, M. T. Elrais, S. Ghosh, R. Rezaii, and I. Batarseh, "A comprehensive review of power converter topologies and control methods for electric vehicle fast charging applications," *IEEE Access*, vol. 10, pp. 40 753–40 793, 2022. DOI: 10.1109/ACCESS.2022.3166935.

[329] S. Ansari, A. Chandel, and M. Tariq, "A comprehensive review on power converters control and control strategies of ac/dc microgrid," *IEEE Access*, vol. 9, pp. 17 998–18 015, 2021. DOI: 10.1109/ACCESS.2020.3020035.

[330] P. Antoniewicz and M. P. Kazmierkowski, "Virtual-flux-based predictive direct power control of ac/dc converters with online inductance estimation," *IEEE Transactions on Industrial Electronics*, vol. 55, no. 12, pp. 4381–4390, 2008. DOI: 10.1109/TIE.2008.2007519.

[331] S. Shao, H. Chen, X. Wu, J. Zhang, and K. Sheng, "Circulating current and zvs-on of a dual active bridge dc-dc converter: A review," *IEEE Access*, vol. 7, pp. 50 561–50 572, 2019. DOI: 10.1109/ACCESS.2019.2911009.

[332] B. Zhao, Q. Yu, and W. Sun, "Extended-phase-shift control of isolated bidirectional dc–dc converter for power distribution in microgrid," *IEEE Transactions on Power Electronics*, vol. 27, no. 11, pp. 4667–4680, 2012. DOI: 10.1109/TPEL.2011.2180928.

[333] R. De Doncker, D. Divan, and M. Kheraluwala, "A three-phase soft-switched high power density dc/dc converter for high power applications," in *Conference Record of the 1988 IEEE Industry Applications Society Annual Meeting*, 1988, 796–805 vol.1. DOI: 10.1109/IAS.1988.25153.

[334] V. M. Iyer, S. Gulur, G. Gohil, and S. Bhattacharya, "An approach towards extreme fast charging station power delivery for electric vehicles with partial power processing," *IEEE Transactions on Industrial Electronics*, vol. 67, no. 10, pp. 8076–8087, 2020. DOI: 10.1109/TIE.2019.2945264.

[335] A. C. Nair and B. G. Fernandes, "A solid state transformer based fast charging station for all categories of electric vehicles," in *IECON 2018 - 44th Annual Conference of the IEEE Industrial Electronics Society*, 2018, pp. 1989–1994. DOI: 10.1109/IECON.2018.8592739.

[336] A. M. A and E. Cherian, "A power factor correcting electric vehicle fast charger with wide voltage range," in *2022 4th International Conference on Smart Systems and Inventive Technology (ICSSIT)*, 2022, pp. 569–576. DOI: 10.1109/ICSSIT53264.2022.9716504.

[337] X. Liang, S. Srdic, J. Won, E. Aponte, K. Booth, and S. Lukic, "A 12.47 kv medium voltage input 350 kw ev fast charger using 10 kv sic mosfet," in *2019 IEEE Applied Power Electronics Conference and Exposition (APEC)*, 2019, pp. 581–587. DOI: 10.1109/APEC.2019.8722239.

[338] D. Cittanti, M. Gregorio, E. Bossotto, F. Mandrile, and R. Bojoi, "Full digital control and multi-loop tuning of a three-level t-type rectifier for electric vehicle ultra-fast battery chargers," *Electronics*, vol. 10, no. 12, 2021, ISSN: 2079-9292. DOI: 10.3390/electronics10121453. [Online]. Available: https://www.mdpi.com/2079-9292/10/12/1453.

[339] A. Lahooti Eshkevari, A. Mosallanejad, and M. Sepasian, "In-depth study of the application of solid-state transformer in design of high-power electric vehicle charging stations," *IET Electrical Systems in Transportation*, vol. 10, no. 3, pp. 310–319, 2020. DOI: https://doi.org/10.1049/iet-est.2019.0106. [Online]. Available: https://ietresearch.onlinelibrary.wiley.com/doi/abs/10.1049/iet-est.2019.0106.

[340] S. Srdic, C. Zhang, X. Liang, W. Yu, and S. Lukic, "A sic-based power converter module for medium-voltage fast charger for plug-in electric vehicles," in *2016 IEEE Applied Power Electronics Conference and Exposition (APEC)*, 2016, pp. 2714–2719. DOI: 10.1109/APEC.2016.7468247.

[341] P. Chakraborty, R. Parker, T. Hoque, *et al.*, "Addressing the range anxiety of battery electric vehicles with charging en route," *Scientific Reports*, vol. 12, no. 1, p. 5588, Apr. 2022, ISSN: 2045-2322. DOI: 10.1038/s41598-022-08942-2. [Online]. Available: https://doi.org/10.1038/s41598-022-08942-2.

[342] M. Shafiei and A. Ghasemi-Marzbali, "Fast-charging station for electric vehicles, challenges and issues: A comprehensive review," *Journal of Energy Storage*, vol. 49, p. 104 136, 2022, ISSN: 2352-152X. DOI: https://doi.org/10.1016/j.est.2022.104136. [Online]. Available: https://www.sciencedirect.com/science/article/pii/S2352152X22001700.

[343] T. Guillod, F. Krismer, R. Färber, C. M. Franck, and J. W. Kolar, "Protection of mv/lv solid-state transformers in the distribution grid," in *IECON 2015 - 41st Annual Conference of the IEEE Industrial Electronics Society*, 2015, pp. 003 531–003 538. DOI: 10.1109/IECON.2015.7392648.